Winter 1-31-2023

Carbon Dioxide Capture Potential of Chitosan-Nanocrystalline Cellulose Aerogel Composite Materials: Synthesis, Functionalization, and Characterization

Victor Oghenekohwo
voghenekohwo@aucegypt.edu

The American University in Cairo
الجامعة الأمريكية بالقاهرة

Graduate Studies

Carbon Dioxide Capture Potential of Chitosan-Nanocrystalline Cellulose Aerogel Composite Materials: Synthesis, Functionalization, and Characterization

A Thesis Submitted by

Victor James Oghenekohwo

TO THE

Chemistry Program

06-07-2022

in partial fulfillment of the requirements for the degree of
Master of Science in Chemistry

DECLARATION OF AUTHORSHIP

I, Victor James Oghenekohwo, declare that this thesis titled, "*Carbon Dioxide Capture Potential of Chitosan-Nanocrystallline Cellulose Aerogel Composite Materials: Synthesis, Functionalization, and Characterization*" and the work presented in it are my own. I confirm that:

- This work was done wholly or mainly while in candidature for a research degree at thisUniversity.

- Where any part of this thesis has previously been submitted for a degree or any other qualification at this University or any other institution, this has been clearly stated.

- Where I have consulted the published work of others, this is always clearly attributed.

- Where I have quoted from the work of others, the source is always given. With theexception of such quotations, this thesis is entirely my own work.

- I have acknowledged all main sources of help.

- Where the thesis is based on work done by myself jointly with others, I have made clearexactly what was done by others and what I have contributed myself.

Signed:

Date: 06/07/2022

ABSTRACT

The carbon dioxide capture technology has been established as an invaluable player in the current global efforts to allay the warming of the planet and climate change. In this connection, the study centers on the valorization of waste organic materials for the application described herein. The sorbents, sourced from a combination of by-products of food processing and agricultural residue waste products, viz. seafood waste and sugarcane bagasse, showed prospects for selective carbon dioxide capture, adsorbing up to 5.78 mg/g of the gas at 273 K and 2.82 mg/g at 298 K, as observed on the Micromeritic ASAP 2020 surface area and porosity analyser. Further, thermogravimetric analysis (TGA) showed the materials to possess a decent level of thermal stability, making them fit for the purpose in an industrial setting. Scanning electron microscopy (SEM), transmission electron microscopy (TEM), fourier transform infrared spectroscopy (FT-IR), energy dispersive X-ray spectroscopy (EDS), X-ray diffraction (XRD), and viscometry were used to elucidate the microstructure and physicochemical properties of the materials. Drawing on the sorption performance of the aerogels, the low cost of raw materials, potential for scaling up, this work further validates the adsorbent-based carbon capture technology toward curbing the slowly revealing cataclysmic aftermaths of carbon dioxide emissions.

ACKNOWLEDGEMENTS

TABLE OF CONTENTS

LIST OF FIGURES

LIST OF TABLES

LIST OF ABBREVIATIONS

[BMIM][BF4]	1-Butyl-3-Methylimidazolium Tetrafluoroborate
BET	Brunauer-Emmett-Teller
CC	Carbon Dioxide Capture
CRCS	Crab Chitosan
CS	Chitosan
EDX/EDS	Energy Dispersive X-Ray Spectroscopy
FT-IR	Fourier Transform Infrared Spectroscopy
HEG/[BMIM][BF4]	Hydrogen Exfoliated Graphene/1-Butyl-3-Methylimidazolium Tetrafluoroborate
HNT	Halloysite Clay Nanotubes
MCS	Mantis Chitosan
MSP	Mantis Shrimp Powder
SABET	Brunauer-Emmett-Teller Surface Area
SBC	Sugarcane Bagasse Cellulose
SBCNC	Sugarcane Bagasse Cellulose Nanocrystals
SEM	Scanning Electron Microscopy
TEM	Transmission Electron Microscopy
TGA	Thermogravimetric Analysis
WSP	Whiteleg Shrimp Powder
SBC	Sugarcane Bagasse Cellulose
SBCNC	Sugarcan Bagasse Cellulose Nanocrystals
XRD	X-Ray Diffraction
BJH	Barette-Joyner-Halenda
MOF(s)	Metal-Organic Framework(S)
MCM	Mobil'S Composition Of Matter
GlcN	Glucosamine
GlcNAc	N-Acetyl Glucosamine
DD	Degree Of Deacetylation
CNF(s)	Cellulose Nanofibrils
CNC(s)	Cellulose Nanowhiskers

DRIFTS	Diffuse Reflectance Infrared Transform Spectroscopy
ONG	Oxygen-Functionalized Nanoporous Graphene
EMPPA	N-(2-Ethoxyethyl)-3-Morpholinopropan-1-Amine
MEA	Monoethanolamine
MMT	Montmorillonite
PDMS	Polydimethyl Siloxane
MDEA	Methyldiethanolamine
SLCM	Solid-Liquid Composite Micrometer-Sized Spheres
DAC	Direct Air Capture
TETA	Triethylenetetramine
GPS	3-Glycidoxypropyltrimethoxysilane
TPI	3-Triethoxysilylpropyl Isocyanate
PEI	Poly(Ethyleneimine)
PGA	Poly(Glycidyl Amine)
LPPI	Linear Poly(Propylenimine)
EAB	Electroactive Bacteria
MUF	Massey University Framework
PILs	Poly Ionic Liquids
rGO	Reduced Graphene Oxide
GNPs	Graphene Nanoplatelets
TEPA	Tetraethylene Pentaamine
CRP	Crab Shell Powder
CS1	Whiteleg Shrimp Chitosan
APTMS	(3-Aminopropyl) Trimethoxysilane

LIST OF SYMBOLS

η	Dynamic or Kinematic Viscosity
η_o	Pure Solvent Viscosity
η_{rel}	Viscosity
η_{sp}	Specific Viscosity
M_v	Viscosity Average Molecular Weight
λ	Wavelength

CHAPTER ONE

INTRODUCTION

The long-standing surge in energy demand since the industrial revolution has informed certain anthropogenic activities which significantly contribute to the emission of carbon dioxide into the earth's atmosphere. Following the Keeling curve (Figure 1), as maintained by Scripps Institution of Oceanography, the atmospheric carbon dioxide concentration continually accentuates when it needs to be falling, peaking at above 420 ppm very recently (SIO, 2022; WMO, 2022). In specific terms, from the year 1850 to 2018, about 645 gigatons of carbon dioxide has been emitted into the atmosphere (Friedlingstein *et al*., 2020). This trend has instigated an alarming rise of average global temperature relative to preindustrial levels. In addition, concerns regarding extreme weather patterns, sea level rise, ocean acidification, and so forth, have surfaced.
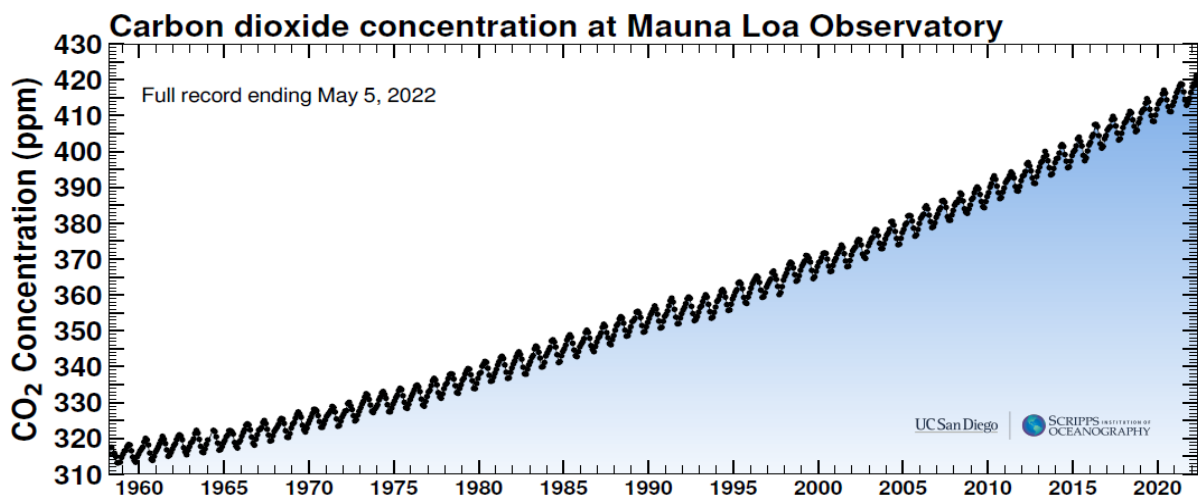
Figure 1: The Keeling Curve

Amongst all sources, fossil fuel combustion, especially for power generation, and other industrial activities account for over 70% of all CO_2 emissions (IPCC, 2013). One of the prominent strategies to mitigate emissions is post-combustion CC. The flue gas stream coming from the stacks of power plants is processed accordingly and the CO_2 fraction is selectively

isolated and either sequestered into underground geologic formations or transformed into value-added products (Pachauri *et al*., 2014).

Given its many decades of development, the amine scrubbing technology is the most mature strategy applicable for CC on a commercial scale. In a typical operation, the flue gas is bubbled through an amine solution and CO_2, being an acidic gas, reacts and dissolves in the capture solution (Rochelle, 2011). Despite this stance, the amine solutions used as absorbents are prone to technological barriers, including a high regeneration energy requirement, thermal degradation (Vega *et al*., 2014; Fredriksen *et al*., 2013), corrosion of equipment and the likelihood of secondary emissions (Wang *et al*., 2017).

As opposed to the amine technology which utilizes liquids, the adsorbent-based technologies are a product of solid materials. A typical adsorption process involves the adhesion of CO_2 to a sorbent's surface, usually a porous dry solid with high surface area. Some noble examples of materials used in adsorption are metal organic frameworks (MOFs) and porous carbon materials, which are deemed ideal candidates for adsorption owing to their outstanding physical and chemical properties (Guo *et al*., 2015).

Many scientists have been drawn to solid adsorption technology because of its ease of maintenance, simplicity of operation, and energy savings during adsorbent regeneration (Bai *et al*., 2015). While much attention with encouraging results (Choe *et al*., 2021; Sato & Hunger, 2020; Siegelman *et al*., 2019) Guo *et al*., 2020) have been devoted to advancing the adsorption technology in terms of sorption capacity, selectivity, and process efficiency, much work still needs to be undertaken to fabricate new adsorbent materials, validate the existing ones, and devise flexible routes that would make this technology less energy-intensive, efficient, eco-friendly, and cost competitive for commercial scale deployment.

Chitin and cellulose represent the most widely available biopolymers (El Knidr *et al*., 2018), and could be obtained in a facile manner. Chitin, a major component of the shells (exoskeleton) of sea animals, is usually processed into the more functional chitosan, while cellulose is chiefly obtained from plant matter.

Regarding the structure of chitosan, if the nitrogen atoms are evenly distributed throughout the material, their presence could improve CO_2 adsorption, as previous research has demonstrated that the presence of nitrogen atoms increases CO_2 capacity (Xia *et al*., 2011; Primo *et al*., 2012).

When used as adsorbent, a blend of chitosan and cellulose could offer a sustainable and economic path to carbon dioxide capture. Besides, introducing specific functionalities, mainly the CO_2-phillic ones, might make the process even more efficient. While chitosan (Kumar *et al*., 2020; Fujiki & Yogo, 2014; Qaroush *et al*., 2017; Hsan *et al*., 2019; Kumar *et al*., 2017; Wang *et al*., 2020) and cellulose (Miao *et al*., 2020; Hou *et al*., 2019; Sepahvand *et al*., 2020; Zhang *et al*., 2020) as well as their hybridized form with other materials have been reported in the literature for CC and other applications (Doustdar, *et al*., 2022a; Doustdar, *et al*., 2022b; Esmaeili *et al*., 2021), the carbon dioxide capture of a composite of both biopolymer was explored on a first-time basis herein.

In this study, chitosan was obtained by conventional chemical treatment of crustacean chitin, the major operations being deproteinization, demineralization, and deacetylation. In parallel, cellulose was isolated from different sources, including municipal waste and agricultural residues. Acid hydrolysis was further carried out on as-obtained cellulose from a chosen raw material to produce nanocrystalline cellulose. A sol-gel method was then employed to produce hydrogels comprising chitosan (matrix) and cellulose nanocrystals (reinforcement) and the neat aerogels were obtained following lyophilization.

In general, the goals of this study span the fabrication of an adsorbent for carbon dioxide coupled with its modification to improve adsorption capacity and selectivity. The composite, projected to be derived from waste materials of biological origin, will comprise chitosan as matrix and nanocrystalline cellulose filler.

1.0 Background Information on the Carbon Capture technology

Over time, the CC technology has proven its worth, and various routes have been explored to develop the process, some at laboratory scale and others at the industrial level. The industrially significant routes taken for CC include pre-combustion capture, oxy-combustion capture, post-combustion capture and direct air capture. Pre-combustion basically involves the reaction of fossil fuel with dilute air containing oxygen. The product of this reaction is a syngas, a mixture of carbon monoxide and hydrogen. Further reacting the carbon monoxide in a shift converter leads to the formation of CO_2, which could be processed for storage or recycling. The side-product, hydrogen, is mostly used as fuel.

Conversely, in oxy-combustion capture, the fuel is combusted in highly pure oxygen as opposed to air. Oxy-combustion produces a flue gas having a high concentration of CO_2. This process enables cost saving, since there is no need for a separate cryogenic separation or fractional distillation of air to obtain oxygen (Herzog, 2018).

In post-combustion, the CO_2 is removed only after the source material, mostly fossil fuel, has been burnt. The flue gas containing CO_2, N_2, water vapour, SO_2, and so forth, is sent to an absorber column where it contacts with the sorbent specially designed to capture the CO_2. This capture medium is further transferred to a stripper, where the CO_2 is desorbed and processed for use or storage.

Drawing inference from the Paris Agreement signed in 2016, CC is presumably not at the frontline of technologies needed to fulfil the pledges made for the first commitment period

leading up to 2030; renewable energies and related strategies are suited for this purpose. However, in subsequent commitment periods, CC has a significant role to play (Herzog, 2018). The Intergovernmental panel on Climate Change estimates that carbon capture would constitute between 15 and 55 % of the total efforts to combat climate change until 2100 (IPCC, 2006).

A question might be raised as to why CO_2 needs to be isolated from flue gas when really the whole flue gas could just be transported and stored away in geologic formations. A simple rationale for this is that extracting CO_2 from the flue gas is considerably less costly than transporting and storing the whole flue gas. Specifically, much capital goes into compressing CO_2 prior to transportation and storage. For example, the energy penalty for CO_2 compression in a supercritical pulverized coal power plant (SCPC) is around 8%, while that for compressing the whole flue gas will be over 70% (Herzog, 2018).

Another significance of CC lies in the fact that it is uniquely positioned to meet the mitigation goals of other industrial sectors. According to the Global Carbon Capture and Storage Institute, CC is particularly amenable to "difficult-to-abate" industries such as steel, cement, and fertilizer production. Both the IPCC and the International Energy agency (IEA) endorse this technology as one of the critical technologies for achieving net-neutral emissions by mid-century and meeting global climate change goals (Global CCS Institute, 2020).

This proceeding chapters in this discourse include a literature review, highlighting previous related studies and findings in the intended area of study, followed by a discussion of the approaches adopted while fabricating the adsorbent for the intended application. Next, the outcome of adsorbent fabrication, characterization, and adsorption studies was presented in the results and discussion section. In a final section, certain outlooks and concluding remarks regarding the study are presented.

CHAPTER TWO

LITERATURE REVIEW

This section is set off with a discussion of the chemistry and applications of chitosan and cellulose materials in relation to the literature. The latter part of the section gives reviews some of the literature on the utilization of solid adsorbents for carbon dioxide capture (CC). While emphasis is placed on the application of these kinds of materials for CC, their relevance for other major applications is also discussed.

2.0   Chitosan

Chitosan is a natural polycationic polymer and linear polysaccharide obtained as a functional product of chitin via deacetylation, i.e., the transformation of an acetamido into an amino group. Both molecules are characterized by N-acetyl-2-amino-2-deoxy-D-glucose (N-acetyl-glucosamine, GlcNAc) and 2-amino-2-deoxy-D-glucose (glucosamine, GlcN) residues linked to each other in (β1$\rightarrow$4) glycosidic bonds (Aranaz *et al*., 2021; Ababneh & Hameed, 2021). Figure 2 (a & b) illustrate a fragment each of the structure of chitin and chitosan, respectively. Since both these molecules have a similar structural backbone, their identities are contingent upon the predominance of the acetamido or amino groups, as shown in Figure 2c.

Although in the short term biopolymers cannot phase out their non-degradable counterparts, they can be utilized to abate the undesirable effects that accompany the extensive use of synthetic polymers (Riofrio *et al*., 2021). Given its ubiquity, chitin can be readily converted into chitosan, a nontoxic, biodegradable, and biocompatible polymer with numerous applications across several spheres (Al-Manhel, *et al*., 2018; Ahmed & Ikram, 2015).
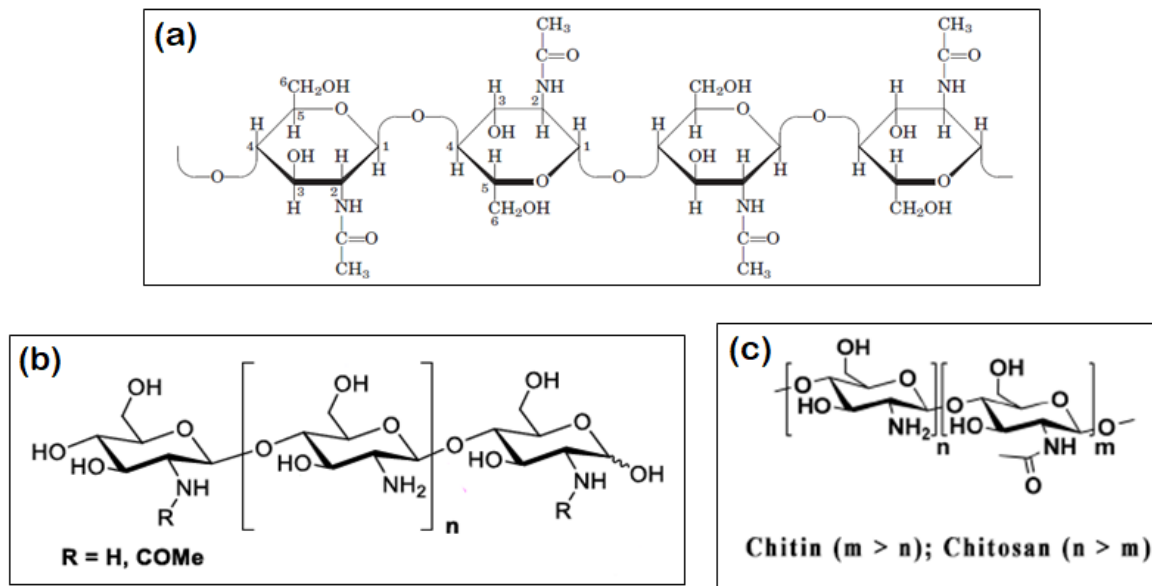
Figure 2: A Fragment of Chitin (a), a Fragment of Chitosan (b), and Backbone of Chitin or Chitosan (c)

Chitosan is biocompatible and nontoxic, with antibacterial (No *et al*., 2003), antifungal (Park *et al*., 2002), and anticancer properties (Qin *et al*., 2002). It also has good metal binding and wound healing properties (Ishihara *et al*., 2001), as well as the ability to decrease cholesterol (Ahn *et al*., 2021). Besides, the possibility to process chitosan into various forms, such as fibres, gels, sponges, makes it an ideal biopolymer (Jayakumar *et al*., 2010a; Jayakumar *et al*., 2010b).

2.1   Physicochemical Properties of Chitosan

An inexhaustive description of certain properties that significantly influence the application of chitosan follows. These include degree of deacetylation, molecular weight, and solubility.

2.1.1   Degree of Deacetylaion (DD)

The DD is expressed as percentage of N-amino-d-glucosamine (GlcN) units in the overall number of units. DD may be determined using the equation that follows:

$$DD\ (\%) = 100 * \frac{nGlcN}{nGlcN+nGlcNAc}$$

It is established that chitosan is derived from chitin by deacetylation (Figure 3). This degree of deacetylation marks the chitin from chitosan. When the DD exceeds 50%, the polymer is called

chitosan. During deacetylation, depolymerization reaction also occurs, altering the molecular weight of the polymer. Considering the susceptibility of the glycosidic bonds to acid (Hajji *et al*., 2014), alkali deacetylation is the most common route taken to achieve this end.
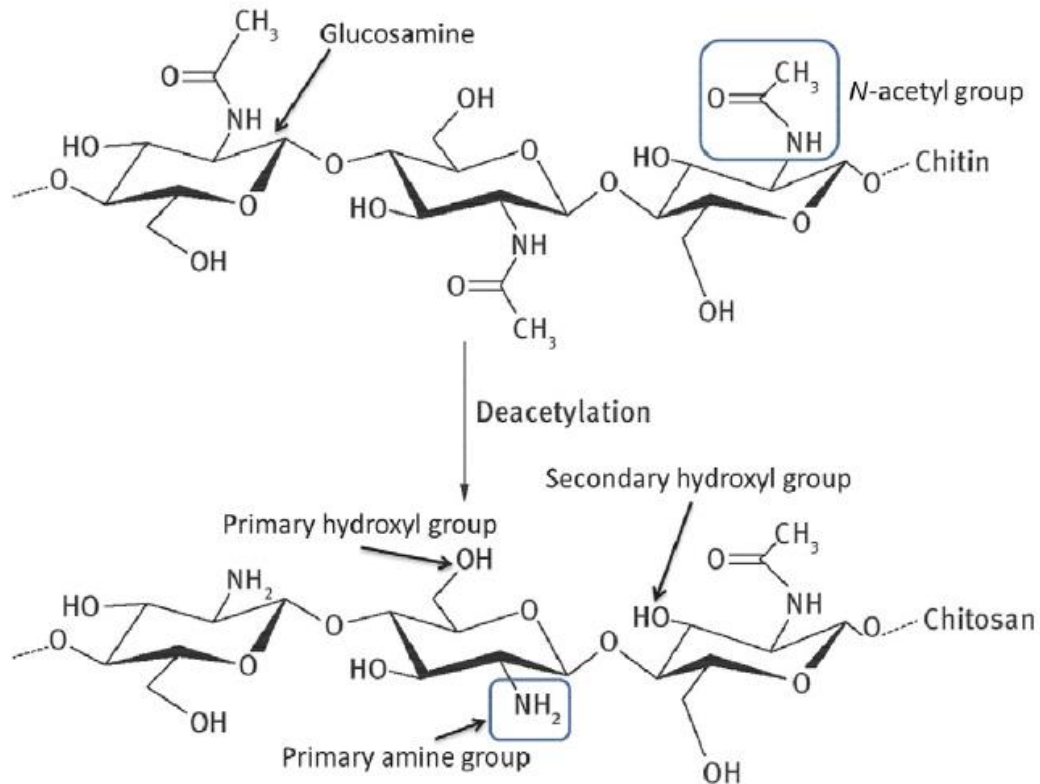
Figure 3: Deacetylation of Chitin to Chitosan (Adapted from Berezina, 2016)

Further, deacetylation is carried out either heterogeneously (Wardhono *et al*., 2021; Bradić *et al*., 2018) or homogeneously (Li *et al*., (2021). Homogeneous deacetylation proceeds with the treatment of chitin with concentrated NaOH and a subsequent dissolution in crushed ice at around 0 ºC (Kasaai, 2009). On the other hand, heterogeneous deacetylation involves the treatment of chitin with a hot concentrated solution of NaOH, producing chitosan as an insoluble residue (Wardhono *et al*., 2021; Bradić *et al*., 2018).

Typically, chitosan is never fully deacetylated and this phenomenon has yet to be reported. The DD, nonetheless, could be improved by repeating the deacetylation process. Different factors

influence the efficiency of deacetylation, including NaOH concentration, temperature and time of reaction (Tsaih & Chen, 2003).

2.1.2 Molecular Weight of Chitosan

Much of the same as with DD, the molecular weight of chitosan plays an integral role in the applicability of this material (Hwang *et al*., 2002) and is dependent on conditions like reaction temperature, alkali concentration, time, and atmospheric conditions of the deacetylation (Tolaimate *et al*., 2003).

Capillary viscometry represents one of the most widely used method for determining chitosan's molecular weight. An Ubbelohde-type capillary viscometer is usually employed to achieve this end. The viscometer is filled with solution of the sample and the time of flow of the solution and neat solvent through the capillary at 25 °C is used to estimate the relative viscosity from which the reduced viscosity is determined. From the plot of this reduced viscosity as a function of the polymer solution concentration, the intrinsic viscosity and, by extension, molecular weight can be estimated (Kasaai *et al*., 2000; Hwang, 2002).

Although different classifications exist in the literature, generally, chitosan is classified into three categories with respect to molecular weight, viz., low-molecular-weight chitosan (50 kDa), medium molecular weight (50-250 kDa), and high-molecular-weight chitosan (> 250 kDa) (Kumari and Rupak, 2020).

2.1.3 Solubility of Chitosan

Chitosan's solubility is subject to the influence of different factors, including molecular weight, degree of acetylation, pH, temperature, and polymer crystallinity (Aranaz *et al*., 2021). In the literature, the dissolution of chitosan nucleates around the use of acetic acid or an aqueous mixture of sodium hydroxide and urea. The preponderance of protonated primary amine (-NH_2) groups (pKa ~ 6.5) on chitosan's structure is largely responsible for its solubility in

aqueous acidic media (Mohammed *et al.*, 2017). Basically, low pH values enhance the ionization of amino groups (-NH2) to the quaternary ammonium ion (NH3$^+$) in the chitosan backbone, hence, facilitating solubility.

Rarely though, in a study by Zhang & Xi, (2014), the mechanism of dissolution of chitosan at high pH values was explicated. Solubility has been also found to vary with the DD. The rationale for this behavior lies with the fact that deacetylation leads to an increase in the number of glucosamine units and a modification in the crystalline structure of the polymer. According to Roy *et al.*, 2017, a DD $\geq$ 60% is deemed optimal for dissolution of chitosan.

The influence of crystallinity as well as intra- and intermolecular attractions on solubility was studied by Sogias *et al.* (2010). Here, solubility was found to decrease with polymer crystallinity following deacetylation. The increase in crystallinity was found to offset the effect of the increase in glucosamine moieties.

2.2   Cellulose

Given its abundance and facile isolation from virtually any plant matter, cellulose and its derivatives are versatile materials for many different applications. The global production of cellulosic materials reached a record 7.5×10^{10} tons per annum some years back (French, 2018; Habibi, 2014). Given the fact that cellulose is a renewable, environmentally friendly and cost-effective material (Bernard *et al.*, 2016), its production technology has continually been developed and cellulosic nanomaterials are being sought for high-value applications (Shak *et al.*, 2018; Khan *et al.*, 2014; Golmohammadi *et al.*, 2017; Abitbol *et al.*, 2016; George & Sabapathi, 2015; Habibi *et al.*, 2010).

Regarding its chemistry, the structure of cellulose ties in with that of chitin. Both polymers are composed of (β1$\rightarrow$4) glycosidic linkages. However, as opposed to chitin, where the C-2 atom

carries an acetamide group, in cellulose, a hydroxyl group is present at this position (Figure 4) (Ogawa & Okuyama, 2004).
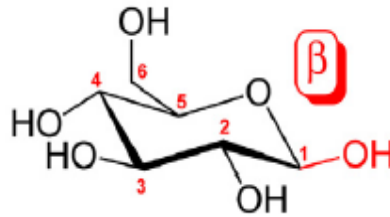
Figure 4: Basic Structure of Cellulose as a Fragment

2.2.1   Nanocellulose: Properties and Synthesis

The repeating units in natural cellulose tend to form linear chains of the polysaccharide (Klemm *et al*., 2005), which further aggregate into a hierarchical architecture of nanosized fibrils and rodlike crystals known as cellulose nanocrystals or nanowhiskers (CNCs) (Habibi *et al*., 2010). CNCs are crystalline, rod-shaped cellulosic molecules of diameter between 5 and 70 nanometers and lengths up to a few hundred nanometers (Klemm *et al*., 2011), whereas cellulose nanofibrils (CNFs) are a mixture of amorphous and crystalline cellulose chains with a relatively high aspect ratio. CNFs form long flexible fiber networks with a diameter similar to or larger than CNCs (Xu *et al*., 2013).

2.2.2   Mechanical Properties of Cellulosic Materials

In general, cellulose has a high tensile strength (Young's modulus of 20-50 GPa) (Usov *et al*., 2015; Wang *et al*., 2012) as a result of its hierarchical structure, which makes it ideal for use as a structural support in various applications.

Because of its huge aspect ratio (length of fibrils as a fraction of diameter *l/d*) and capacity to form linked network structures via hydrogen bonding, nanosized cellulose could impart reinforcing effects to composite matrices even at low concentrations. Specifically, with a modulus and bending strength of cellulose up to 150 GPa (Helbert *et al*., 1996; Sturcová,

Davies & Eichorn, 2005) and 10 GPa (Helbert *et al*., 1996), respectively, nanocellulose fibril's incorporation in chitosan matrix can bolster the mechanical properties of chitosan-based composite materials.

2.2.3   Aspect ratio of Nanocellulose Materials

Theoretically, in a composite, the efficiency with which mechanical stress is transferred to the filler through the matrix determines the performance of reinforcement. Generally, high aspect ratio fibres, such as CNFs, are better at sustaining mechanical load uniformly across the matrix (Klemm *et al*., 2011; Xu *et al*., 2013) but their predisposition to entangle makes their uniform distribution in composites a tall order, thereby limiting the improvement of mechanical profiles. Besides, Xu *et al*. (2013), in a study comparing the reinforcement effect of CNCs and CNFs in a polyethylene oxide matrix noted that, considering their entanglements and percolation, CNFs have a higher probability of fibre agglomeration than CNCs, resulting in lower strain-at-failure for such composites.

2.2.4   Synthesis of Nanocelluloses

Regarding the synthesis of CNCs, acid hydrolysis normally used to remove amorphous parts of a pure cellulose source, followed by ultrasonic treatment. Usually, there is a variation in structure from one source of cellulose to another and the crystallinity of these sources dictates what dimensions of nanocrystals are liberated (Klemm *et al*., 2011). For instance, cotton, wood, and Avicel (Dong *et al*., 1996) produce a narrow distribution of highly crystalline (90 percent crystallinity) nanorods (width: 5–10 nm, length: 100–300 nm) that are highly crystalline (90 percent crystallinity) nanorods (width: 5–10 nm, length: 100–300 nm).

The surface chemistry of CNCs is a function of the mineral acid used in hydrolysis: materials prepared with HCl are weakly negatively charged, whereas crystallites prepared with H_2SO_4 are more negatively charged, with one tenth of the glucopyranose residues functionalized with

sulphate ester (SO_3^-) groups via a substitution of the hydroxy groups (Xu *et al*., 2013; Araki *et al*., 1999; Edgar & Gray, 2003). Further, CNCs obtained via hydrolysis with H_2SO_4 have been shown to possess better colloidal stabilities, given their relatively extensive repulsive nature. The size of crystals was also shown to be dependent on the length of the hydrolysis, with an extended reaction time, resulting in smaller crystals (Beck-Candanedo *et al*., 2005; Elazzouzi-Hafraoui *et al*., 2008).

2.3   Aerogel Composites

Aerogels are solid materials characterized by their light weight, made up of up to 99.98 percent air by volume but also highly porous and stiff (Nguyen *et al*., 2013; Pierre and Pajonk, 2007). The structure of an aerogel is characterized by a high porosity, large specific surface area, and a decent surface chemical reactivity. Optoelectronics, adsorption catalysis, acoustic insulation, medical materials, aerospace materials, and a variety of other applications serve to benefit immensely from aerogel' chemistry (Maleki, 2016; Vareda *et al*., 2016; Stergar & Maver, 2016; Bheekun *et al*., 2013).

Typically, aerogels are brittle, and they fracture when under much pressure. Surmounting the problem surrounding aerogels' rigidity could open up a whole new spectrum of applications. Aerogel materials stand to benefit from cellulose and its derivatives in terms of mechanical characteristics and moisture affinity (Seantier *et al*., 2016). Because the cellulose chain contains several hydroxyl groups, intramolecular and intermolecular physical cross-linking of hydrogen bonds can be used to obtain a stable network structure, making the aerogel preparation process quite simple (Long *et al*., 2018).

Esmaeili *et al*. (2021) fabricated an aerogel composite of chitosan and CNFs with epichlorohydrin crosslinks, exploring its ability to adsorb an azo dye from water. The chitosan solution was made by dissolution in aqueous NaOH/urea and a CNF suspension was directly

added as well as the crosslinker. Finally, the aerogels were obtained by pre-freezing the mixture and subsequently freeze drying it. The resulting mesoporous aerogel, with a BET (Brunauer-Emmett-Teller) specific surface area of 315.10 $m^2 g^{-1}$, had a maximum spontaneous dye uptake of 1428.7 mg g^{-1}, following a chemisorption pathway. The authors suggest that the fabricated adsorbent could be a viable alternative to non-renewable synthetic aerogels.

In an attempt to study the hydrophobicity of an adsorbent for application in water remediation, for instance regarding oil spillage, (Meng *et al*., 2017) prepared a chitosan-cellulose aerogel. The material was prepared by dissolving each biopolymer in aqueous solutions of NaOH/urea at different proportions following the freeze-thaw method. The sol-gel technique was used to obtain hydrogels, and after coagulation, the gels were freeze-dried. Hydrophobicity was conferred on the gel when it was modified by sodium stearate through wet impregnation. According to the group, the aerogel shows potential to effectively adsorb oil from water separate water-in-oil emulsions stabilized by surfactants under gravity.

Alhwaige *et al*. (2013) fabricated aerogels based on a hybrid of chitosan matrix and graphene oxide nanofiller. Following a sol-gel procedure, as-prepared graphene oxide (modified Hummer's method) was dispersed in water by sonication. Acetic acid and chitosan were then added sequentially with mechanical stirring. The aerogel was produced after the pre-frozen hydrogel was lyophilized for 5 days. An apparent increase in BET surface area and CO_2 capacity was exhibited as the graphene oxide content increased up until 20% of the aerogel weight. The thermogravimetric analysis of the adsorbents demonstrates a thermally stable material while the cyclic adsorption-desorption profile shows an excellent regeneration of adsorbents.

2.4   Other Forms of Composite

Fujiki & Yogo, (2014) examined the CO_2 sorption mechanism of chitosan beads functionalized by polyethyleneimine with and without humidity using diffuse reflectance infrared transform spectroscopy (DRIFTS). The functionalized beads were placed in specialized cells and the DRIFTS spectra were collected while switching the gas flow between helium and CO_2 atmosphere at 313 K for 30 minutes. The material, which was prepared by dissolution and subsequent precipitation of chitosan in 5% lactic acid and 10M NaOH, displayed a CO_2 capacity of 2.3 mmol/g of adsorbent without water vapor with high selectivity. This capacity increased to 3.6 mmol/g in a humid atmosphere.

In another study, (Kumar *et al*., 2018) synthesized a composite of chitosan and zeolite via dissolution, solvent exchange, and finally calcination for CO_2 capture and conversion. The thermograph obtained for the composite demonstrates it to be thermally stable. Besides, given a BET surface area of 68.36 $m^2 \, g^{-1}$ and its mesoporous structure as deduced from the type IV isotherm (showing hysteresis loop), the composite exhibited an enhanced adsorption behavior, fixing 1.7 mmol/g of CO_2. The composite was further used as a heterogeneous catalytic substrate for the cycloaddition reaction of adsorbed CO_2 with various epoxides. This opens up possibilities for generating cyclic carbonates which are considered to be of industrial significance.

The work of (Primo *et al*., 2012) nucleated around producing activated carbons from chitosan and alginate by valorizing biomass wastes. First, biopolymer beads were prepared and subsequently made into aerogel beads via supercritical drying. The study indicated an increase in surface area of the materials with calcination temperature, probably because of the decomposition of oxygenated groups (H_2O, CO_2, CO) leaving behind pores. Besides, the surface areas of the aerogel beads were further increased by subjecting the carbonized material to KOH treatment under thermal condition, promoting the creation of pores.

2.5   Other Adsorption Materials and Techniques

The general consensus is that materials which meet the criteria for a full-scale deployment of the CC technology, such as a high sorption capacity and selectivity, often require energy-intensive unit operations or pose environmental concerns. In light of this, research effort is steered in the direction of developing materials whose utilization serve to ease these pressing issues.

In a bid to address the energy penalty shortcoming associated with absorbent-based CC processes, especially amine scrubbing, He *et al.* (2019) set out fabricating a high-performance CO_2-selective nanoporous graphene membranes. First, monolayer graphene was exposed to oxygen-based plasma and ozone to produce oxygen-functionalized nanoporous graphene (ONG). Further, polymeric chains with strong affinity for CO_2 were grafted on the porous graphene lattice to obtain polymer-functionalized ONG. Ultimately, the addition of an oligomer of poly-(ethylene glycol)-dimethyl-ether (PEGDE) resulted in swelling of the CO_2-philic polymer layer in the polymer-functionalized ONG, the film produced being 20 nm thick, as illustrated in Figure 5, hence, realizing a sorbent with six times higher CO_2 permeance.
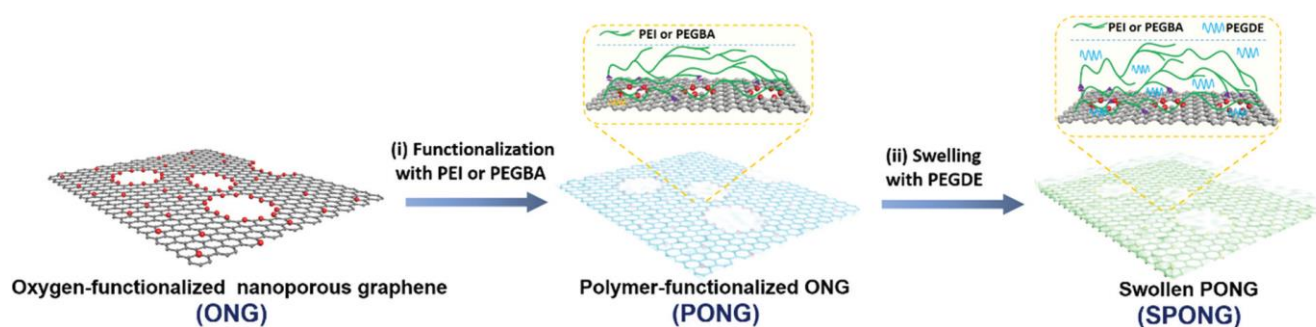
Figure 5: Schematic for Fabricating Polymer-Functionalized Nanoporous Graphene

More recently, Jiang *et al.* (2021) developed a one-component water lean solvent, N-(2-ethoxyethyl)-3-morpholinopropan-1-amine (EMPPA), for CC and compared the energy penalty with mono ethanolamine (MEA), a commonly used amine. In parallel, several studies have revealed, that by supplanting aqueous amine with water-free solvents, the energy penalties

associated with heat of vaporization, could be significantly abated (Mathias *et al*., 2013; Zheng *et al*., 2020). Consequently, the EEMPA produced has a 42 percent lower energy saving than the MEA, and given further solvent production and process optimization, cost savings could be achieved with the use of water-lean solvents could be reduced (Jiang *et al*., 2021).

Guo *et al*. (2020) sought to enhance the sorption capability of amines loaded into five commercial mesoporous frameworks, namely mesoporous alumina (MA), montmorillonite (MMT), silica gel, porous resin, and MCM-41 molecular sieve (MCM-41) (MCM = Mobil's Composition of Matter). According to this group, the adsorption of CO_2 on solid-supported amines is favored by components of flue gas, particularly H_2O. They backed up this view with the following equations of reaction (Dutcher *et al*., 2013):

$$2RNH_2 + CO_2 \leftrightarrow R\text{-}(NH_3+) (NHCOO^-)$$

$$(R^1)NH_2 + CO_2 + H_2O \leftrightarrow R^1\text{-}(NH_3^+) (HCO_3^-) \qquad (\text{R and } R^1 \text{ are alkyl groups})$$
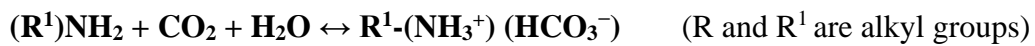
However, SO_2 hindered CO_2 adsorption, which was mostly due to SO_2's intense and irreversible binding to some amine sites. The adsorption of CO_2 was unaffected by NO (Guo *et al*., 2020).

In contrast to the abovementioned study by Guo *et al*. (2020), where the presence moisture contributed positively to adsorption, Park *et al*. (2020), synthesized a Mg_2(dobpdc) adsorbent (dobpdc = 4,4′-dihydroxy-(1,1′-biphenyl)-3,3′-dicarboxylic acid) functionalized with 1-ethylpropane-1,3-diamine, whose CO_2 sorption capacity decreased with moisture during humidity cycles. Following a careful diamine functionalization selection, the Mg_2(dobpdc) metal organic framework (MOF) displayed an appreciable adsorption potential (12.2 wt. percent) at 1000 ppm and desorption temperature of 70 °C. In addition, to increase water resistance, hydrophobic polymers, particularly polydimethyl siloxane (PDMS), were employed to coat the MOF surface.

Similarly, in another study, (Siegelman *et al*., 2019) showed that functionalizing the metal-organic framework $Mg_2(dobpdc)$ (dobpdc4 = 4,4′-dioxidobiphenyl-3,3′-dicarboxylate) with the cyclic diamine 2-(aminomethyl)piperidine (2-ampd) results in a 90% CO_2 capturing capacity from a moist natural gas flue emission source. According to this group, water enhances CO_2 capture in 2-ampd $Mg_2(dobpdc)$ through hydrogen-bonding with the carbamate groups of the ammonium carbamate chains formed upon CO_2 adsorption.

However, with respect to zeolites, experimentally, CO_2 sorption decreases significantly when moisture is present. This is due to H_2O's heavy dipole moment, which predominates over CO_2 in terms of occupying available coordination sites (Joos *et al*. 2013; Cmarik and Knox, 2018). As a result, removing the water component and realizing the maximum zeolite potential for adsorption of CO_2 in functional environments necessitates an activation stage. According to Mukherjee *et al*. (2019) and Masala *et al*. (2017), water vapor, being a constituent of crude natural gas streams, can interfere with physical gas adsorption

Kar *et al*. (2018) identified a CO_2 capture process using aqueous inorganic hydroxide solutions. After that, the CO_2-loaded solution (CO_2 + MOH + $MHCO_3$) was hydrogenated in situ with various catalysts to produce formate salts ((HCOO)n M). They claim that aqueous hydroxide solutions have many benefits over commonly used amines. These include widespread availability of hydroxides through electrolysis of aqueous salts, better carbon capture performance from surrounding air, insignificant vapor pressure, preventing atmospheric pollution, low toxicity, ease of regenerability. Noteworthy, NaOH/KOH are perfect for scrubbing CO_2 from very dilute sources like ambient air and further transforming it into value-added products.

Sen *et al*. (2020), following the carbon capture and utilization approach, converted alkali hydroxide-captured CO_2 into methanol on a first-time basis. Through a one-pot system, the

intermediate bicarbonate and formate salts were hydrogenated at 100-140 $^\circ$C and in the presence of Ru-PNP catalysts to methanol in ethylene glycol solution. This group posits that hydroxide bases are better suited for direct air capture and scalable conversion to methanol, as opposed to the amine counterparts, owing to their high capture efficiency and stability.

In a closely-related hydroxide-based route, although in solid state, Ruiz, *et al*. (2020) used NaOH for CO_2 capture and compared to their amine processing technique (based on methyldiethanolamine, MDEA) and indirect calcium looping with alkali (KOH/NaOH). Utilizings a small-scale model converter to quantify the CO_2 collected as well as gas sensors to assess the converter's capture capability, they concluded that in any event, significant savings on energy and carbon footprint were realized.

According to Kar *et al*. (2018), the regeneration of hydroxides is difficult and typically requires a series of high-temperature (~750 $^\circ$C) steps viz. causticization, calcination, and slaking. But compared to amines, Hydroxides are more effective than amines at trapping CO2 from dilute sources (Sanz-Pérez *et al*., 2016).

Wu *et al*. (2021) prepared an ultramicro-porous metal-organic framework (MOF-11) using the hydrothermal process. The product sorbent outperformed many other sorbents, based on published results, with a relatively high CO_2 capture capacity of 4.63 mmol per gram of sorbent at 25 $^\circ$C and 100 kPa, which then dropped to 2.92 mmol/g at a pressure of 15 kPa. However, subsequent CO_2 capture research centred on pore environment control to enhance adsorption under low pressure.

Further, given its porous structure, MOF-11 displays a strong structure affinity for CO_2, simultaneously weakening interactions with N_2, resulting in such high selectivity. This CO_2/N_2 separation efficiency was investigated using computational modelling and the binding energy

between the adsorbate and adsorbent was measured using the Density Functional Theory (Wu *et al*., 2021)

Zhang *et al*. (2018) devised an approach leading to the production of self-supported and flexible HKUST-1 (a metal organic framework otherwise known as MOF-199) nanofibrous membranes. Thermogravimetric analysis approach was then used to evaluate the sorbent's CO_2 capture characteristics. The promising CO_2 potential of the sorbent produced is due primarily to their extensive porous structure, large surface area, and abundance of open metal sites. Compared to N_2 molecules, CO_2 has a smaller molecular size, higher polarizability, and greater quadrupole moment, resulting in more stringent interactions between the open metal sites of the metal organic framework and CO_2, which makes for better CO_2/N_2 selectivity.

The use of MOF for CC opens up more possibilities for engineering solid sorbents. However, in spite of the recent advances in MOF chemistry, generating such system adsorbents with strong separation capabilities and more extensive performance characteristics including scalability, recyclability, and fast, low-energy regeneration remains a challenge (Qazvini *et al*., 2021).The large-scale implementation of this technology, which requires much less energy, has yet to be perfected, and questions about its long-term stability for long-term CO_2 capture projects suggest that its high cost is not yet justified (Ding *et al*., 2019).

Li *et al*. (2021) synthesized hierarchically structured porous carbon-based material double-doped with Boron/Nitrogen, using boric acid as precursor for boron and ethylenediamine for nitrogen, in order to design a high-performance sorbent for CO_2 capture. They showed how to make B, N-codoped carbon materials with hierarchical porous structures using a green, cost-effective, and powerful template-free process. Hydrothermal carbonization was used to create the material.

Wei *et al*. (2021) developed a new method for creating effective solid-liquid composite materials. Through a novel Pickering emulsion templating technique, they injected liquid amine into porous silica nanospheres that are encased in a micrometer-sized sphere's hydrophobic shell. The result of this are solid-liquid composite micrometer-sized spheres (SLCM). Such materials show exceptional capacity for CC in industrially preferred fixed-bed reactors, having rapid adsorption kinetics, long-term recyclability, and alleviated loss of amine. Overall, methods based on templating, for example, the works of (Wei *et al*., 2021) and (Qian *et al*., 2019) could be prone to difficulty in eliminating the template material, consequently expanding time and cost of operation.

Park *et al*. (2020) undertook a formulation and analysis of sorbents made from hyperbranched polyglycerol with trimethylammonium hydroxide groups, assessing the effect of humidity and temperature on the sorbents' adsorption/desorption features. The sorbent synthesized in this study behaved differently than a lot of materials described in the literature, given the considerably large number of hydrophilic hydroxyl groups in its structure. The sorption was carried out by humidity swing which is an especially appealing CO_2 capture technique because it captures and releases CO_2 by adjusting the moisture content, preventing costly heating/cooling cycles or major pressure variations over the sorbent.

Moreover, it was possible to desorb all the collected CO_2 in one hour just by applying a very short temperature impulse. From the application standpoint, this idea is significant and can be attributed to the polarity of polyglycerol, which facilitates the movement of released carbon dioxide from the polymer matrix. Besides, the desorption occurred even without the presence of moisture, indicating that CO_2 release is not exclusively contingent upon the formation of hydrated ammonium hydroxide moieties. According to this research group, the essence of this

process is extremely complex, and further research is needed to develop materials which possess swift adsorption/desorption kinetics. (Park *et al*. 2020).

From the perspective of DAC, Barzagli *et al*. (2020) sought to develop more effective and sustainable sorbents by screening a number of alkanolamines, especially those already used in CCS. Their findings showed the differences between DAC and traditional CCS processes, suggesting that the optimal CCS absorbents may not be ideal for the DAC process. In all, the researchers implied that non-aqueous sorbents are deemed unfit for DAC processes, particularly given that their use will necessitate significant reforms in traditional DAC equipment to mitigate loss of solvent and the resulting effects on the environment.

Li *et al*. (2020) investigated the microwave regeneration characteristics of various triethylenetetramine (TETA) solutions. According to the group, microwave regeneration could offer a path to alleviating energy consumption. Their findings showed viscosity, dielectric constant, and heat capacity of a solution to be the most important factors in its microwave heating rate.

Adopting on a different approach, Shu *et al*. (2020) spelled out an application of electrochemistry in CO_2 desorption from sorbents. Including such electrochemical systems in the desorption stage potentially leads to more energy savings, because the sorbent regeneration requires no heat, rather it the required energy comes from electricity. This makes the system amenable to renewable energy sources. Besides, as opposed to energy-intensive processes like causticization and calcination, the desorption of CO_2 desorption and sorbent regeneration occurring in one phase represents a strong advantage for lowering overall operating costs, as it simplifies the process activity (Mahmoudkhani and Keith, 2009).

Exploring a different class of materials, Cai *et al*. (2020) presented a facile direct CO_2 capture method using a new trichelating iminoguanidine ligand and reactive crystallization. According

to this group, (BTIG) might bind CO_2 strongly and reversibly, creating insoluble carbonate crystals which could be isolated without effort. Analyses of thermodynamics show that 81 kilojoules of energy is required to isolate the CO_2 molecule, a figure which is significantly less than the energy required for $CaCO_3$ decomposition (177.8 kJ/mol) which basically results from using sorbents based on hydroxides (Rodriguez-Navarro *et al*., 2009). However, a considerable amount of energy is still dedicated to water evaporation, and this raises the cost of ligand regeneration. To play down this limitation, the heat energy contained in the hot vapor could be recovered using a heat exchanger, a well-established technology in the industry. (Cai *et al*., 2020)

In a different study, Anyanwu *et al*. (2020) grafted N-(3-trimethoxysilylpropyl)-diethylenetriamine onto a series of silica gels. It was revealed that the silica gel with the largest pores (150 Angstrom) was optimal for subsequent enhancement of the capture efficiency, pore properties, and amine loading.

Kolle and Sayari, (2020) utilized 3-glycidoxypropyltrimethoxysilane (GPS) or 3-triethoxysilylpropyl isocyanate (TPI) as a grafting agent with triethylamine or sodium hydroxide base catalyst, for the covalent immobilisation of poly(ethyleneimine) (PEI) on PE-AlSiO$_2$. Consequent upon oxidative degradation at 100 °C for about 40 hours and leaching in thanol for 2 hours, covalently immobilised PEI using TPI and NaOH retained the most CO_2 as compared to conventional PEI impregnation. PEI was further modified with 1,2- epoxybutane, which improved oxidation stability even more.

Under the auspices of Global Thermostat, a large-scale facility for CC which operates in the United States, Sujan *et al*. (2019) synthesized a well-defined poly(glycidyl amine) (PGA) (Figure 6) and showed how it can be used to make PGA-loaded mesoporous silica for CO_2 capture both from flue gas and ultra-dilute air. The improved CO_2 mass transfer kinetics of

these amines on high surface area supports represents one of the main reasons for which absorption by liquid amine solutions was not employed. Moreover, the overall amine efficiencies of the PGA sorbents were similar to those of PEI, albeit at lower pore filling levels than PEI-based sorbents. As expected with PEI, in terms of amine quality, the PGA sorbents began to show a downshift trend at pore filling levels less than 100%. However, the materials had lower CO_2 capacities than PEI-based sorbents due to a declining trend in amine efficiency coupled with low net amine density as pore filling exceeded 100%.
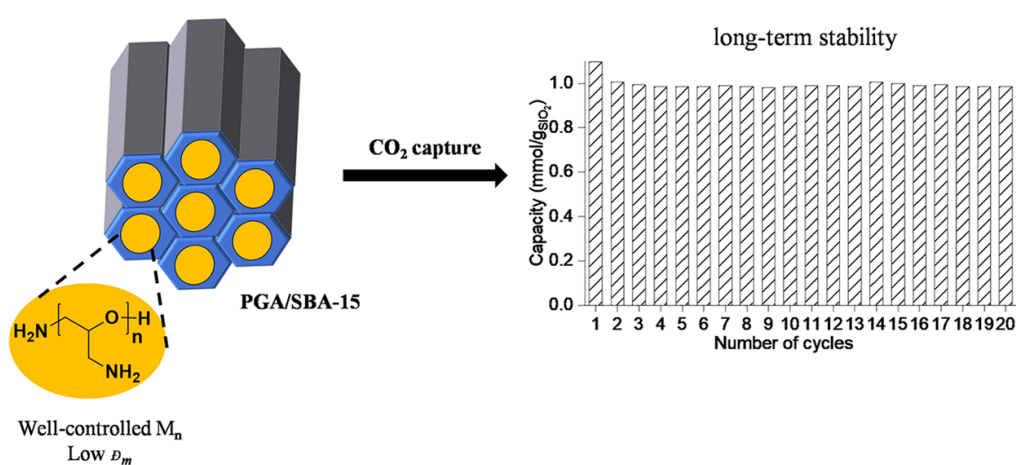
Figure 6: Poly(Glycidyl Amine) Loaded Onto Mesoporous Silica for CC (Sujan et al. 2019)

Wotzka *et al*. (2020) looked at the potential of powdered $Ce_{0.8}Zr_{0.2}O_2$, a multifunctional inorganic species. They employed mass spectroscopy to monitor the continuous adsorption of 400 ppm CO_2 from air on $Ce0.8Zr0.2O_2$ and subsequent release of dimethyl carbonate over time, when methanol is added. While the emphasis of this study was placed on the increasing the concentration of the released dimethyl carbonate, the group demonstrated that an upscaled sorbent material (550 cm^3 of $Ce_{0.8}Zr_{0.2}O_2$) shows prospects for CC comparable to values observed for the net carbon fixed by plants.

Guo *et al*. (2020) presented a novel technique for substantially extending the stability of CO_2 adsorbents. First, the group produced porous beads with a hydrophobic and extensive structure for long-term thermal and hydrothermal stability, by copolymerizing a water-in-oil emulsion

comprising several acrylates with epoxide groups. Through a ring-opening reaction, they then grafted tetraethylenepentamine between the epoxide and amine groups, on an acrylate copolymer framework with a subsequent functionalization step. In a simulated flue gas constituting O_2, SO_2, and steam, its sorption potential decreases by 9.8% after 1000 adsorption/desorption cycles, indicating its durability in a complex environment.

Sujan *et al*. (2019) described the use of polymer/silica fibre adsorbents functionalized with poly(ethylenimine) for DAC, essentially employing the dry-jet, wet quench spinning technique. By employing a vacuum- and temperature-assisted desorption step to extract CO_2 from ambient air, they recovered highly pure CO_2 with or without the effect of moisture.

Hou *et al*. (2019) reported using quaternized bamboo cellulose for DAC. In this work, they produced a sorbent with an ideal microstructure for gas diffusion, by imobilizing quaternary ammonium groups onto a natural lignocellulose support in a heterogeneous synthesis. Observation from quantifying the H_2O adsorption behavior revealed that the quaternized cellulose has a hydrophobic property. For 400 ppm CO_2, the adsorption is consistent with the Langmuir isotherm model, and the sorbent saturation is over 90%. Further, a low relative humidity ($< 20\%$) or a high relative humidity ($> 90\%$) was not favorable for CO_2 capture. The impact of water differences on the thermodynamics and kinetics of sorption, is thought to be linked to interfacial hydrophilicity.

For comparison, Qian *et al*. 2019) modified two Mobil's Composition of Matter (MCM) samples with poly(ethyleneimine). The templates of the traditional MCM-48-C sample are eliminated by the process of calcination, while the other sample, MCM-48-W, without calcination. Further, X-ray Diffraction and N_2 adsorption/desorption isotherms were employed to confirm the identity of the mesophases of MCM-48-C and MCM-48-W. Ultimately, the PEI impregnated samples of the MCM-48-W having pores saturated with cetyltrimethylammonium

bromide (CTAB with long alkyl chains) were observed as better CO_2 adsorbents than PEI-impregnated traditional MCM-48-C samples.

Rosu *et al*., (2020), in an effort to evaluate the integrity of linear poly(propylenimine) (LPPI) in mesoporous silica composites. According to them, physical ageing or degradation polymers which contain of amines as well as amine-grafted adsorbents is a crucial problem that poses limitations to their use in CO_2 capture applications. The results show that ageing and storage conditions had only slightly impacted the output of the LPPI-based adsorbent could, thereby demonstrating its potential in carbon capture applications over an extended period of time.

Generally, two major hurdles have to be surmounted for the appropriate use of these amine-supported adsorbents, in terms of their application. First, the material's adsorption efficiency and recyclability need to be optimized. Second, such adsorbents have to be worked into large structures to fulfil the criteria of continuous operation in fixed or fluidized beds (Wei *et al*., 2021). While PEI covalently linked on large surface area supports, such as MOFs, has been shown to display excellent CO_2 capture profiles, PEI grafted on other supports, such as mesoporous silicas, needs to be improved. Furthermore, the thermal stability of PEI-containing adsorbents in an inert or oxidising atmosphere is a significant limiting factor to their use. (Kolle & Sayari, 2020).

Earthen matter is another class of material that has been explored for its CC potential. Sato and Hunger, (2020). Solid-state nuclear magnetic resonance combined with open space analysis using positronium was used to investigate the CO_2 capture in cavities within saponite clay nanosheets. Under atmospheric conditions, CO_2 physiscal adsorption takes place on the surface of the nanosheet within the cavities. CO_2 molecules are enabled by removing weakly bound oxygen from octahedral sites at edges of the nanosheet, while carbonate species are stabilized

on the surfaces. In this study, the physical adsorption of CO_2 proceeded without an energy-consumption mechanism or chemical solution enhancement.

Lu *et al*. (2018) looked at how wastewater treatment can be used for carbon capture and utilization. A very common practice herein is Microbial Electrolytic Carbon Capture. In a typical set-up, wastewater is used as the electrolyte; microorganisms in the anode chamber, especially electroactive bacteria (EAB), oxidize biodegradable substances in wastewater, generating CO_2, electrons, and protons. The anode accepts electrons, which are then moved to the cathode through an external circuit, where water becomes reduced to generate H_2 and OH^- (Wang and Ren, 2013). Metal ions (Ca^{2+}, Mg^{2+}, and so on) can be liberated from abundant silicate minerals (such as wollastonite $CaSiO_3$) or waste materials (for example, coal fly ash) by the H^+-rich anolyte). Upon migrating to the catholyte, these metal ions form metal hydroxide, which reacts with CO_2, spontaneously absorbing it and eventually converting it into stable carbonate or bicarbonate (Lu *et al*, 2015).

With the aim of achieving selectivity, very recently Qazvini *et al*. (2021) synthesized MUF-16 (MUF = Massey University Framework), a MOF that displays inverse selectivity, which means it prefentially adsorbs carbon dioxide over hydrocarbon guests. Having exposed the MUF-16 to air and immersing in water, they tested the MOF's adsorption characteristics to elucidate its moisture resistance. Following these mistreatments, the framework retains its CO_2 adsorption ability.

The pores in MUF-16 bear comparable sizes and electrostatic potential to CO_2, causing the guest CO_2 to be trapped by H-bonding and other noncovalent interactions. Other gases, especially methane and C2 hydrocarbons, do not bind well. Resultantly, the group observed a clear preference for CO_2 over methane and inverted selectivity for CO_2 over C2 and C3

hydrocarbon. The rationale for this observation was attributed to the reversed polarity of these hydrocarbons relative to CO_2.

Different factors have been observed to affect the CO_2 sorption performance of PILs. Some of these were extensively reviewed by Zulfiqar *et al*. (2015). Such factors include but not limited to the nature of cation or anion, effect of alkyl chain substituents and backbone, effect of cross linking. The availability, cost, purity, and compatibility of PILs as a green option for CO_2 capture are the most significant obstacles.

Very recently, Wang *et al*. (2021) undertook the fabrication of graphene-IL composites for CC. With an interlayer spacing of only 3.4 Å in multilayer graphene, such as graphite, the accessible pore size is zero and it lacks the area to incorporate gas molecules This interlayer space could be made accessible by intercalating an ionic liquid with the graphene layers.

In a bid to achieve enhanced CO_2 absorption, Li *et al*. (2018) grafted an IL ([P66614][Triz]) on nanoplatelets of graphene (GNP) and reduced graphene oxide (rGO) following the dipping method as reported by Cheng *et al*. (2018). As obtained using the BET method, specific areas of GNP and rGO were 15.77 and 393.98 m^2/g for, respectively. The surface areas of GNP and rGO, on the other hand, were reduced to 1.06 and 5.45 m^2/g, respectively, after both being loaded with 20% IL loading. The rate of CO_2 sorption by the rGO/IL hybrid IL (20 % IL) was lower than that of neat IL. An explanation for this might be that rGO has a higher proportion of oxygen functional groups. Hydrogen bonds were thought to exist between the active site

(nitrogen) of the IL anions and the -OH functionalities of rGO, as illustrated schematically in Figure 7.
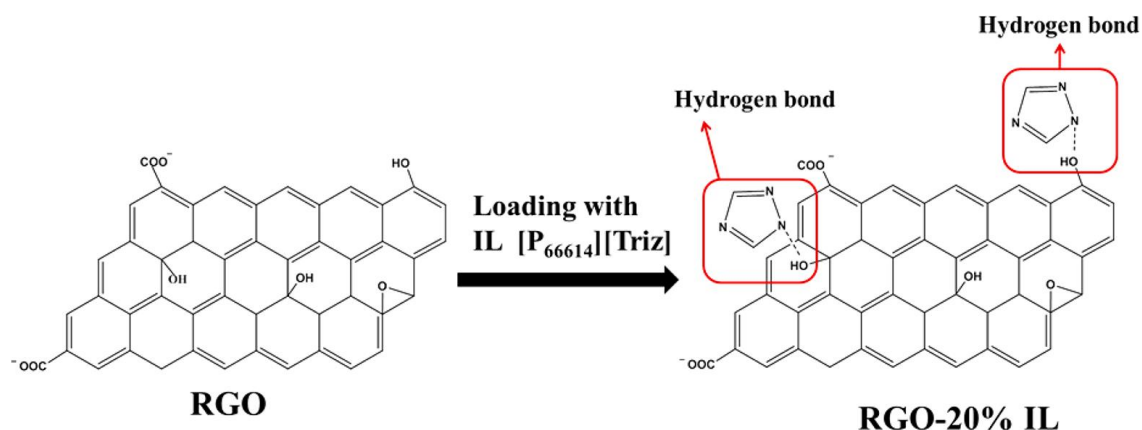
Figure 7: Illustration of Hydrogen Bonds Between Active Nitrogen in Anions and Hydroxyl Groups on Reduced Graphene Oxide (Source: Li et al. (2018)

To assess the ability of the hybrid (GNP-20 % IL) to regenerate, a total of ten absorption-regeneration cycles were performed (Figure 8). Given the decent stability of the ionic liquid, the sorption capacity of this sorbent remained consistent (92 % CO_2 absorption capacity), showing that the CO_2 capture process by this hybrid material is reversible.
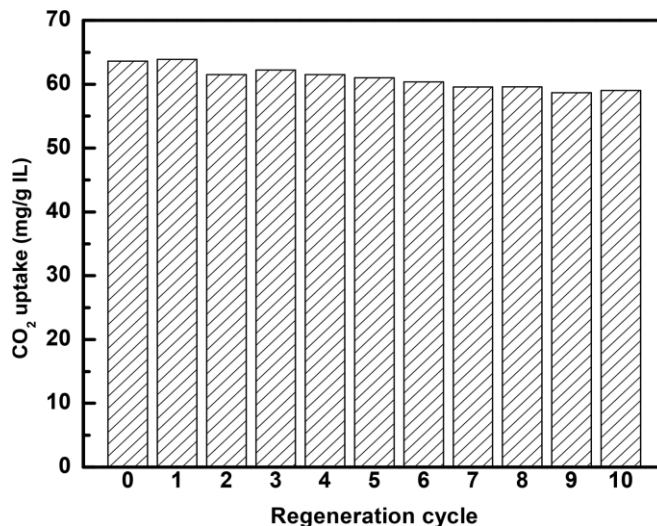
Figure 8: The Regeneration Characteristics of IL Loaded on Nanoplatelets of Graphene. Source: Li Et Al. (2018)

In a different work, (Tamilarasan *et al.*, 2013) revealed that the functionalization of hydrogen exfoliated graphene with 1-Butyl-3-methylimidazolium tetrafluoroborate ([BMIM][BF4]) improved the carbon dioxide capacity. A Sieverts apparatus was used to conduct the sorption

analysis. At 27 °C and 11.78 bar, the hybrid sorbent shows a CO_2 capacity of 42.32 mmol/g, which is higher than graphene (21.6 mmol/g at almost the same conditions).

To evaluate the thermal stability of the HEG/[BMIM][BF_4] nanocomposite sorbent, thermogravimetric (TG) analysis in an inert (nitrogen) atmosphere at a temperature range of 40–900 °C at a scan rate of 10 °C/min (Figure 9), was undertaken. Observation from the TG analysis were corroborated when the group studied the sorption capacity with the same material in 16 cycles at various pressures and temperatures and found no significant differences in adsorption kinetics or capacity. The thermal stability of the HEG/[BMIM][BF_4] nanocomposite, and the reversible dissolution of CO_2 in ionic liquid could explain this (Tamilarasan *et al*., 2013).
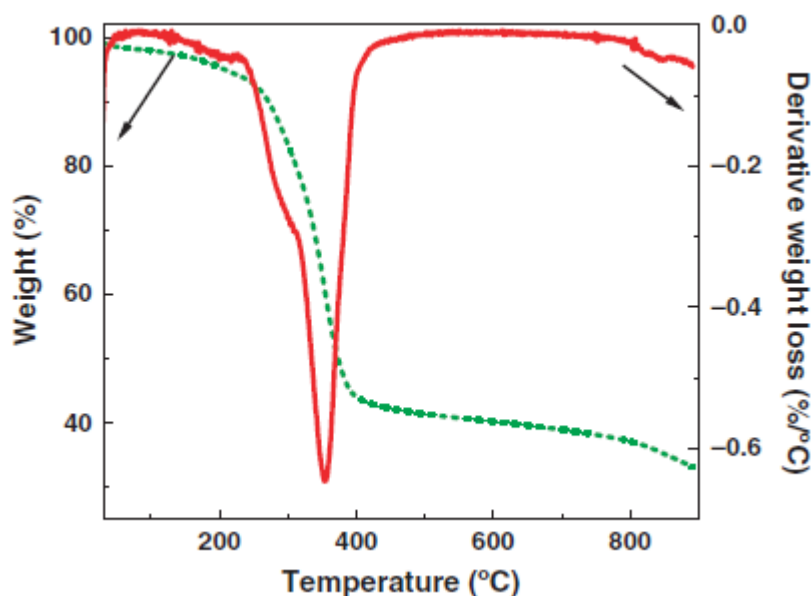
Figure 9: TGA profile of HEG/[BMIM][BF_4] (Source: Tamilarasan et al., 2013)

It could be deduced from the preceding explanation that HEG/[BMIM][BF$_4$] interacts with CO_2 in two ways, as indicated in Figure 10. Chemical interaction and multilayer adsorption may explain the improved adsorption capacity of HEG/[BMIM] [BF$_4$] nanocomposite over conventional solid adsorbents. It was also discovered that at high pressures, the change in sorption capacity increases with temperature, however at low temperatures, there is no sorption capacity. Physisorption plays a key role at high pressures, where an increase in temperature prevents porous condensation. However, at low pressures, physisorption contributes less than chemisorption, thus a temperature increase may not have a significant impact (Tamilarasan *et al.*, 2013).
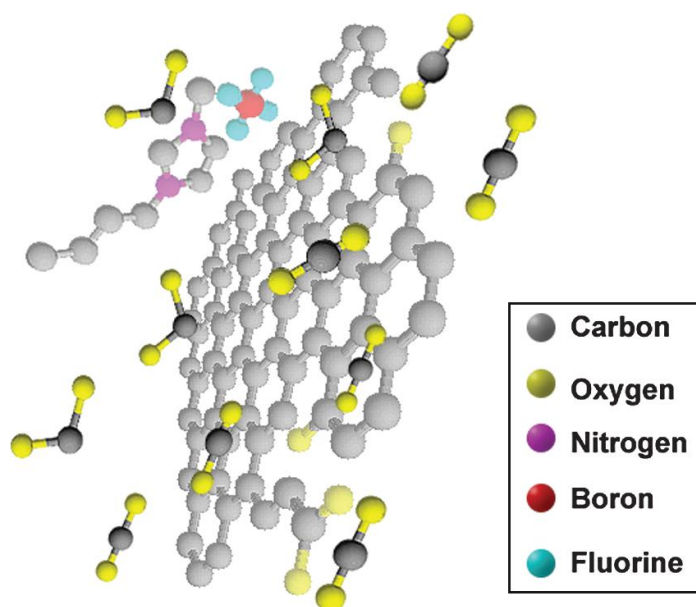
Figure 10: CO$_2$ Interaction with the Hybrid Material (Source: Tamilarasan et al., 2013)

Employing the Pickering emulsion technique, (Lee *et al.*, 2020) synthesized a task-specific ionic liquid (IL), 1-ethyl-3-methylimidazolium 2-cyanopyrolide ([EMIM] [2-CNpyr]), encapsulated with graphene oxide sheets and polyurea. This IL was used to capture CO_2 from moist air (CO_2 concentration from $0 - 5000$ppm).

Primarily, the goal was to reduce CO_2 mass transfer barriers in ionic liquids and develop enhanced solid sorbents tailored for fixed-bed reactors. The "one-pot" Pickering emulsion route offers scalability, and the resultant ionic liquid capsules possess a gas-permeable shell

that tremendously facilitates the rate at which CO_2 is absorbed (Huang *et al*., 2019). In a scenario where separation of CO_2 exists in a gas mixture with low partial pressures, this study presents a facile and alternative scheme for CO_2 scrubbing. Besides, it is demonstrated that a mixture of ionic liquids could also serve to reduce the effect of viscosity, essentially increasing CO_2 diffusivity and thus absorption rate.

2.6   Comparison of Technologies and Materials for CC

Given the plethora of parameters which are considered while designing materials and experiments for CC, it will be difficult to make a direct comparison of the techniques employed for this purpose. Thus, the discussion that follows is therefore with a superficial rather than an in-depth scope.

At present, the methods employed for CC mostly fall under two broad categories, that is post-combustion capture (from flue gas) and direct capture (from ambient air). These methods include absorption, adsorption, membrane separation, and oxy-combustion (Herzog, 2018). Noteworhty, some of these technologies could be theoretically applied for both aforementioned categories but are mostly applied for post-combustion capture.

In post-combustion, the CO_2 is removed only after the source material, mostly fossil fuel, has been burnt. The flue gas containing CO_2, N_2, water vapour and SO_2 is sent to an absorber column, where it contacts the sorbent specially designed to capture the CO_2. This capture medium is further transferred to a stripping column where the CO_2 is desorbed and processed for use or storage.

The absorption process proceeds either by physical or chemical means; for example, the amine scrubbing falls under chemical absorption because CO_2 reacts chemically with the amine. Chemical absorption is widely employed for post-combustion capture under a wide array of conditions (Herzog, 2018). As a relatively advanced form of CO_2 capture, the amine scrubbing

method still comes with some drawbacks, including the corrosion of equipment and the use of very volatile solvents that give rise to secondary emissions (Wang *et al*., 2017). In addition, the amine scrubbing is energy-intensive, subject to solvent degradation, and associated with toxicity.

On the other hand, physical absorption plays on physical driving forces such as solubility. Physical absorption is well-suited to extracting CO_2 from high-pressure gas streams. The CO_2 is released, and the solvent is regenerated by a pressure swing, similar to opening a can of soda pop. Physical absorption is not suitable for atmospheric flue gases, such as those found at power plants, given its relatively weak driving force.

As opposed to absorption which involves the dissolution of CO_2 in a capture solution, in the adsorption process, CO_2 adheres to the surface of a sorbent in adsorption processes. Adsorption uses porous dry solids with high surface areas, rather than liquid solvents like amines, which are commonly used in absorption. Some noble examples of materials used in adsorption are metal organic frameworks (MOFs) and porous carbon materials, which are deemed ideal candidates for adsorption owing to their outstanding physical and chemical properties (Guo *et al*., 2015). Many scientists have been drawn to solid adsorption technology because of its ease of maintenance, simplicity of operation, and energy savings during adsorbent regeneration (Bai *et al*., 2015).

Membranes are porous structures that allow gas species to move through. Different gases permeate at varying rates, resulting in a separation (Herzog, 2018). Membrane separation is relatively inexpensive, albeit still in its early stages of development, and the application conditions and stability of such materials restrict its widespread use (Chen *et al*., 2018).

With respect to the physical state of the sorbents employed for CC, (Liu *et al.*, 2014) compared liquid absorbents to solid sorbents. According to them, the reason for more extensive adoption of liquid absorption in the industry is two-fold. First, the liquid phase helps one to recover a significant portion of the heat using advanced heat integrations. In comparison, effective heat integration is difficult in solid adsorption. In the absence of heat recovery, the solid-adsorption method becomes less efficient. Second, liquid absorption is amenable to continuous processes with pumping, while the use of solid adsorbent is limited to batch processes which are considered less efficient for CC.

The latter advantage has been echoed from a hands-on perspective by researchers at Carbon Engineering, a direct air capture facility in Canada (Figure 11). According to them, aqueous sorbents have the benefit of allowing the contactor (framework containing the sorbent) to run continuously, and allow for the (liquid) surface to be continually refreshed, which in turn contributes to the durability of contactors even in the presence of dust and other pollutants (Keith *et al.*, 2018).
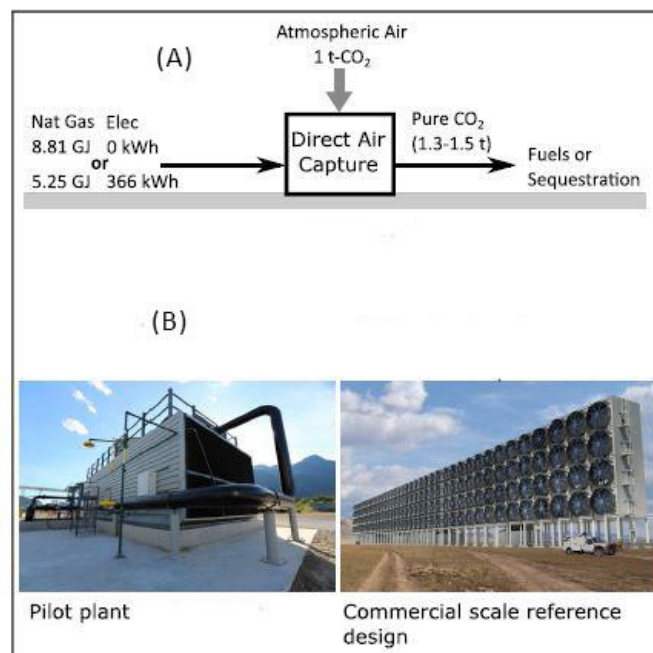
Figure 11: (a) Simple Mechanism of Carbon Engineering's Capture Process (b) Carbon Engineering's Plant Design

According to Azarabadi and Lackner (2020), post-combustion capture, when compared to other carbon capture technologies, is much more advanced because it is comparable to other pollution control technologies. For the most part, this technology is best amenable to operations in a new power plant, even though it can also be readily adapted to retrofitting existing plants. Worthy of note, however, is that retrofitting existing power plants is typically more expensive relative to integrating CCS into a new system (Rao and Rubin, 2002).

Corroborating this motion, (Azarabadi & Lackner, 2020) discovered that the capacity factor, an indication of how much carbon dioxide is captured by a method/material, has the greatest effect on the cost of post-combustion capture. Their findings demonstrated capacity factor to be inversely proportional to cost even for a new power plant.

Conversely, direct air capture (DAC) is still in its early stages, and various groups in the academia and industry have proposed a number of DAC designs, ranging from the use of solid sorbents (passive capture) to forced capture with hydroxide solutions (Sanz-Perez *et al*., 2016; Shi *et al*., 2020; Azarabadi, and Lackner, (2019); Fasihi *et al*., 2019)

From an economic standpoint, (Azarabadi & Lackner, 2020) examined the potential of post-combustion capture technology, as well as the unconventional CC technology, DAC, to counter residual pollution. Since DAC has been demonstrated to fix pollution from any source and directly eliminates CO_2 from the air.

Surprisingly, DAC (which is typically overlooked for point-source capture) could allow for cost savings when addressing emissions from non-retrofittable natural gas combined cycle units. In addition, the residual emissions from retrofitted units can also be fixed by DAC. This technology appears to be a feasible alternative, given the financial implications of post-combustion capture for low utilization natural gas-fired units, such as gas turbines (Azarabadi & Lackner, 2020).

Some of the prerequisite for achieving a high DAC capture efficiency include strong CO_2 affinity, selectivity, and fast kinetics of the sorbent. As a result, chemisorption materials seem to be a better bet for DAC. The basic materials of choice here are aqueous/solid alkaline hydroxides, oxides, and salts (Li *et al*., 2020).

Summarily, non-aqueous sorbents do not appear to be ideal for DAC, particularly given that their use will necessitate significant changes in traditional DAC equipment to reduce solvent loss. There are only a few scalable solid sorbent contactors that can be used for DAC, with the most prevalent used in laboratory scale studies not being scalable owing to very high levels of pressure drop (Kolle & Sayari, 2020).

CHAPTER THREE

EXPERIMENTAL

3.1   Materials

As-preserved mantis shrimp (*Squilla mantis*) and crab (*Carcinus aestuarii*) shells native to the Mediterranean Sea were procured from the Polymer Laboratory, Department of Petrochemicals at the Egyptian Petroleum Research Institute. Sugarcane bagasse was obtained as waste from a local vegetable store. Chemicals used include sodium hydroxide, (Sigma Aldrich, 100.5%) anhydrous sodium chlorite (CDH, 80%), urea crystals (Chemlab, 99.5%), glacial acetic acid (Loba Chemie PNT ltd., 99.5%), (3-aminopropyl)trimethoxysilane (Sigma Aldrich, 97%), tetraethylene pentaamine (Sigma Aldrich, technical grade), halloysite nanoclay (Sigma Aldrich).

3.2   Methods

In this work, the precursor materials and composites were all prepared by chemical methods. The protocols were chosen to fit into the scope of the most extensively employed synthetic route.

3.2.1 Extraction of Chitosan

The exoskeleton (shells) of crustaceans has been demonstrated to comprise chitin, calcium carbonate, and proteins as major fractions. In parallel, chitin, when modified such that the molar fraction of N-acetyl glucosamine moieties falls short of 50%, with respect to the total number of units, gives chitosan. The isolation of chitosan is well-established in the literature and usually involves three major steps viz. deproteinization, demineralization, and deacetylation. Chitosan from squilla (mantis shrimp) and crab shells was isolated according to the method employed by Riofrio *et al.* (2021) while that from whiteleg shrimp was extracted following the protocol by (Nazir *et al.*, 2021). Both methods are similar with respect to the

chemical used but there are slight differences in the treatment steps. Besides, an additional decolorization step to eliminate organic pigments, such as beta-carotene and astaxanthin, was applied while extracting chitosan from whiteleg shrimp shell.

At the outset, the shells (Figure 12 a-c) were thoroughly washed with boiling (tap) water to get rid of adherent flesh residues and unwanted substances. The final washing was done using ultrapure water (type 1) and the shells were dried at 80 ºC for 8 hours in a convection oven. This drying condition was applied in all intervening periods between unit operations and the products of each step were washed thoroughly with ultrapure water until the filtrate attained near-neutral pH.

Following the drying operation, the shells were pulverized using a kitchen blender and fine particles (Figure 12 d-f) were obtained by sieving the pulverized shells through a 250-micron (60 mesh) sieve. For deproteinization and the removal of minor organic molecules, 25 g each of the mantis shrimp and crab powders (MSP and CRP) was subjected to treatment with 250 mL of 1.25 M (5%) sodium hydroxide (NaOH) solution at 70 (±1) ºC to give a 10% W/V solution. The solutions were heated with mechanical stirring on a hot plate stirrer for 2 hours. Deproteinization of the whiteleg shrimp powder (WSP) was carried out given the same conditions with refluxing the solution on a heating mantle in a fume hood. Further the oven-dried MSP and CRP were demineralized with 1N HCl (6.25 % W/V) at room temperature for 48 hours, with constant agitation. The WSP, on the other hand, was demineralized for 48 hours, with 1% (0.33 M) HCl at room temperature, but without stirring. Effervescence of bubbles upon adding HCl gave an indication of the breakdown of carbonates, hence, releasing CO_2 (Figure 12 g and h). Given the rigid matrix of the crab shells, which might make recalcitrant

the proteins and minerals, the deproteinization and demineralization steps were repeated twice and once, respectively.

Prior to demineralization, the WSP was decolorized by immersing the filtered and oven-dried deproteinized shell powder in acetone for 24 hours. Following demineralization, chitin was obtained, and in a final step, chitosan was produced by deacetylation. Typically, chitin samples from MSP and WSP were treated with 50% aqueous NaOH (10 % W/V) at 120 ($\pm$2) °C for 2 and 3 hours, respectively, with mechanical stirring at 500 rpm while that from WSP was obtained using 30% aqueous NaOH for 12 hours with intermittent stirring. The resulting
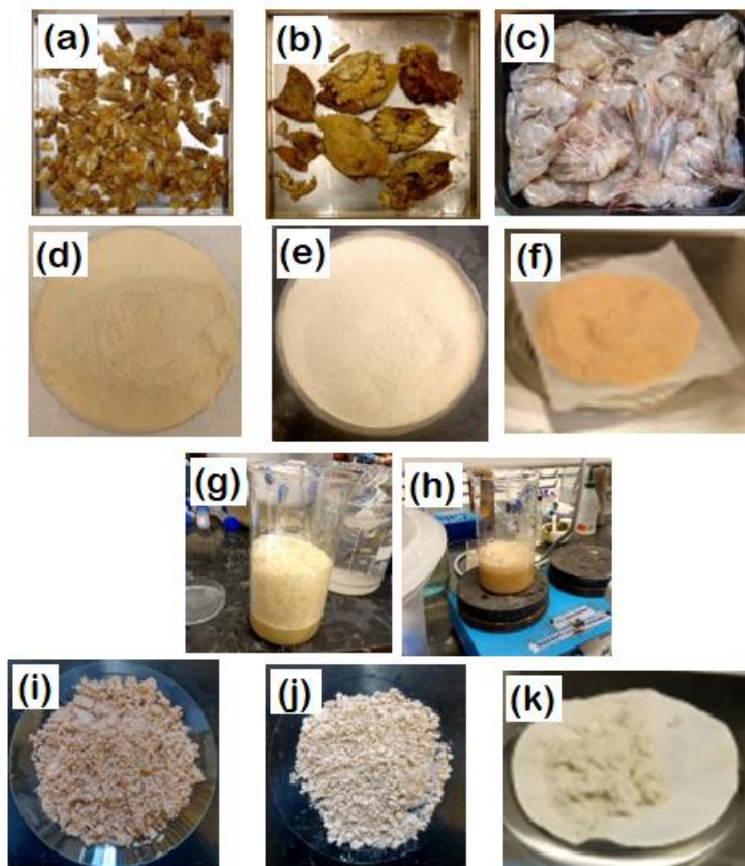
Figure 12: Exoskeletons Of (a) Mantis Shrimp (b) Crab and (c) Whiteleg Shrimp

    Pulverized Shells of (f) Mantis Shrimp (e) Crab and (f) Whiteleg Shrimp

    Effervescence Of CO_2 Bubbles (g & h) During Demineralization Chtosan From (i) Mantis Shrimp (j) Crab and (k) Whiteleg Shrimp

slurries were vacuum-filtered, washed until neutrality and dried in the oven to obtain chitosan as powdery flakes (Figure 12 i-k). The chitosan samples from mantis shrimp, crab shells and whiteleg shrimp were labelled MCS, CRCS, and CS1, respectively. A shortcoming of the preceding approach is the use of harsh chemical and thermal treatments which not only leaves an environmental footprint but also gives a low yield. An alternative, eco-friendly route to extracting chitosan would follow an enzymatic pathway, for instance, would probably be much better (Ilyina *et al.,* 2000).

3.2.2   Isolation of Cellulose

Different materials, including old corrugated containers, wood dust, fig tree branches, and sugarcane bagasse, were explored to prepare cellulose. For brevity and the application intended, only sugarcane bagasse cellulose extraction was described herein. The method to isolate cellulose from sugarcane bagasse (SB) (Figure 13a) was adapted according to the work of (Rungthaworn *et al*., 2020). In a typical synthesis, 5 g of the pre-washed, dried, and blended SB (Figure 13b) was mixed with 100 mL aqueous sodium hydroxide (1M or 4 wt. %), resulting in a 5 % W/V slurry. This was necessary for partial removal of lignin and hemicellulose from the biomass matrix. The reaction mixture was continuously stirred and maintained at 55 °C for 2 hours. Subsequently, following vacuum filtration and oven-drying at 80 °C overnight, an amount of the dried pulp was reacted for 1 hour with 1.4 wt. % (ca. 0.16 M) sodium chlorite (NaClO$_2$) solution to give a 5 % W/V solution. The reaction was maintained at 70 °C for 1 hour and the pH (Jenway 570 portable handheld pH meter) was adjusted to 4.0 with glacial acetic acid. This pH adjustment was necessary to generate a series of species including chlorous acid, chlorine dioxide, and chlorite anion in the aqueous solution. These species facilitate the bleaching of the pulp fibres and further delignification. The spent chlorite was filtered off by vacuum and the treatment was repeated four times.

Figure 13: Isolation of Cellulose from Sugarcane Bagasse

Figure 13 (c & d) illustrate the physical state of the pulp at the start of the second run and the resultant white pulp slurry at the end of the fifth run, respectively. In the final step, the pulp was vacuum filtered, washed until the filtrate pH was close to neutral and dried at 55 °C for 24 hours to give the sugarcane bagasse cellulose (SBC).

3.2.3 Preparation of Sugarcane Bagasse Cellulose Nanocrystals (SBCNC)

CNC suspension from SBC was prepared as described by Dassanayake *et al*. (2017). In a typical synthesis, approximately 1 gram of SBC (Figure 14a) was hydrolyzed in 10 mL of 64% (W/W) sulphuric acid (H_2SO_4) solution. The hydrolysis proceeded at 45 °C for 60 minutes, and the resultant brown solution (Figure 14b) was sonicated in an ultrasonic bath for 50 minutes. To quench the reaction, an excess of cold distilled water was added into the mixture. Several portions of the dispersion were centrifuged and washed in succession at 5000 rpm for 20 minutes to recover the nanocrystals which precipitated at the bottom of the tubes. Finally, the suspension was dialyzed (Figure 14c) against distilled water for 14 days to abolish the acid molecules. During this time, the dialysate buffer was gently stirred and periodically renewed. A portion of the resultant CNC suspension (Figure 14d) was kept for Transmission Electron Microscopy, while another for FTIR, TGA, XRD, and EDS analyses was pre-frozen in a minus 20°C freezer followed by vacuum-freeze drying. Although an industrially established route to

fabricating nanocellulose, the use of extremely high acid concentration is hazardous. Perhaps the material could be alternatively produced by electrospinning.

Figure 14: Preparation of Sugarcane Bagasse Cellulose Nanocrystals

3.2.4. Fabrication of Aerogels

First, 2g each of MCS and CRCS powdered samples were dissolved in 2% (0.33 M) aqueous acetic acid to make 1% W/V and 2% W/V solutions, respectively. The dissolution proceeded with constant mechanical stirring overnight, giving rise to gel-like solutions (Figure 15 a & b). The aerogels were then prepared in facile steps wherein the CNC suspension from sugarcane bagasse was directly mixed with chitosan hydrogels. This was according to the method by (Rizal *et al*., 2021). Typically, the CNC suspension was homogenized at 3000 rpm with the aid of Advanced IR Vortex Mixer and placed in a conventional freezer for 24 hours. In a similar fashion, the chitosan solutions were frozen for 24 hours.

Upon thawing of all solutions at ambient temperature, specific portions of the CNC suspension and chitosan solution were mixed (cf. Table 1) and homogenized with vortex at 3000 rpm. The resultant composite hydrogels (Figure 15 c & d) were degassed in an ultrasonic bath and again frozen overnight.

Depending on the physical properties of the intended functionality, which could impact the process of lyophilization, aerogels could be functionalized either by introducing the

functionality prior to lyophilization (pre-modification) or wet impregnation of ready-made aerogels (post-modification). In light of this, halloysite clay nanotubes (HNT) and (3-aminopropyl) trimethoxysilane (APTMS) were introduced into portions of the chitosan hydrogels (Figure 15 e & f) (cf. Table 1). The mixtures were stirred at 500 rpm for more than 12 hours to disperse the functionalities for proper interaction with the solution. Subsequently, all composite hydrogels, in their respectively containers controlling shape, were vacuum-freeze dried (TOPT-10C Freeze Dryer, Toption Group Co., Limited) for 48 hours, producing the aerogels (Figure 15 g & k). The aerogel comprising CS1 and SBCNC was also prepared according to the preceding procedure. Silane and halloysite modification were thought to introduce -NH_2 functionality and improve the adsorption capacity, given the lumen of the tubes, respectively.

Table 1: Aerogel Composition

Sample	CS1/SBCNC	CRCS/SBCNC	MCS/SBCNC	MCS/HNT	CRCS/APTMS
SBCNC (mL)	8	25	25	-	-
CS1 (mL)	12	-	-	-	-
CRCS (mL)	-	100	-	-	35
MCS (mL)	-	-	50	50	-
HNT (g)	-	-	-	0.1	-
APTMS (mL)	-	-	-	-	1

For post-modification with tetraethylenepentamine (TEPA), 5 mL of TEPA was added to 20 mL methanol with mechanical stirring. Thereafter a sample of MCS/SBCNC aerogel was immersed and the solution was stirred at 200 rpm for 24 hours to allow diffusion of the TEPA solution into the bulk. The modified aerogel was placed in a vacuum oven (Across International Model AT09e) at 50 °C for 24 hours to completely eliminate the methanol solvent. The chemical structures for the functionalities, HNT, APTMS, and TEPA, are presented in the appendix section.
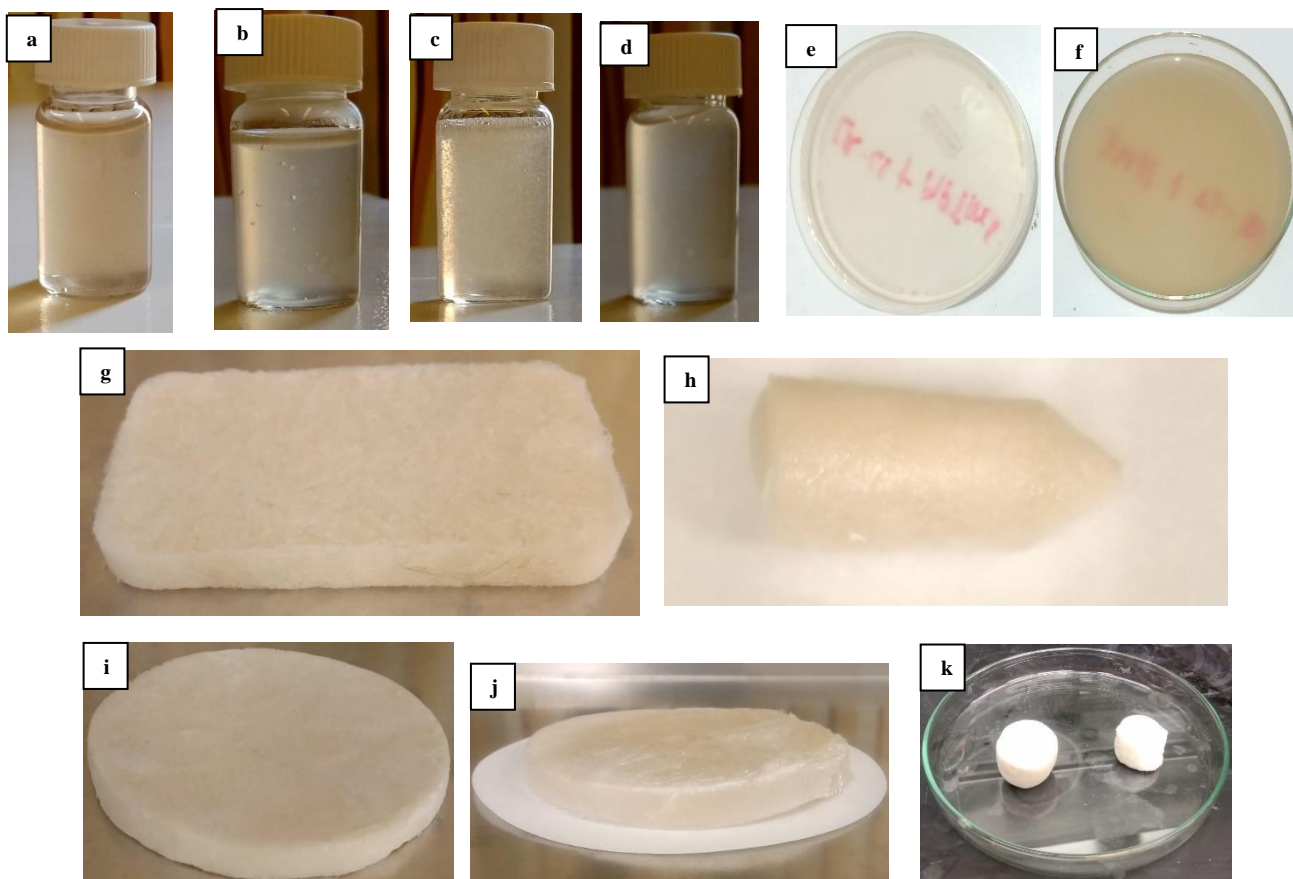
Figure 15: MCS and CRCS Solutions (a and b) Composite Hydrogels (c and d) CRCS/APTMS Hydrogel (e) MCS/HNT Hydrogel (f) CRCS/SBCNC Aerogel (g) MCS/SBCNC Aerogel (h) CRCS/APTMS Aerogel (i) MCS/HNT Aerogel (j) CS1/SBCNC Aerogel (k)

Freeze drying is the most widely employed method for fabricating aerogels but from an economic standpoint, it is a non-starter as it can be both time- and energy-consuming. Besides, the prefreezing process impacts the resultant structure of the aerogel. Liquid nitrogen is often used for this purpose, as opposed to the slow conventional freezing employed herein, since it allows for rapid nucleation of ice crystals without extensive crystal growth. These allows the formation of uniform pore size (monodisperse) following the sublimation of the ice crystals. Nevertheless, it is expensive and might be considered economic only when used a large scale. The schematic for the fabrication of these aerogels is presented in Figure 16 below.
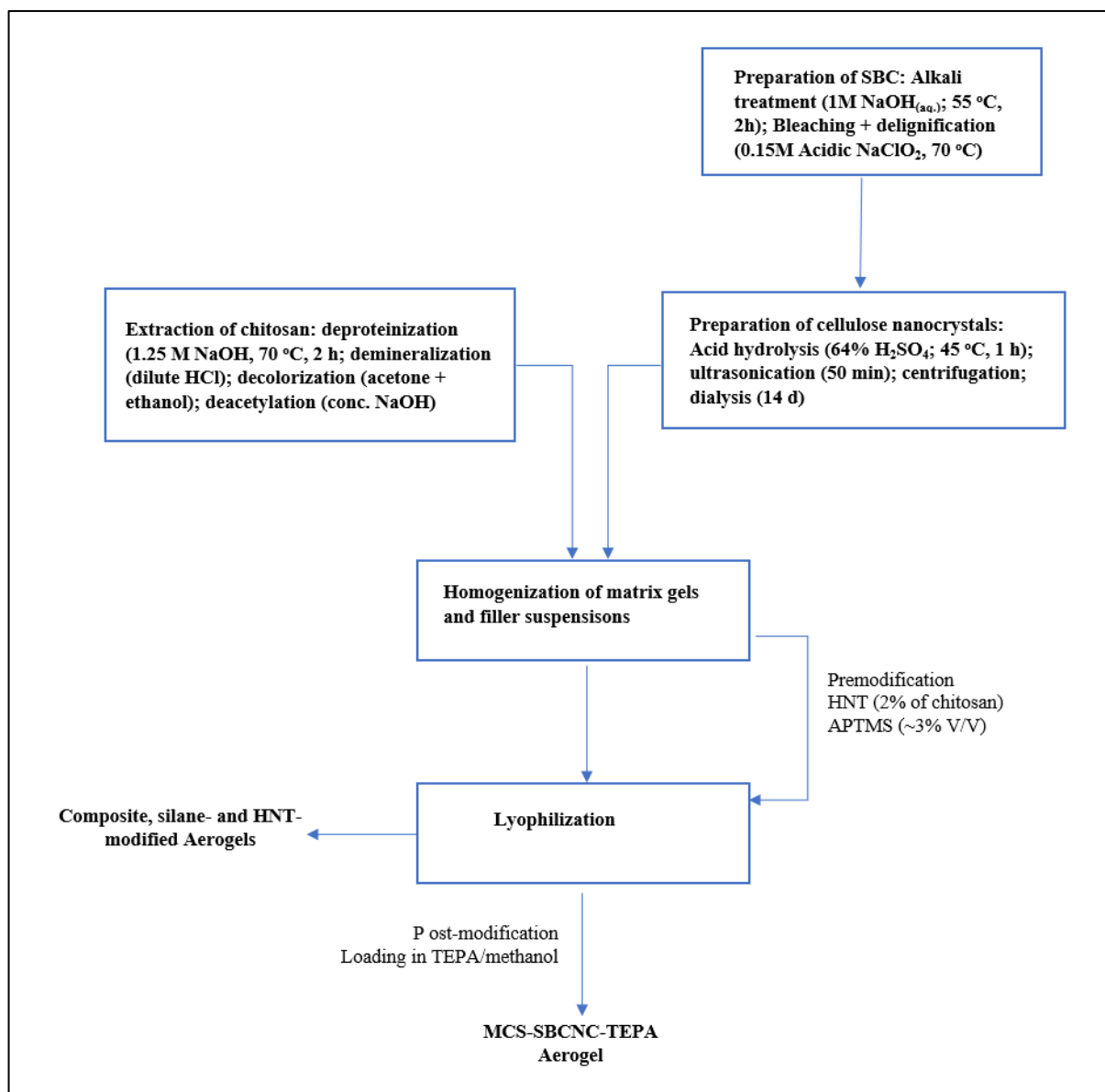
Figure 16: Overall Schematic for Producing the Aerogel Composites

3.2.5 Characterization of Materials

A full physico-chemical characterization is requisite for CO_2 capture candidate materials. In light of this, the following analysis were carried out on the precursors and composites prior to adsorption studies.

3.2.5.1 Molecular Weight of Chitosan

The viscosity-average molecular weights of the chitosan samples were measured using capillary viscometry. For all samples, 0.05 g chitosan was dissolved in 50mL of solvent comprising 0.25M acetic acid (CH_3COOH) and 0.25M sodium acetate monohydrate

($CH_3COONa \cdot H_2O$), giving a 0.1% (0.1 g/dL) solution. Using an Ubbelohde capillary viscometer, the relative viscosity (η_{rel}) was measured as the ratio of passage time of polymer solution to the passage time of pure solvent as the fluids are pumped through the capillary of the viscometer over a marked distance. Serial dilutions of the original solution were made, and the reduced viscosity ($\eta_{sp/C}$) was plotted as a function of concentration. A limitation here is that the procedure was carried out across the different samples under non-isothermal conditions.

Viscometric Parameters:

t = passage time for polymer solution

t_o = passage time for pure solvent

η = viscosity (dynamic or kinematic) of solution

η_o = viscosity in the absence of solute, that is, reference solvent

The t and t_o, as obtained from the viscometer, are directly related to the η and η_o, respectively.

$\eta_{rel} = t/\, t_o$

η_{sp} = specific viscosity = $(\eta/\,\eta_o)_{-1}$ = $(\eta - \eta_o)/\eta_o$ = $\eta_{rel} - 1$

This is denoted as the relative increment in the solution viscosity relative to that of the solvent.

$\eta_{sp/C}$ = reduced viscosity

$[\eta]$ = limiting viscosity number (intrinsic viscosity) = $\lim\limits_{C \to 0} \left(\dfrac{\eta_{sp}}{C} \right)$

A plot of the reduced viscosity versus concentration (Huggin's plot), when extrapolated to the y-axis, that is the intercept, gives the intrinsic viscosity. The viscosity-average molecular weight was finally estimated according to the modified Mark–Houwink–Sakurada equation (Kasaai & Arul, 2000):

$$[\eta] = KM_v^a$$

Where the MHS constants for chitosan in ACOH/ACONa K = 1.57×10^{-4} dL/g and a = 0.79

Q_{MHS} = polydispersity factor = 0.95

Mv = viscosity average molecular weight

But for the modified MHS equation, K = K * Q_{MHS} = 1.57×10^{-4} * 0.95 = $1.49 * 10^{-4}$

Therefore, $[\eta] = 1.49 * 10^{-4} M_v^{0.79}$

The viscosity-average molecular weight is then obtained as

$Mv = ([\eta]/K)^{1/a}$

3.2.5.2 Degree of Deacetylation (DD)

Since the deacetylation of chitin usually leads to the formation of CO_2-phillic amino (-NH_2) groups, it is imperative to properly quantify the degree of deacetylation of chitosan to give a sketch of what application it can be used for. The degree of deacetylation was estimated from FTIR absorbance ratios of amide-I band and O-H band at 1655 cm^{-1} (probe band) and 3450 cm^{-1} (reference band), respectively, using the equation that follows:

$$DD\ (\%) = 97.67 - (26.486\frac{A1655}{A3450}) \qquad \text{(Hussein \textit{et al}., 2013; Sabnis \& Block, 1997)}$$

3.2.5.3 Fourier Transform Infrared Spectroscopy (FT-IR)

The spectra of all the samples were taken with the aid of a Nicolet 380 FT-IR spectrophotometer between 650 and 4000 cm-1, with a scan rate of 64 and resolution of 4. All materials were blended and triturated with excess KBr (FT-IR grade) in an agate mortar and pestle until uniformity. The mixture was then compacted using an IR hydraulic press (Loomis Engineering & MFG. CO.) under a load of 20000 lbs (10 tons) for at least 120 seconds.

3.2.5.4 Energy Dispersive X-ray Spectroscopy (EDX)

Elemental composition of all samples was investigated on a JEOL JCM-6000Plus Versatile benchtop SEM equipped with energy dispersive X-ray spectrometer detector. All samples were irradiated at 15 kV and the spectral analyses were conducted on the JED-2300 Analysis Station software.

3.2.5.5 X-ray Diffraction Analysis (XRD)

The X-ray diffraction patterns of all samples were obtained using a Bruker D8 Advance X-ray diffractometer at 2-theta range between 5° and 50° with a step size of 0.030° and Cu Kα radiation ($\lambda = 1.54$ Å).

3.2.5.6 Thermogravimetric Analysis (TGA)

The thermal stability or the precursor and resultant composite materials was explored on a Labtron (LTGA-A10) Full Auto Thermo Gravimetric Analyzer. 10-15 grams was used across all samples, the TGA was carried out at a ramp of 10 °C/min, and nitrogen was used as purge gas at a flow rate of 40-50 mL/min.

3.2.5.7 Scanning Electron Microscopy (SEM)

The microstructures of the chitosan precursors, HNT and aerogels were observed on an ultrahigh resolution Carl Zeiss (LEO) FESEM between 4 and 6 kV. The samples were all coated with gold at 15 miliamperes for 5 minutes using a HUMMER® 8.0 sputtering system.

3.2.5.8 Transmission Electron Microscopy (TEM) of Cellulose Nanocrystals

Transmission electron microscopy of the SBCNC suspension was observed on a JEOL JEM-2100 electron microscope using an acceleration voltage of 200 kV. The suspension was stained with uranyl acetate solution for the enhancement of microscopic resolution and subsequently dropped on a copper grid coated with carbon-formvar. The electron source is a $LaBr_6$ crystal

filament and the images at different scales and magnification were taken with the Gatan camera software.

3.3 BET Surface Area and Gas Adsorption Analysis

The Brunauer-Emmett-Teller (BET) surface area, nitrogen, and carbon dioxide adsorption analyses of the composites were carried out on the Micromeritics ASAP 2020 surface area and porosity analyzer. BET surface area for all samples were carried out in liquid nitrogen bath at 77 K. For gas (N_2 and CO_2) adsorption at 273 and 298 K, the analysis bath dewar was switched to a chiller dewar. All samples were degassed in vacuum at 393 K for 5 hours prior to each analysis run.

CHAPTER FOUR

RESULTS AND DISCUSSION

4.1   Molecular Weight

The viscosity-average molecular weights (M_v) of the chitosan samples as determined from the Huggin's plot and Mark-Houwink equation show the mantis shrimp and whiteleg shrimp chitosan to be high-molecular weight, while the chitosan obtained from crab was medium molecular weight (Table 2). The Huggin's plot for each sample is presented in the appendix section of this discourse.

Table 2: Viscosity Average Molecular Weights of Chitosan Samples

Sample	M_v (Da)
CS1	431699
MCS	468420
CR-CS	211911

4.2   Degree of Deacetylation

The chitosan sample from crab shell waste presented the highest degree of deacetylation most likely due to its more stringent extraction condition. CRCS had the highest DD of all samples (Table 3), given the relatively harsh deacetylation treatment. All estimated results are tabulated below:

Table 3: Degree of Deacetylation of Chitosan Samples

Sample	DD (%)
MCS	80
CRCS	81
CS1	79

Although, the deacetylation of CS1 was over a longer period of time, is had a slightly lower DD. This indicates the prominence of NaOH concentration and temperature over time of deacetylation.

4.3   FT-IR

FT-IR spectra of the matrix, fillers, and composite materials is depicted in (Figure 17). The chitosan samples exhibited characteristic bands around $1020 – 1200$ cm^{-1} (C-O-C stretching vibrations of the glycosidic linkages) (Hussein *et al*., 2013), 3400-3500 cm^{-1} (overlapping N–H and O–H stretch) (Huang *et al*., 2019), ~1650 cm^{-1} (amide I: C=O) (Esmaeili *et al*., 2021). The bands around 1560 cm^{-1} is ascribed to an overlap of the amide II and N–H bending of amino group) (Lawrie *et al*., 2007), ~1420-1430 cm^{-1} (amide III: C–N stretching vibration) (Esmaeili *et al*., 2021), and just below 3000 cm^{-1} (C–H asymmetric stretch) (Zhang *et al*., 2021). In the spectrum of the mantis shrimp, only one broad band is observed in the ~1650-1560 cm^{-1} region and this is ascribed to an overlap of the amide I with N–H bending. Noteworthy, some spectra exhibited a sharp peak around 2300 cm^{-1}. This peak is ascribable to CO_2 asymmetric stretching collected in the background.

The spectra of SBCNC exhibit several characteristic peaks viz. ~3400 cm^{-1} ascribed to the O–H streching vibration of the free –OH groups on the chain of the cellulose molecule as well as the intermolecular and intramolecular hydrogen bonds the inter and intramolecular hydrogen bonds (Mandal and Chakrabarty, 2014) ~2900 cm^{-1} (C–H stretch); ~ 899 cm^{-1} (assigned to the glycosidic C−H stretching vibration in cellulose molecules, representing the β-glycosidic linkages and the amorphous part in the cellulose structure (Szymanska-Chargo *et al*, 2015), ~1059 cm^{-1} (stretching vibrations of C-O-C bridge in the glycosidic bonds of the cellulose chain), 1632 cm^{-1} (O-H deformation of adsorbed water) (Soni *et al*., 2015).
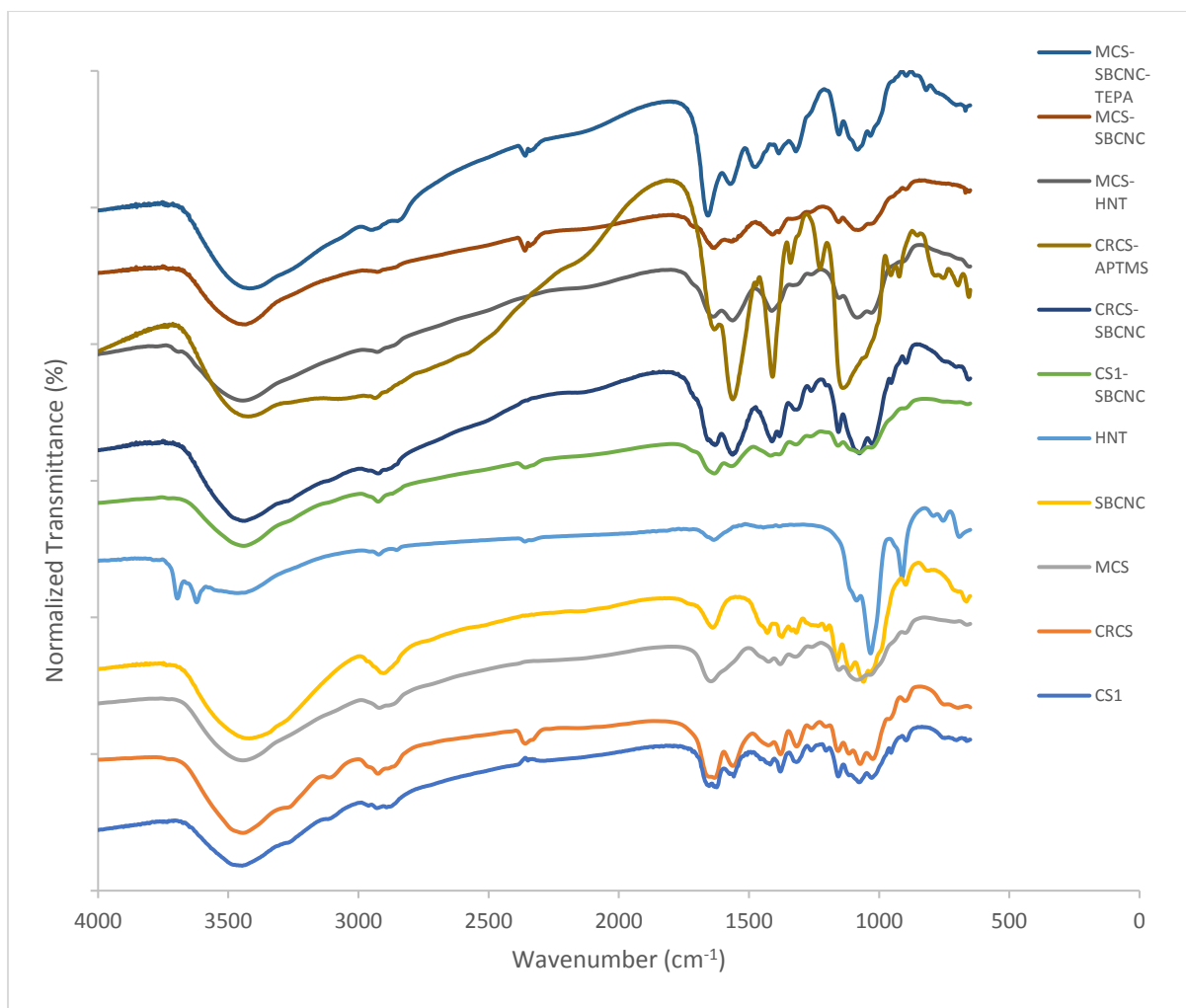
Figure 17: FT-IR spectra of precursor and composite materials

For neat HNT, the peaks observed at 3695 cm^{-1} and 3621 cm^{-1} are assigned to the stretching vibration of internal O-H groups while that at 3467 cm^{-1} corresponds to the O-H stretching of adsorbed water molecules. In-plane Si-O stretching vibrations were observed at 1086 cm^{-1} and 1032 cm^{-1} while the Si–O–Si and perpendicular Si–O–Al stretching vibrations were observed at 791 cm^{-1} and 754 cm^{-1}, respectively. Further, the bands at 1630 cm-1 and 911 cm^{-1} are ascribable to O-H bending of water and inner-surface hydroxyl groups, respectively (Yuan *et al.*, 2008; Kang *et al.*, 2017).

Virtually all the bands assigned to the precursor materials were exhibited in the spectra of the aerogel composites, indicating a successful incorporation of all materials. Noteworthy, these

bands for the aerogels were less intense and, in some cases, broader relative to those of the precursors. The characteristic O−H and N−H stretching vibration intensities of the chitosan samples were abated due to intermolecular hydrogen bonding between the O−H and N−H groups of the chitosan and cellulose molecular chains (Esmaeili *et al*., 2021; Klein *et al*., 2015).

4.4 SEM Imaging

The microstructure of the chitosan samples (Figure 18 a-c) represents intertwined polymeric fibrous networks. Additionally, a heterogeneous surface and porous internal structure were observed (Dotto *et al*., 2012). The fibrillar structure of pure cellulose obtained from sugarcane bagasse is presented in Figure 18d.
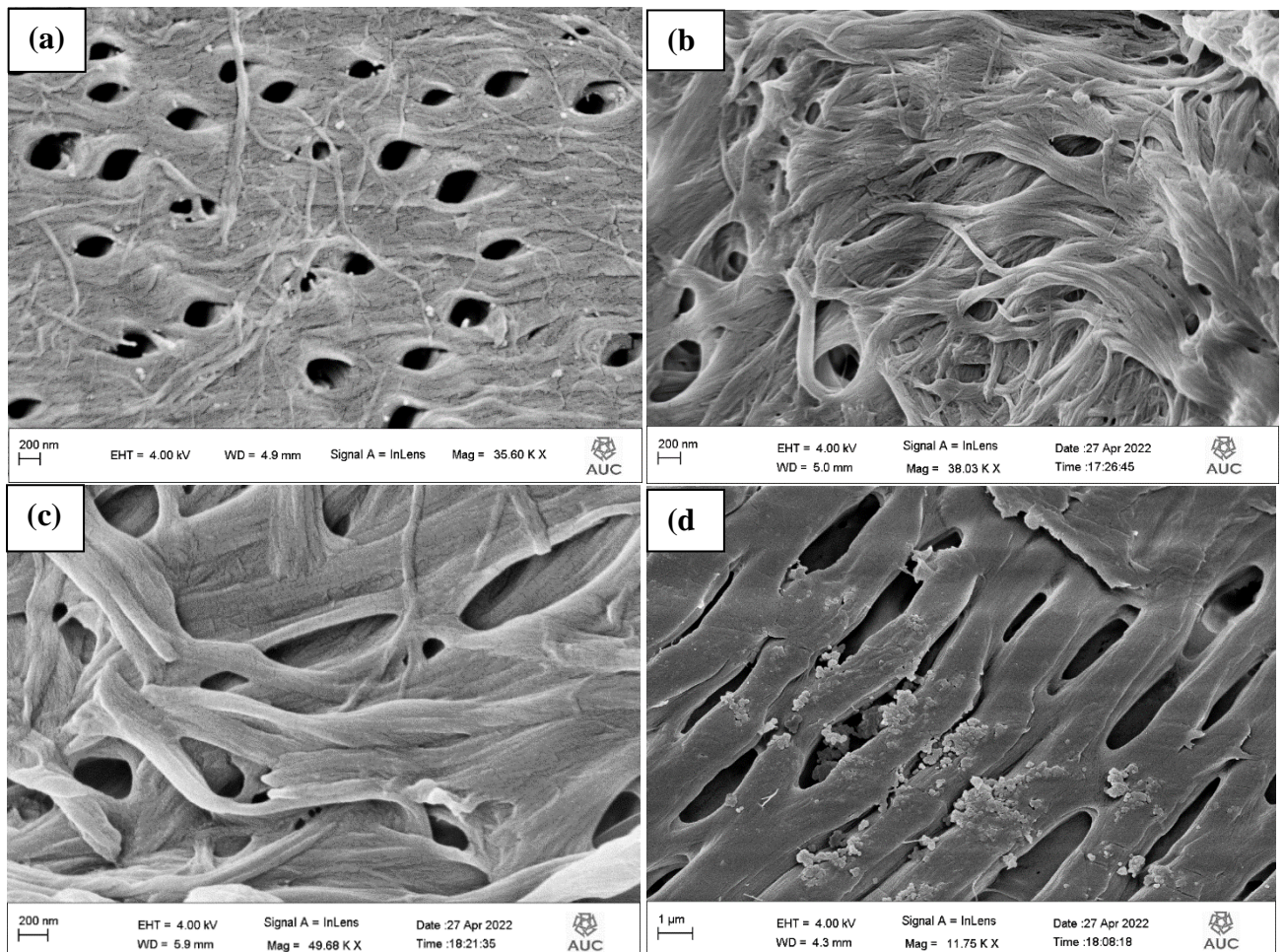
Figure 18: SEM images of (a) CS1 (b) MCS (c) CRCS (d) SBC

The aerogels (Figure 19 a-f) had the structure of platelets loosely arranged to give slit-like pores, facilitating mass transport. This random orientation of the voids probably came from the directional pre-freezing as well as sublimation processes of the ice crystals during lyophilization.
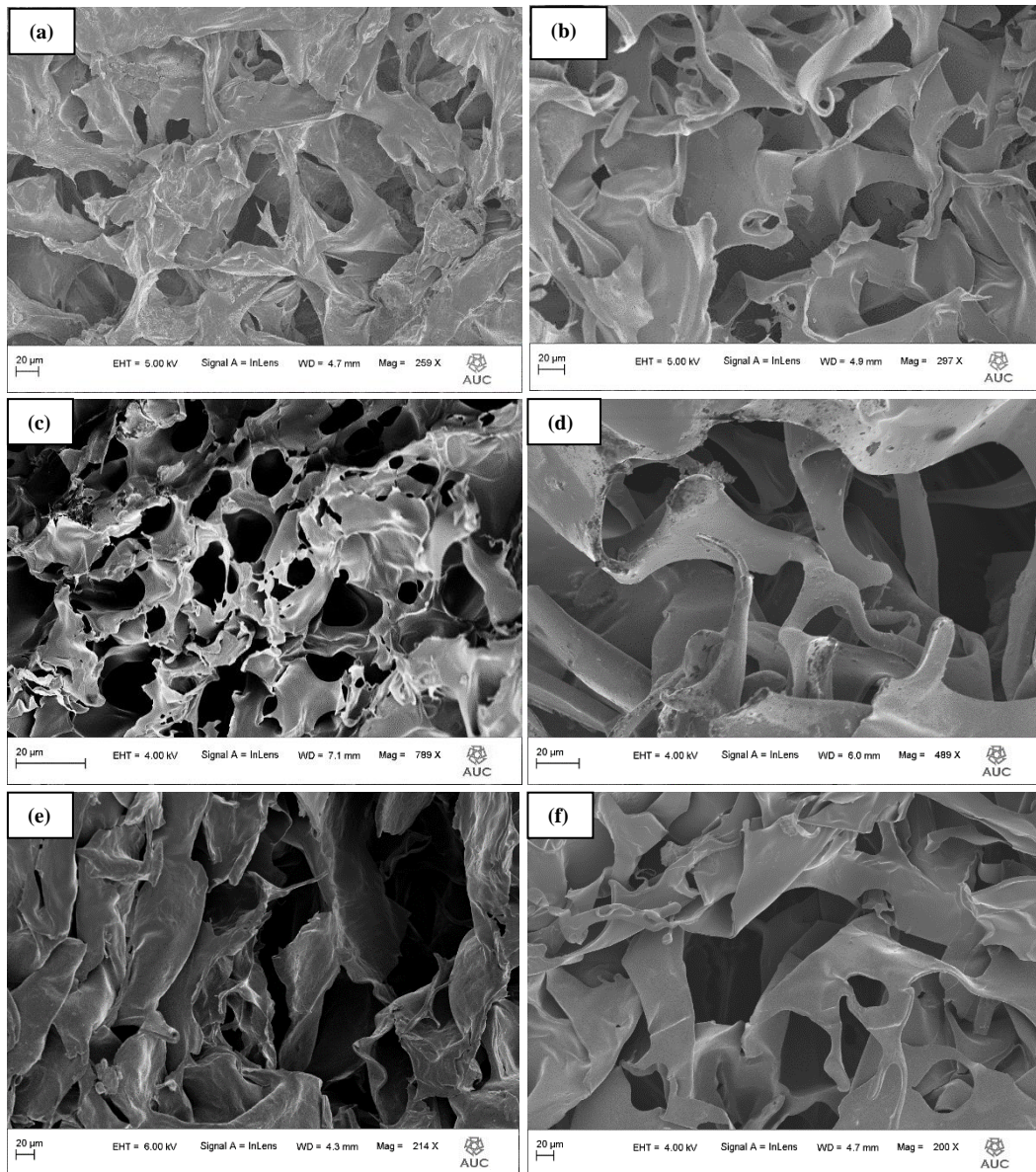
Figure 19: SEM of Aerogel Samples (a) CS1-SBCNC (b) MCS-SBCNC (c) CRCS-SBCNC (d) MCS-HNT (e) CRCS-APTMS f. MCS-SBCNC-TEPA

4.5 TEM Imaging For SBCNC

As could be observed from the high-resolution TEM images (Figure 20 a & b), the SBCNC presents individual needle-like crystals. The aspect ratio taken as a single measurement from

the full-scale of an individual crystallite in a specific area (Figure 20c) is 17.96 *l/w*, much lesser than that estimated for cellulose nanofibers (Xu *et al.*, 2013), hence, suggesting the formation of nanocrystals. The selected area diffraction technique was also employed for the crystal orientation of the material. The ring diffractogram (Figure 20d) obtained from the selected area of the sample depicts that of a polycrystalline, albeit weak, material exhibiting no traces of an amorphous phase.
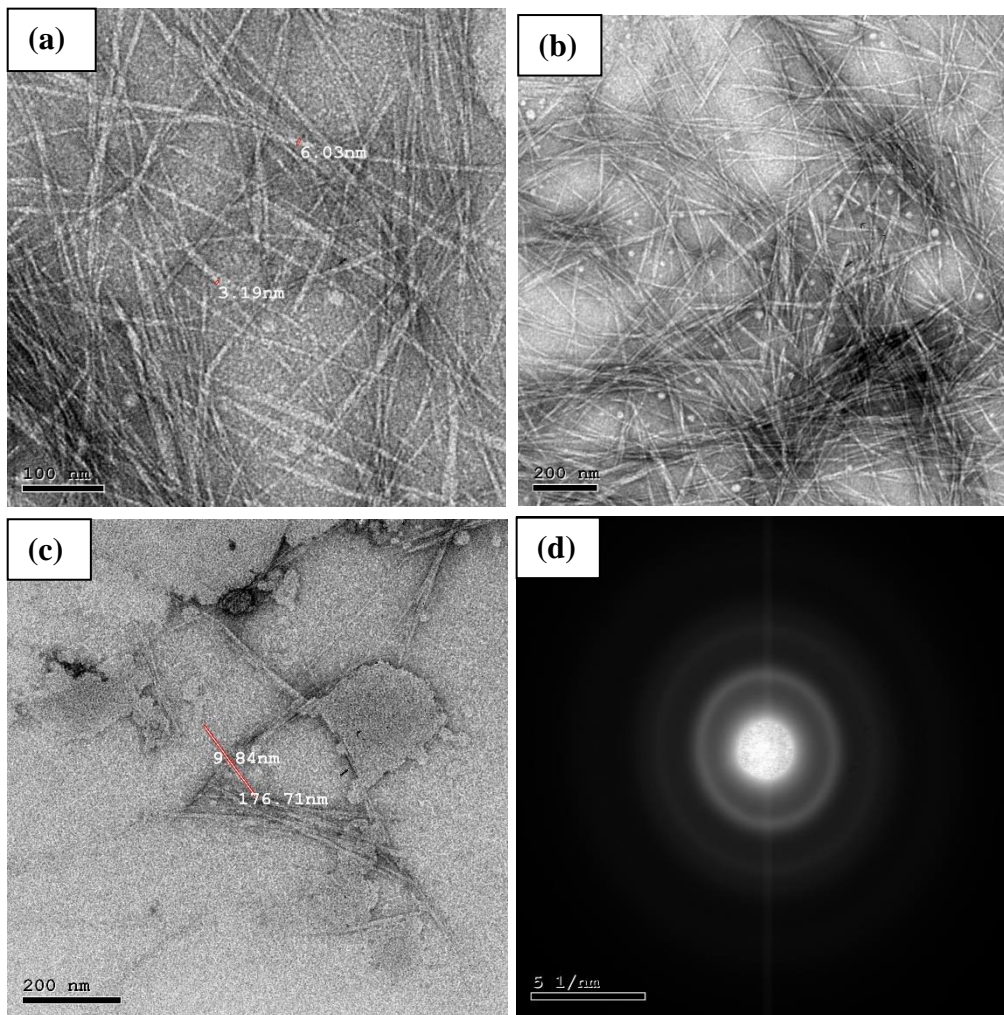
Figure 20: TEM Images of SBCNC on Different Scales (a & b) Individual Fibril (c) and Selected Area Diffraction (d)

4.6 EDS Analysis

As illustrated in Table 4 below, the materials comprised all expected characteristic elements. The cumulative amounts of recalcitrant impurities from the experiments were within permissible levels. Further, the results obtained for the chitosan samples reflect the overall

effect of the treatment steps involved in the extraction as well as the incorporation of

functionalities in the final aerogel composites.

Table 4: Elemental Composition of Precursor and Composite Materials

|		C	N	O	Al	P	S	Ca	Mg	Ni	Si
SBCNC	Mass%	75.86	-	22.37	0.82	-	0.62	-	-	-	0.32
	Atom%	81.23		17.98	0.39		0.25	-	-	-	0.15
WSP	Mass%	67.22	6.52	12.42	0.72	3.58	0.93	8.47	NA	0.06	-
	Atom%	77.48	6.45	10.74	0.37	1.6	0.4	2.93	NA	0.01	-
CS1	Mass%	77.37	3.59	18.62	0.37	-	-	0.04	-	-	-
	Atom%	81.78	3.25	14.77	0.18	-	-	0.01	-	-	-
CS1-SBCNC	Mass%	70.42	3.60	25.13	0.27	0.01	NA	0.06	-	-	0.13
	Atom%	75.83	3.90	20.31	0.13	0.01	NA	0.02	-	-	0.06
MSP	Mass%	34.27	2.58	15.47	4.69	2.18	-	39.63	1.19	-	-
	Atom%	53.98	3.48	18.29	3.29	1.33	-	18.71	0.92		-
MCS	Mass%	70.78	5.71	23.25	0.18	-	-	0.03	-	-	0.06
	Atom%	75.91	5.25	18.72	0.08	-	-	0.01	-	-	0.03
MCS-SBCNC	Mass%	71.64	4.02	23.89	0.25	-	NA	-		-	0.19
	Atom%	76.85	3.70	19.24	0.12	-	NA	-		-	0.09
MCS-HNT	Mass%	67.54	3.91	25.37	1.60	-	-	-	-	-	1.68
	Atom%	73.99	3.58	20.86	0.78	-	-	-	-	-	0.79
MCS-SBCNC-TEPA	Mass%	80.62	8.47	10.38	0.35	-	0.03	-	-	-	0.16
	Atom%	84.06	7.57	8.12	0.16	-	0.01	-	-	-	0.07
CRP	Mass%	21.32	NA	9.90	0.38	1.09	-	63.74	0.57	-	-
	Atom%	42.76	NA	14.91	0.34	0.85	-	38.32	0.57	-	-
CRCS	Mass%	71.29	5.22	23.29	0.12	-	-	0.02	-	-	0.06
	Atom%	76.38	4.79	18.74	0.05	-	-	0.01	-		0.03
CRCS-SBCNC	Mass%	72.76	3.72	23.27	0.17	-	0.08	-	-	-	-
	Atom%	77.80	3.41	18.68	0.08	-	0.03	-	-	-	-
CRCS-APTMS	Mass%	38.74	4.84	25.03	0.78	-	-	-	-	-	30.61
	Atom%	51.57	5.52	25.01	0.46	-	-	-	-	-	17.43

- = not detected ; NA = not analysed

4.7   Thermogravimetry

A summary of the TG profiles of all samples is presented in Table 5 and the TG and DTG curves are presented in Figure 21: (a) TG and (b) DTG Profiles of Precursors and Aerogels, respectively. The first event of weight loss across the precursor chitosan samples and SBCNC occurred between 26 and 163 $^{\circ}$C, the low temperature region, evidenced by the broad minimum peaks on the differential thermograph (Figure 21b), with the MCS accruing the highest rate of this loss (9.2%), which occurred at ca. 72 $^{\circ}$C. Such weight loss is often ascribed to the desorption of bound water molecules (Turci *et al*., 2015). For the aerogels, MCS-SBCNC-TEPA exhibited the highest rate of degradation in this region, losing about 11% of its weight, as shown on the DTG curve. Similarly, this is ascribed to the loss of adsorbed water, with the highest rate occurring at 93 $^{\circ}$C.

The SBCNC sample had the lowest onset temperature of degradation of all samples (temperature at which degradation is initiated) at ca. 142 $^{\circ}$C. Besides, its degradation occurred over a wide range, showing three prominent pyrolysis events, one between 142 and 270 $^{\circ}$C, a brief process between 290 and 366 $^{\circ}$C, and a third between 400 and 480 $^{\circ}$C, with similar behaviour to the first degradation step. This multi-step degradation has been attributed to the presence of free end chains which begin to decompose at low temperatures as well as the presence of free sulphate ends, emanating from the acid treatment, on the surface of the crystals (Wang *et al*., 2007; Fern *et al*., 2018).

In all, the degradation temperatures of the materials show them to be fairly suitable for post-combustion capture, considering the flue gas temperature (45 – 50 $^{\circ}$C) when cooled.
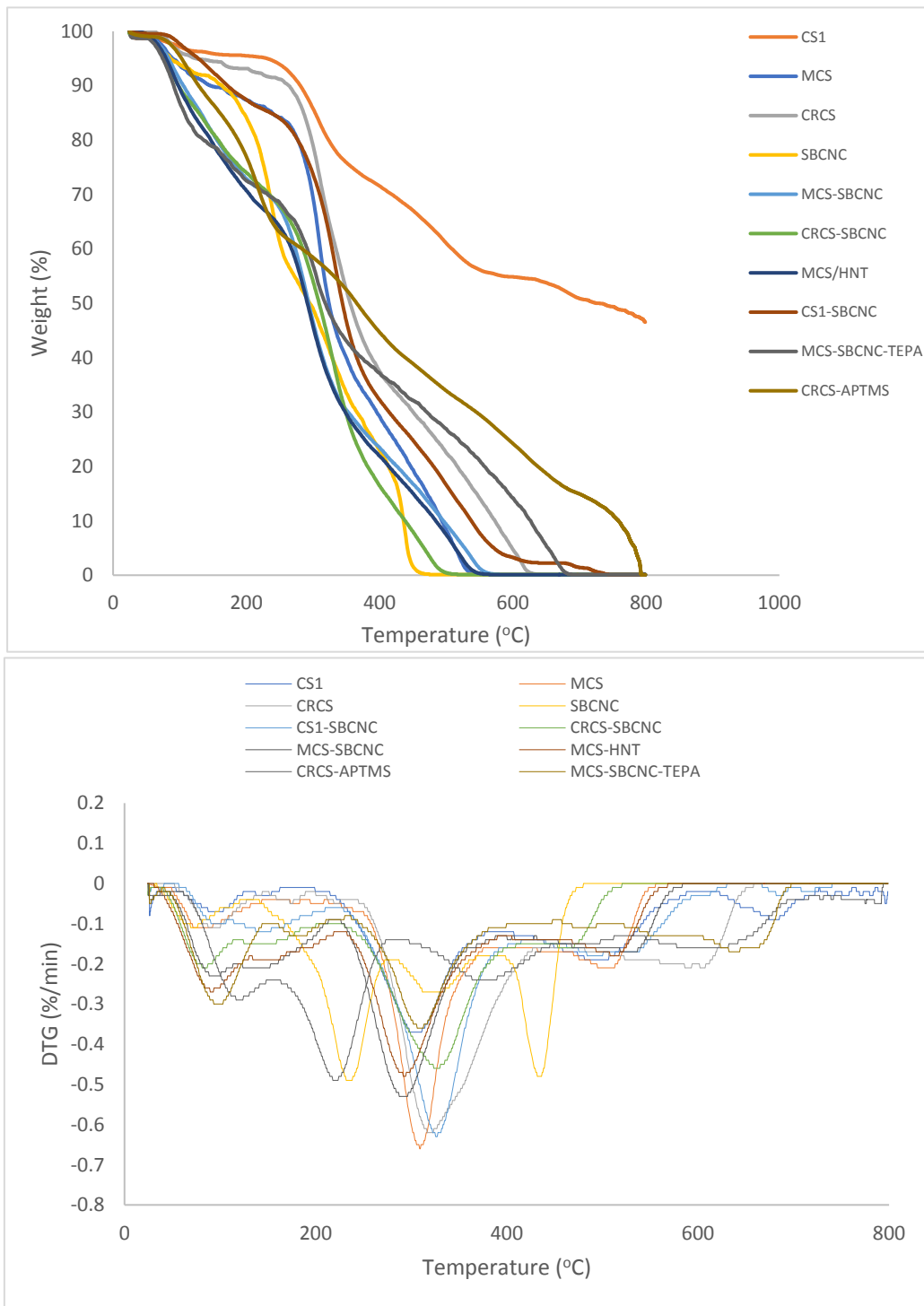
Figure 21: (a) TG and (b) DTG Profiles of Precursors and Aerogels

Table 5: Onset Degradation Temperature (T_o), Maximum Degradation Temperature (T_{max}), and Weight Loss (WL) of All Events

Sample	T_0 (°C)	First event		Second event		Third event	
		Tmax	WL (%)	Tmax	WL (%)	Tmax	WL (%)
CS1	215	305	22	485	16	680	4
MCS	227	310	59	505	21	-	-
CRCS	252	323	68	603	25	-	-
SBCNC	142	236	41	314	28	435	22
CS1-SBCNC	230	326	59	484	17	686	-
MCS-SBCNC	228	296	54	520	16	-	-
CRCS-SBCNC	230	329	69	-	-	-	-
MCS-HNT	233	294	54	512	12		
CRCS-APTMS	164	222	26	368	29	583	30
MCS-SBCNC-TEPA	162	175	8	311	38	634	32

4.8   X-ray Diffraction

The XRD pattern for the precursor matrices, CS1, CRCS, and, MCS (Figure 22) showed two prominent peaks around $2\theta = 9.7°$ and $2\theta = 19.6°$, attributable to chitosan (crystal II form) with a regular crystalline structure (Esmaeili *et al*., 2021; Sarkar *et al*., 2017). For SBC, the peaks observed around $2\theta = 16.4°$, $22.5°$, and $35.0°$, are characteristic of cellulose's native structure (Rungthaworn *et al*., 2020; Klemm *et al*., 2005). With the exception of the peak at $2\theta = 35.0°$ and an overall reduction in peak intensity, SBCNC had the characteristic diffraction pattern of SBC, suggesting preservation of crystallinity. These results for SBC and SBCNC are echoed by the SEM and TEM micrographs, respectively, which depict a repetitive orderly arrangement of the fibres and crystallites. The XRD diffraction pattern of the other filler, HNT, is not

included in this study, but that of the aerogel, MCS-HNT, revealed broad shoulders with no sharp peaks.
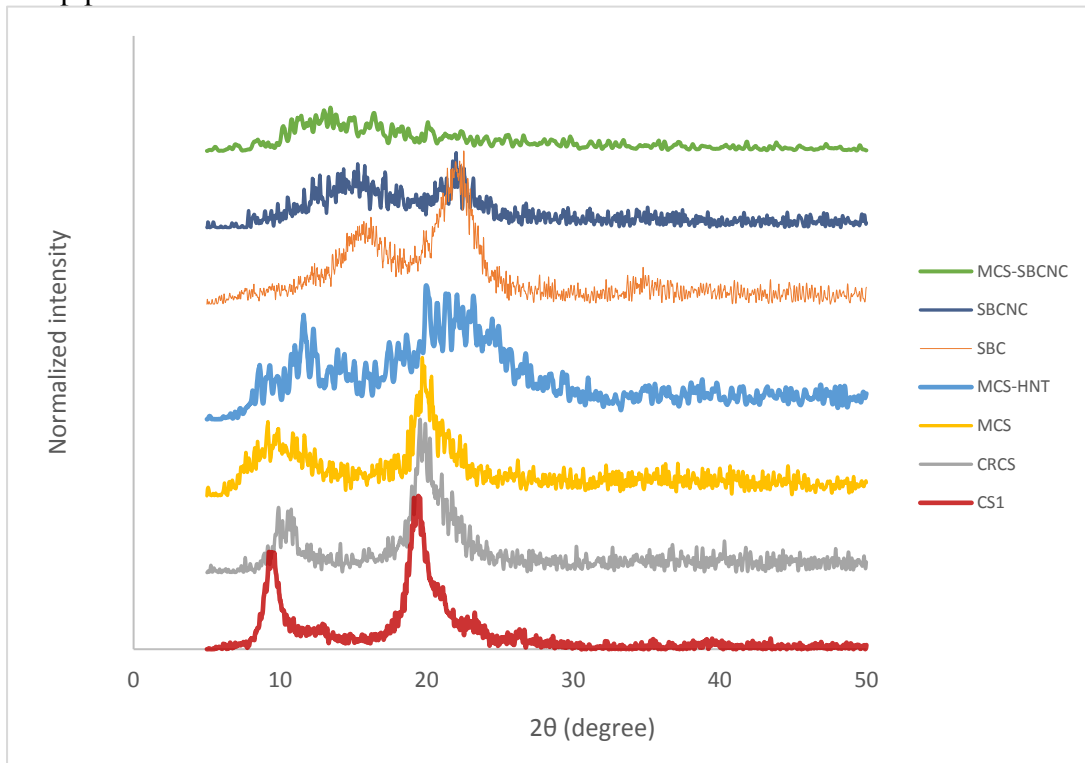
Figure 22: X-ray Diffraction Patterns of Matrices, Filler and Select Composites

The additional peaks observed around $2\theta = 12°$ and $24.8°$ are characteristic of HNT's crystal plane (Ünügül & Ugur, 2022; Barman *et al*., 2020). For the most part, amorphous regions were observed for MCS-SBCNC. The disappearance of the peaks was probably consequent upon rendering the matrix as an aerogel, and this amorphous structure was also observed on the SEM micrograph.

4.9   BET Surface Area Analysis

As illustrated in Figure 23, all aerogel samples presented type-IV isotherms with narrow H_3 hysteresis (IUPAC classification), probably due to filling and emptying of the mesopores. The aerogel composite functionalized with TEPA had the highest surface area (2.15 m^2/g)

Table 6), probably resulting from its prolonged exposure to heat treatment following post-

Aerogels	SABET	Average pore size (nm)	CO2 uptake (mg/g) T = 273 K	T = 298 K	Qst, CO2 kJ/mol	N2 uptake (mg/g) T = 273 K	T = 298 K
CRCS-SBCNC	1.8430	9.1839	2.151713	1.991877	15.415	-2.18813	-3.51234
MCS-SBCNC	1.2631	10.0198	1.868124	1.601047	9.131	-2.31516	-3.81565
CS1-SBCNC	1.2842	29.4157	5.781699	2.072777	9.465	-2.36622	-10.6719
CRCS-APTMS	0.5169	11.4999	2.838632	2.827657	0.941	-1.34948	-2.27769
MCS-HNT	1.1588	55.2853	1.338539	1.376431	23.907	-2.21721	-3.34458
MCS-SBCNC-TEPA	2.1540	5.1527	4.727095	1.296027	38.998	-0.5555	-78.2531

modification, which in turn lead to a negligible material loss.

The neat CRCS-SBCNC aerogel had a comparable surface area (1.84 m^2/g) to the aforementioned, arising from its slightly different lyophilization process. Its hydrogel had been placed in a relatively wide container which allowed a more rapid conduction, sublimation, and, hence, drying of the aqueous solvent.

There was a decrease in surface area for the aerogels modified with APTMS and HNT, perhaps due to the pore-blocking effect of these functionalities as could be seen on the SEM micrographs. Compared to the literature, all the aerogels present significantly lower BET surface areas, with the least reported in the literature, to the best of my knowledge, being 9.74 m^2/g (Liu *et al*., 2021).
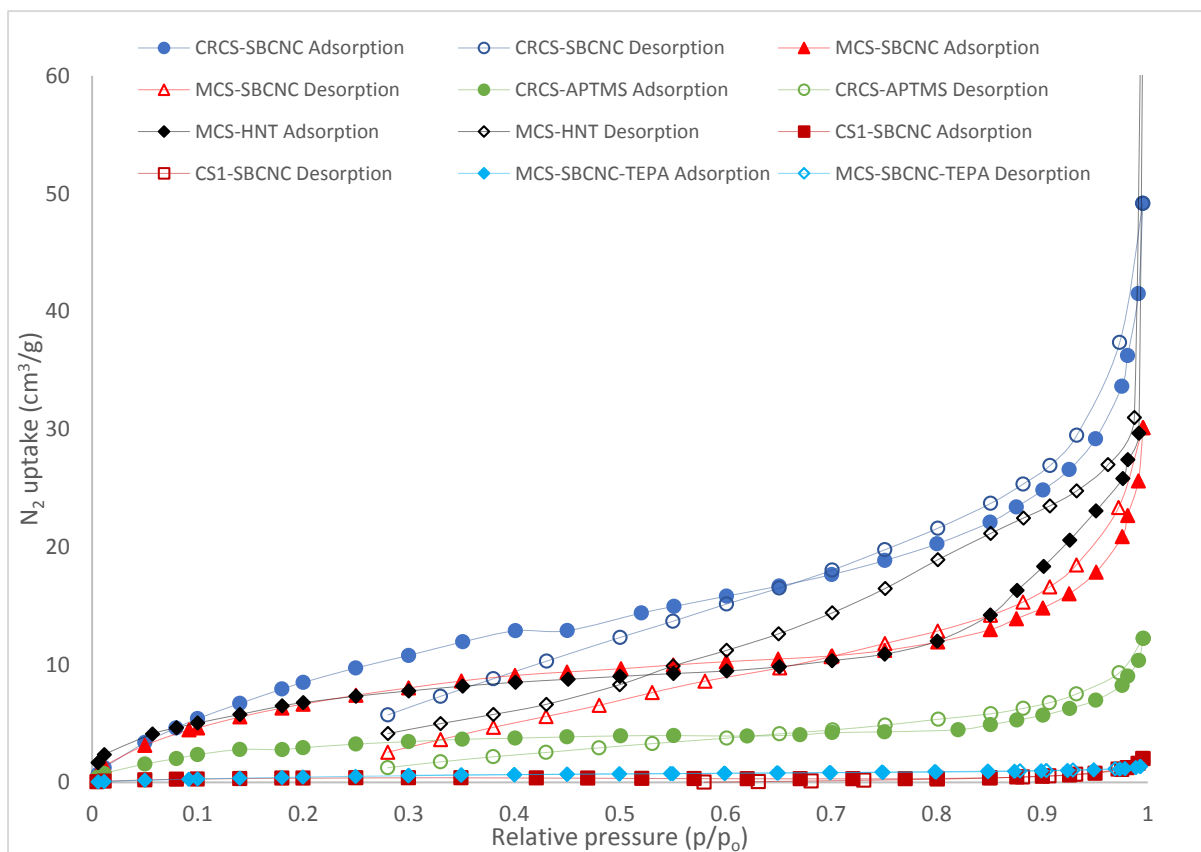
Figure 23: N₂ Adsorption-Desorption Isotherms of the Aerogels

4.10 Gas Adsorption Studies

The CO_2 adsorption-desorption isotherms at 273 and 298K as presented in Figure 24 a and b below indicate that the CS1-SBCNC aerogel had the highest sorption capacity a 273 K, while the CRCS-APTMS sample had the highest at 298 K, which is relatively closer to industrial post-combustion capture condition (Dawson *et al.*, 2011). This value was observed for the aerogel despite the fact that it had the lowest surface area (0.5169 m^2/g). The rationale for this observation draws on the inference that the CO_2 capacity of physisorbents is not a mere factor of surface area but also the presence of CO_2-phillic moieties such as nitrogen (Zulfiqar *et al.*, 2016). Shockingly, the TEPA-functionalized aerogel had the lowest capacity at 298 K. This probably resulted from a 1.2 mg gain in sample weight prior to the analysis run, attributable to inefficient degassing operation. Consequently, adherent molecules most likely hindered mass transfer and contributed a pore-blocking effect, hence, compromising the sorption capacity of the aerogel. The HNT-functionalized material also performed relatively poorly, perhaps due to aggregation of the nanotubes within the matrix.

As illustrated in (Figures 24 a and b), at 273 and 298K all of the samples exhibited negligible adsorption of nitrogen gas at low pressure values which further transited into the negative adsorption phenomenon at higher pressures. This behaviour gives an indication of the experimental selectivity of the materials, considering the CO_2 adsorption profiles.
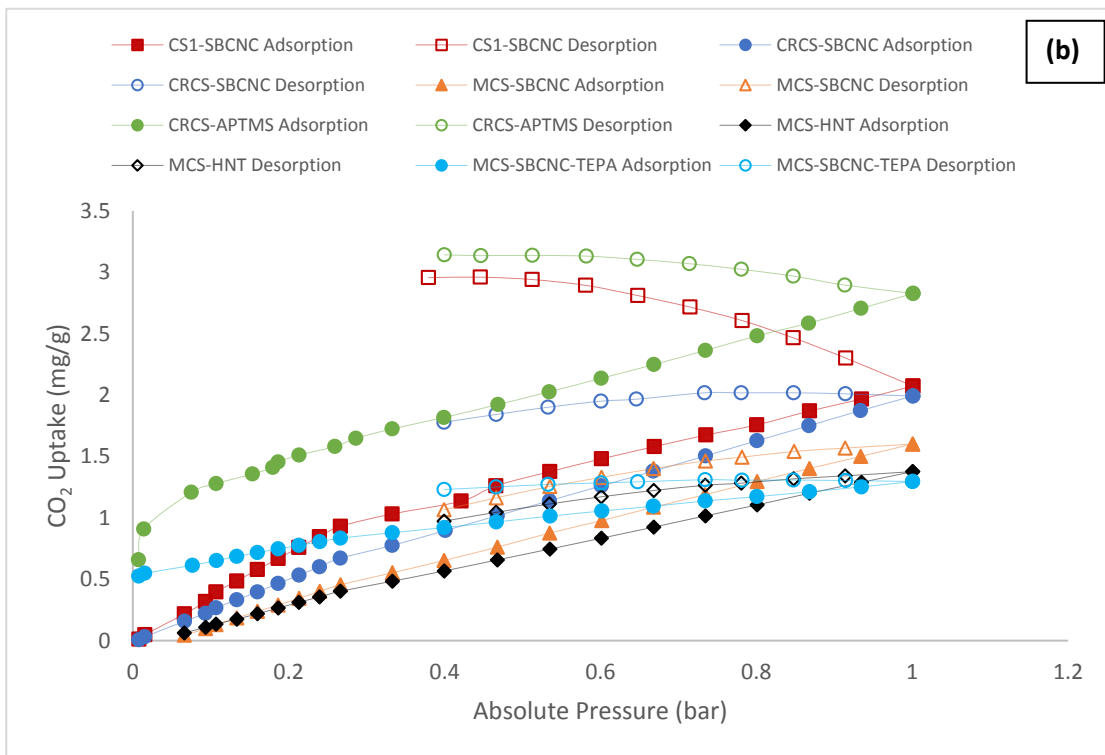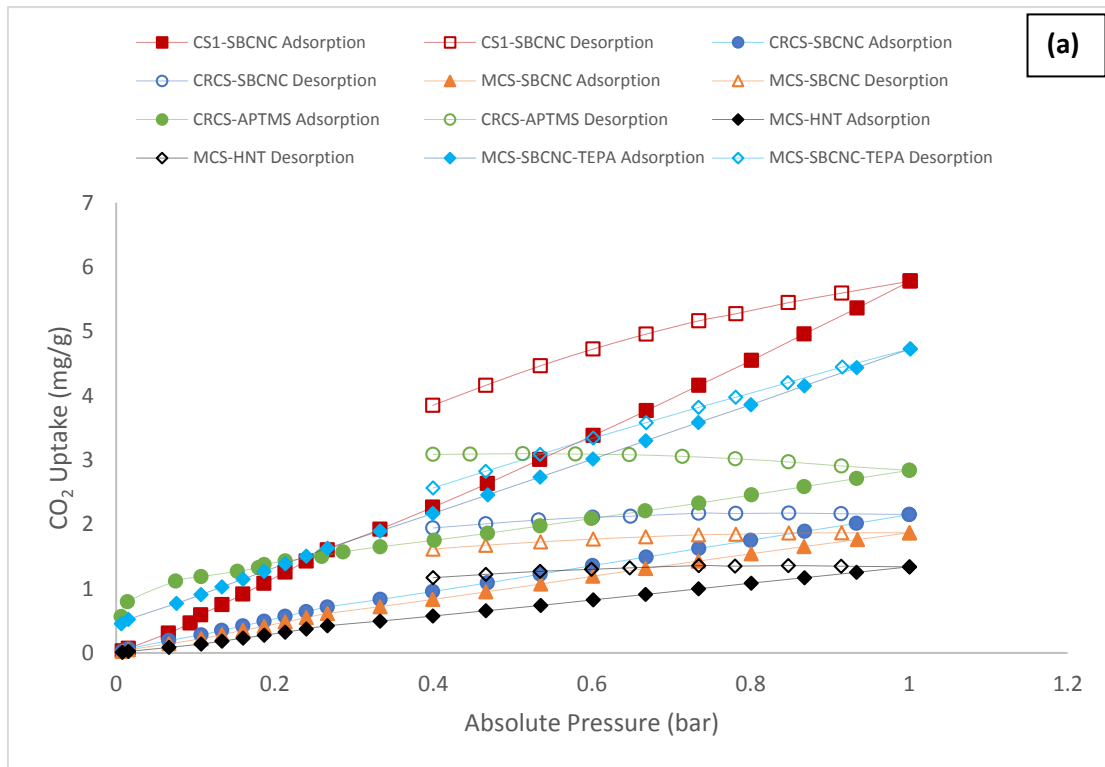
Figure 24: CO$_2$ adsorption-desorption isotherms at (a) 273K and (b) 298K
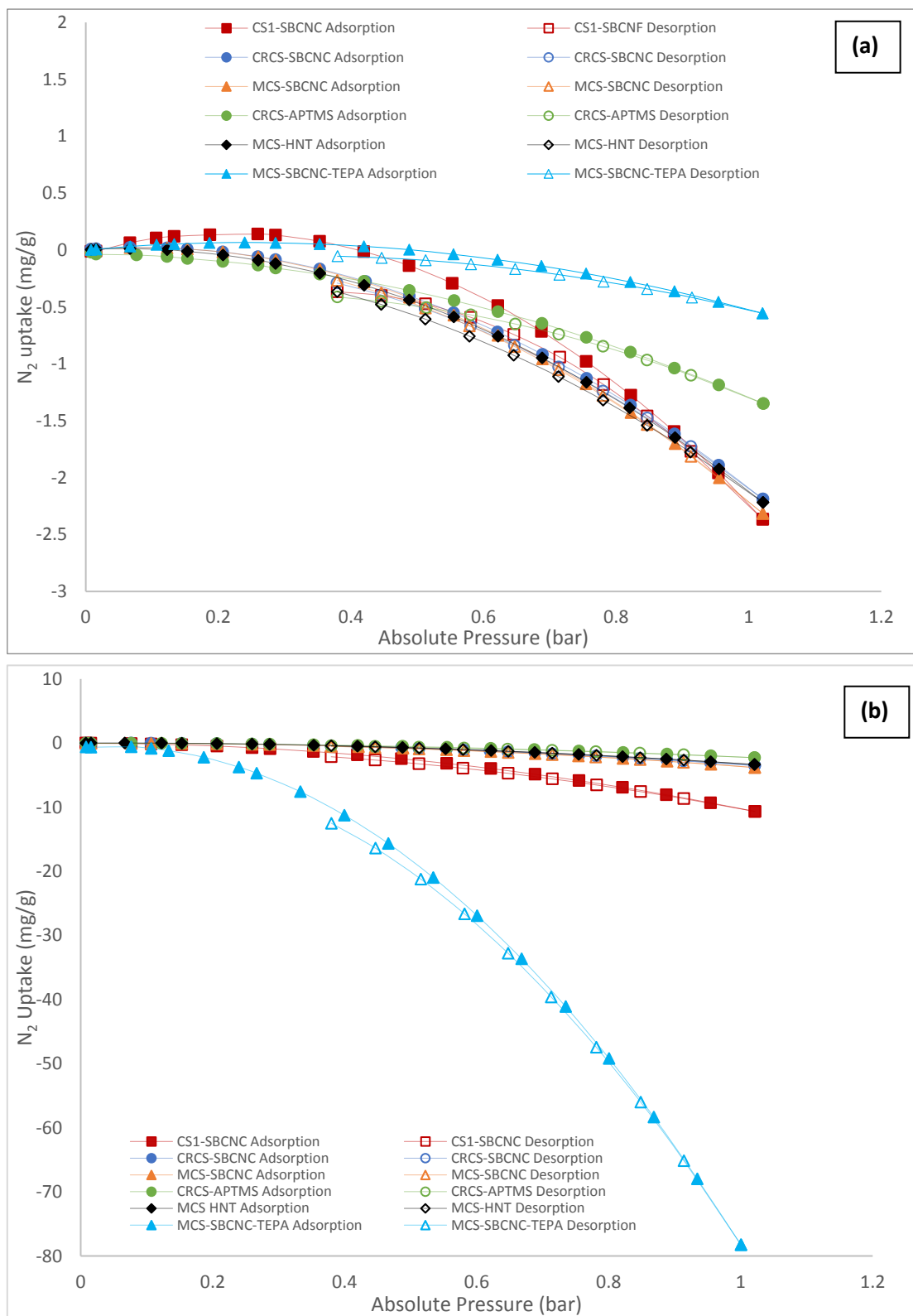
Figure 25: N_2 Gas Adsorption-Desorption Isotherms at (a) 273K and (b) 298K

Table 6: BET Surface Area (SA$_{BET}$), BJH Adsorption Average Pore Aiameter, CO$_2$ and N$_2$ Capacity at 273 K and 298 K , 1 bar, Isosteric Heat of CO$_2$ Adsorption (Qst, CO$_2$)

Aerogels	SA$_{BET}$	Average pore size (nm)	CO$_2$ uptake (mg/g) T = 273 K	T = 298 K	Qst, CO$_2$ kJ/mol	N$_2$ uptake (mg/g) T = 273 K	T = 298 K
CRCS-SBCNC	1.8430	9.1839	2.151713	1.991877	15.415	-2.18813	-3.51234
MCS-SBCNC	1.2631	10.0198	1.868124	1.601047	9.131	-2.31516	-3.81565
CS1-SBCNC	1.2842	29.4157	5.781699	2.072777	9.465	-2.36622	-10.6719
CRCS-APTMS	0.5169	11.4999	2.838632	2.827657	0.941	-1.34948	-2.27769
MCS-HNT	1.1588	55.2853	1.338539	1.376431	23.907	-2.21721	-3.34458
MCS-SBCNC-TEPA	2.1540	5.1527	4.727095	1.296027	38.998	-0.5555	-78.2531

Further, the heats of CO$_2$ adsorption of the aerogels, as determined isosterically (constant coverage) from the adsorption isotherms at 273 K and 298 K, were in the range of ca. 1 - 39 kJ/mol. (Table 6) These values are well below those for chemisorption ($\geq$ 80 kJ/mol) (Abdulsalam *et al*., 2020; Delavar, *et al*., 2012), indicating that the mode of bonding between the adsorbate (CO$_2$) and the adsorbents (aerogels) is driven by weak physical interactions such as Van der Waals forces. By extension, this type of interaction makes it easy to regenerate/reuses the materials for further adsorption with an overarching advantage of energy savings.

CHAPTER FIVE

CONCLUSION AND OUTLOOK

The study presented encompassed an investigation, on a first-time basis, of the carbon dioxide capture capacity of aerogel composite materials based on chitosan and cellulose nanocrystals prepared by the freeze-frying operation. Although the adsorbents presented relatively low CO_2 capacities when compared with established physisorbents, such as metal organic frameworks, their selective interaction with CO_2 over N_2 gas, coupled with the idea of utilizing waste materials for their production, shows good prospects, hence, opening up possibilities to optimize their performance. Additionally, their isosteric heats of adsorption were in the physisorption region, signifying a less energy-intensive mode of regenerating the adsorbents in practical settings.

Since it is crucial to fully explore the mechanical and textural properties of candidate adsorbents for carbon dioxide capture, an intricate approach will be adopted in a prospective study to investigate the effect of the filler in the composite matrix and on the porosity of the adsorbent as well as the contribution of crosslinkers to the structural integrity of polymeric aerogel composites. Likewise, the adsorption of CO_2 on post-modified aerogels using fluidized bed systems, breakthrough CO_2 adsorption studies, and regeneration of adsorbent would be explored. Further, the design of the chemical and electrochemical conversion of CO_2 into value-added products will be a subject of future study.

In all, given that the carbon dioxide capture technology is largely still in transition, the current effort corroborates the scientific idea to continually develop existing materials and fabricate newer ones to consolidate the credibility, validity and viability of this environmentally beneficial technology.

APPENDIX
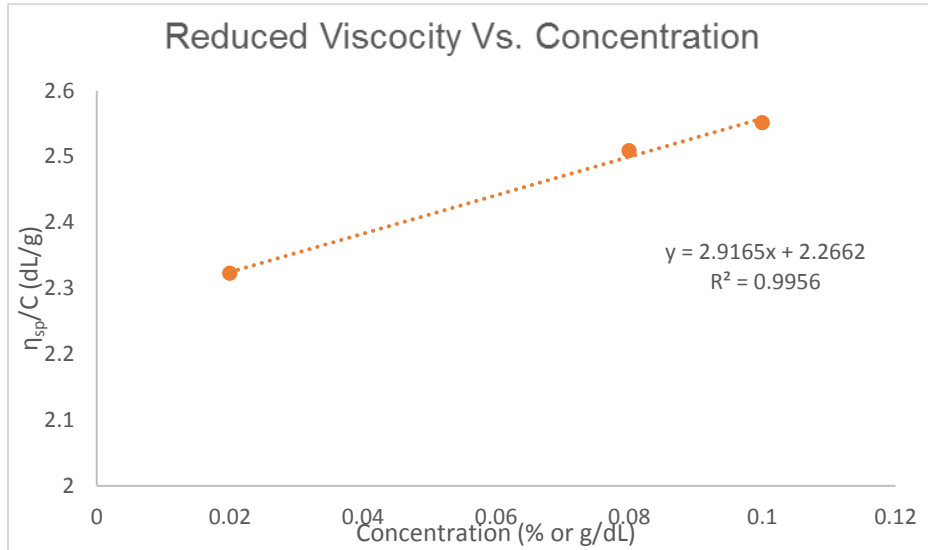
Figure 26: Huggin's plot for CRCS
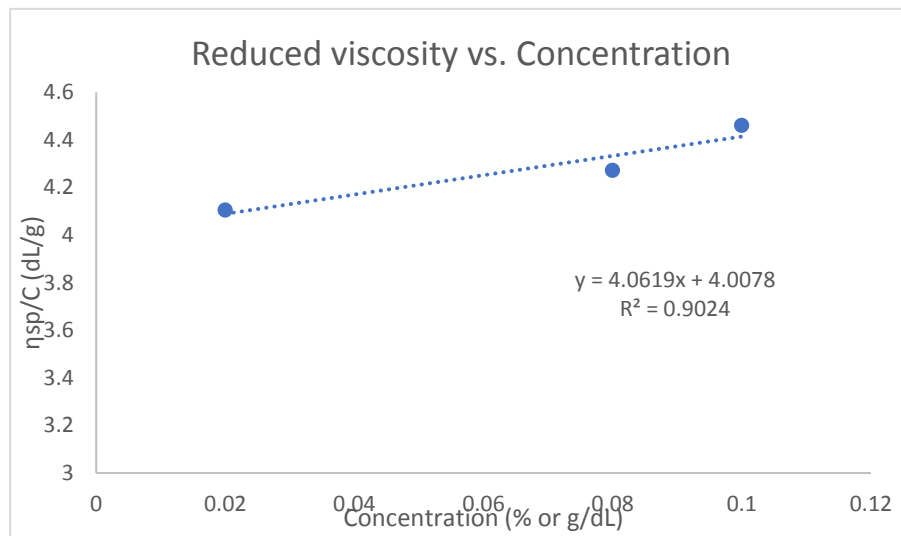
Figure 27: Huggin's plot for CS1
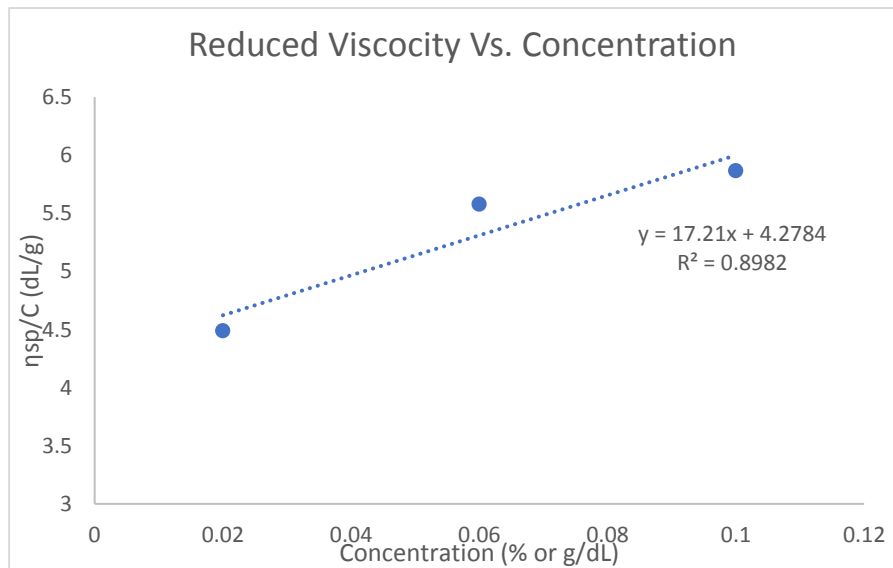
Figure 28: Huggin's plot for MCS
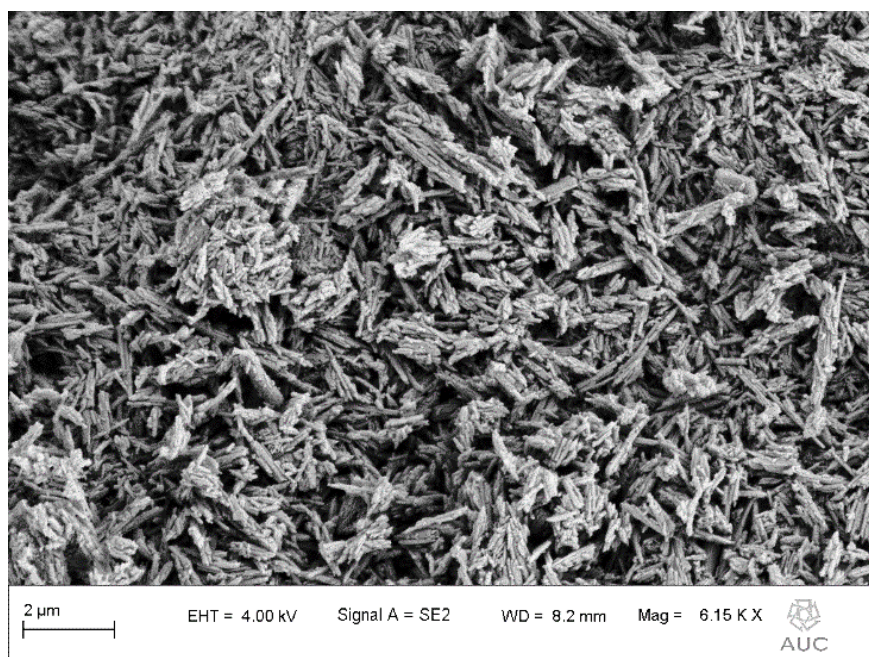
Figure 29: SEM micrograph of HNT
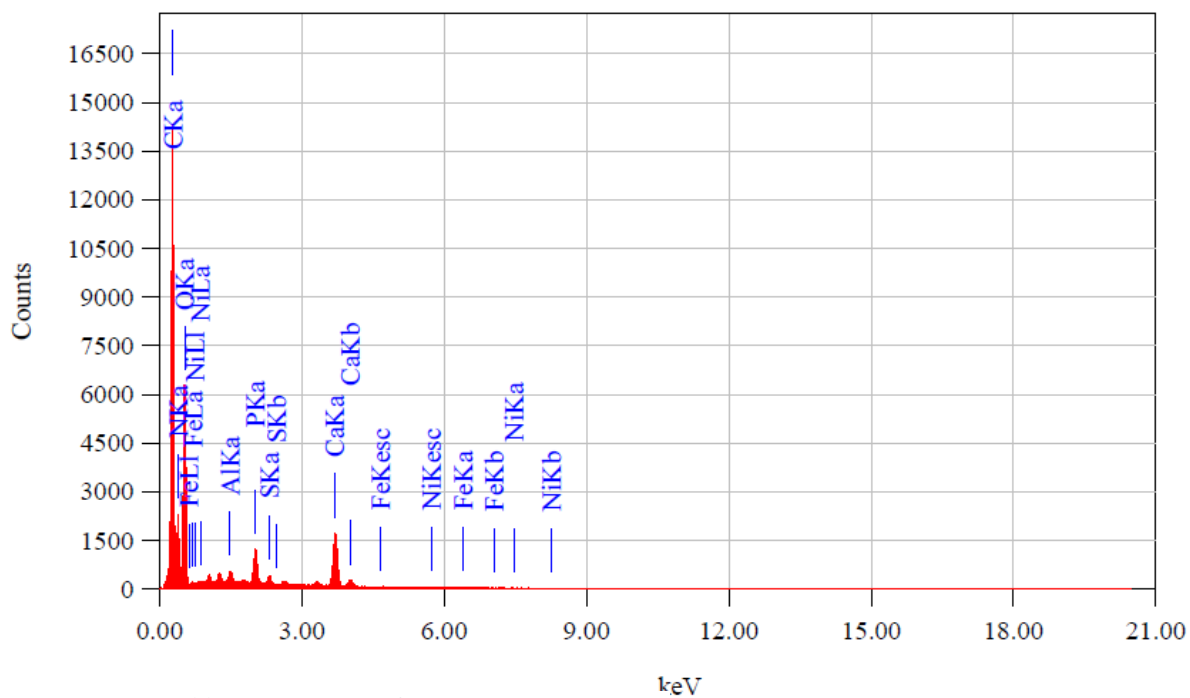
Figure 30: EDX spectrum for WSP
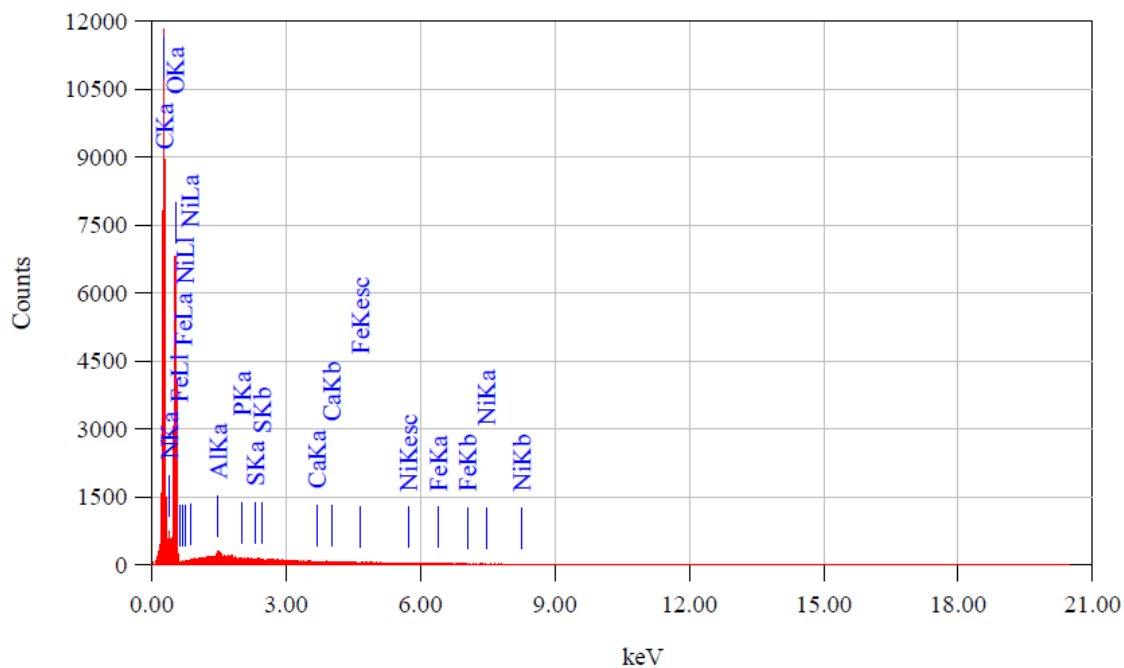
Figure 31: EDX spectrum of CS1

71
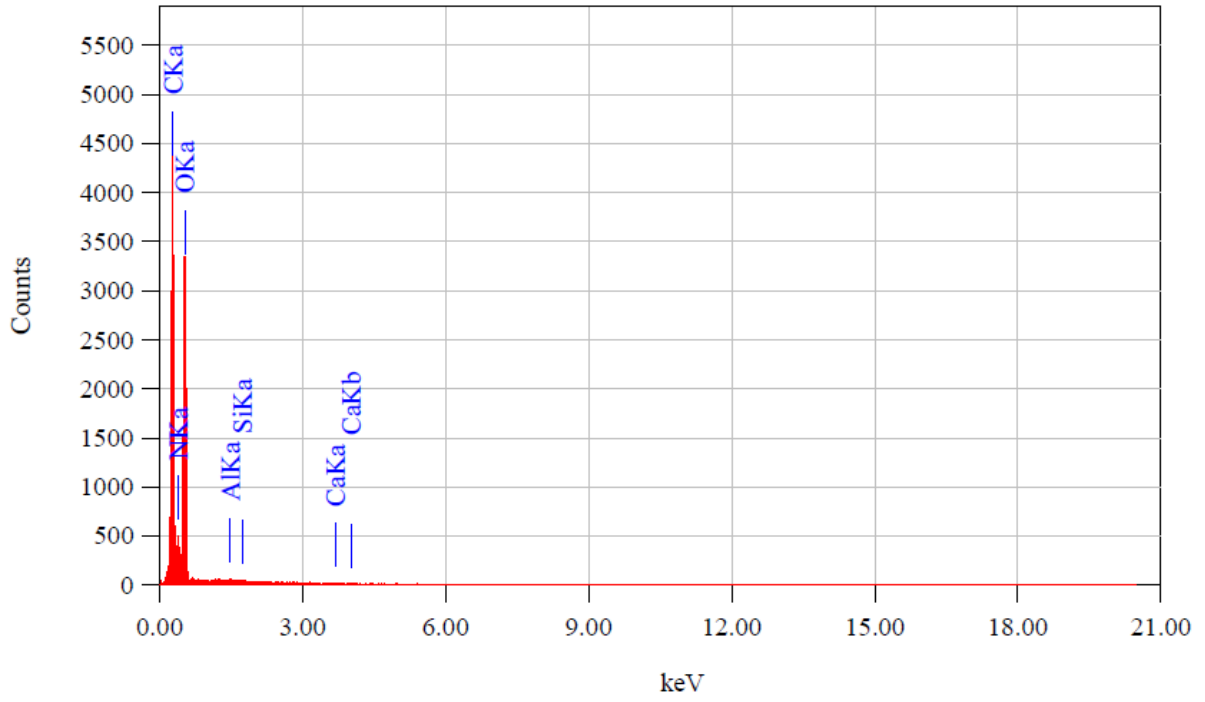
Figure 32: EDX spectrum for CRCS
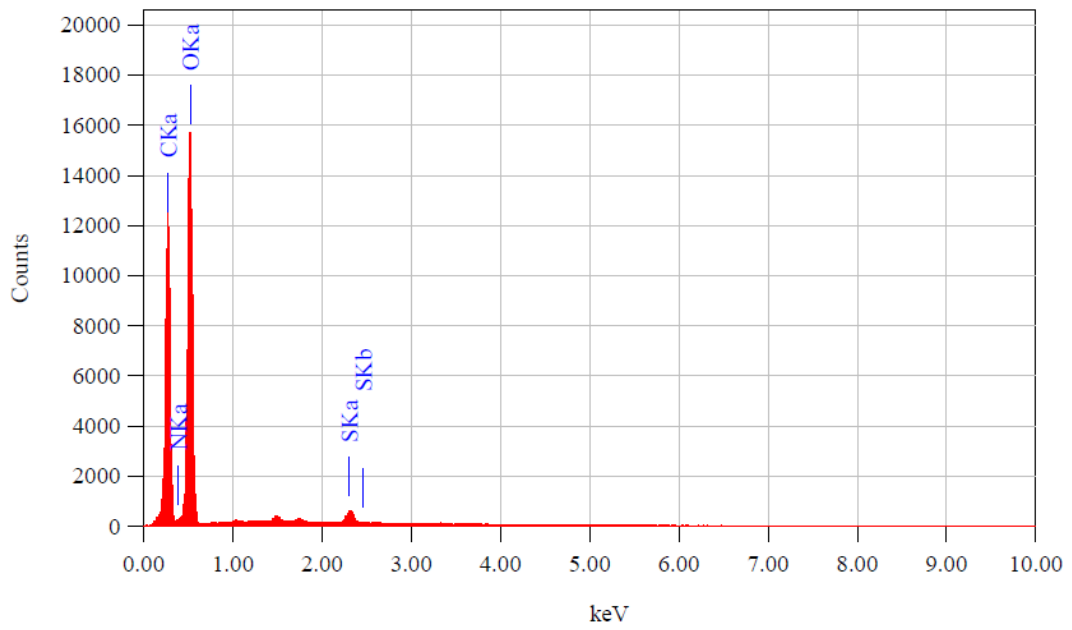
Figure 33: EDX spectrum for SBCNC

72
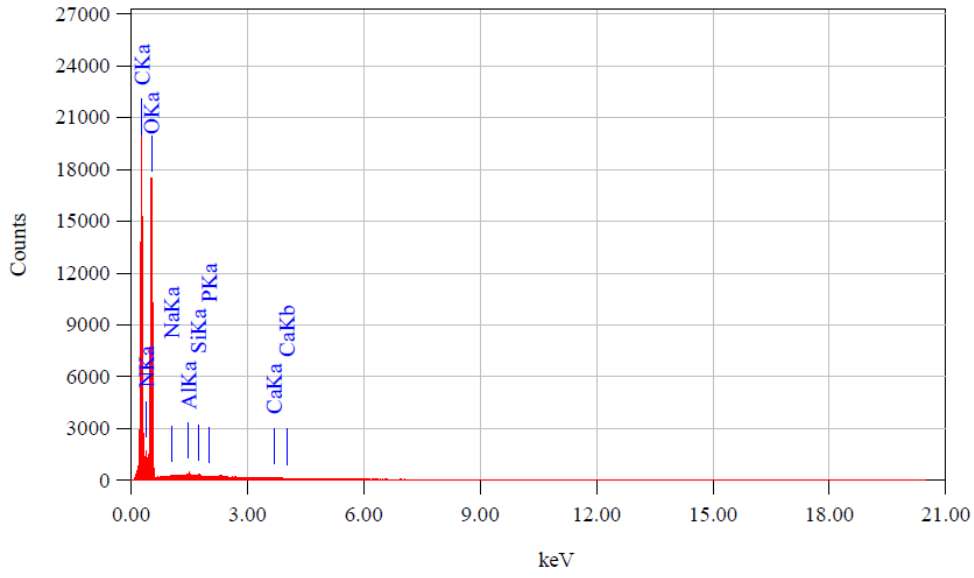
Figure 34: EDX spectrum for CS1/SBCNC
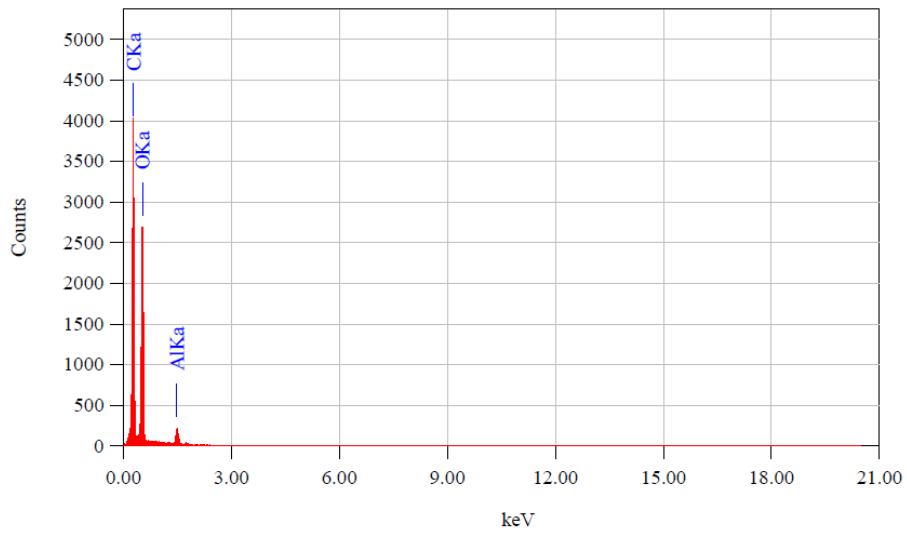
Figure 35: EDX spectrum for SBC
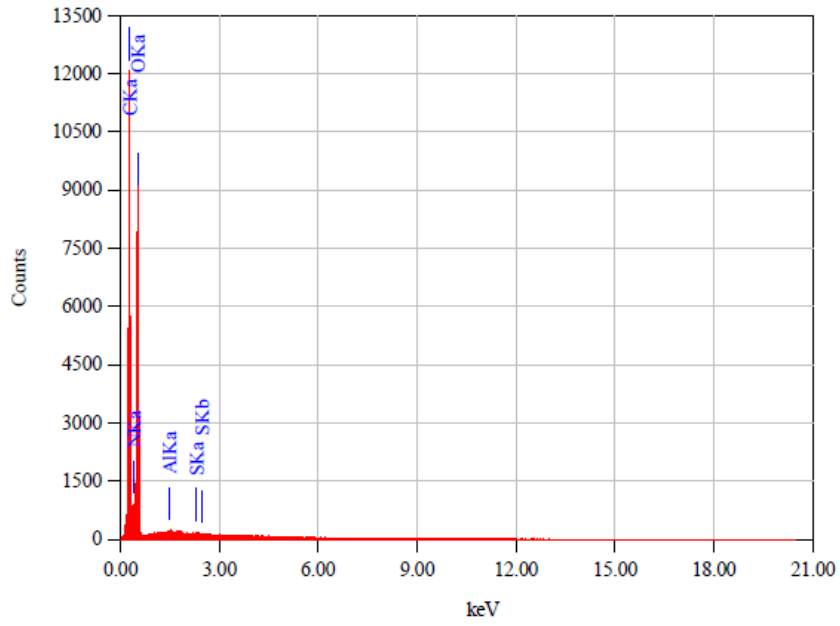
Figure 36: EDX spectrum for CRCS-SBCNC
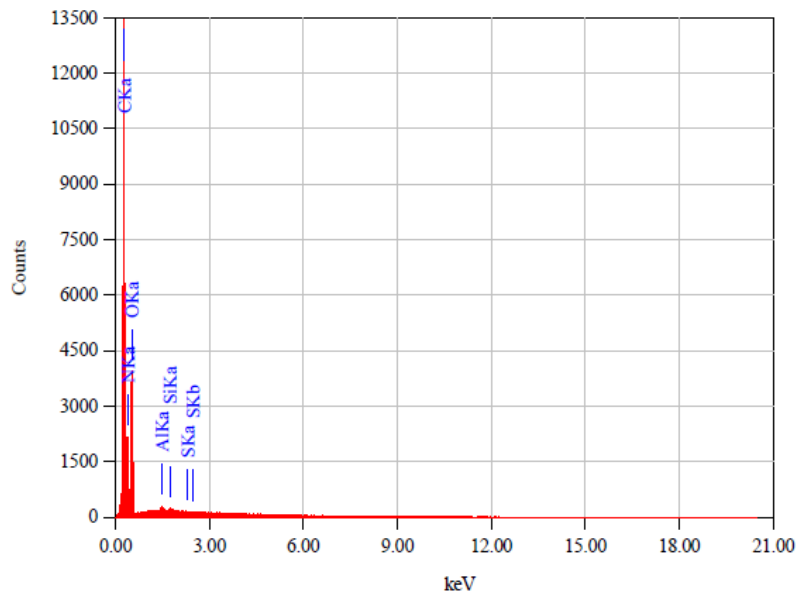
Figure 37: EDX spectrum for MCS-SBCNC-TEPA
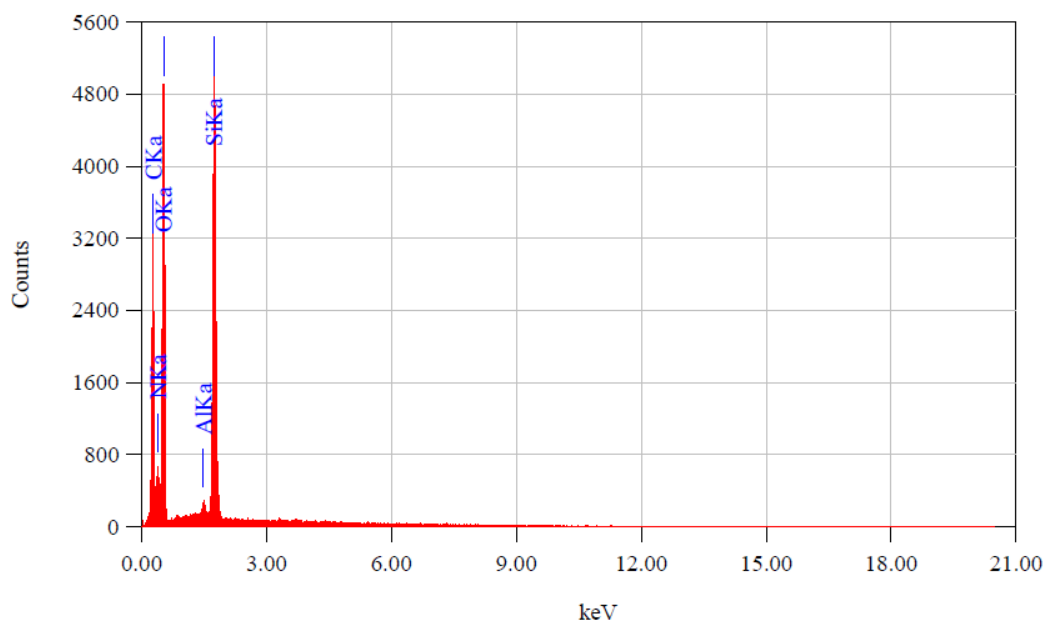
Figure 38: EDX spectrum for CRCS-APTMS
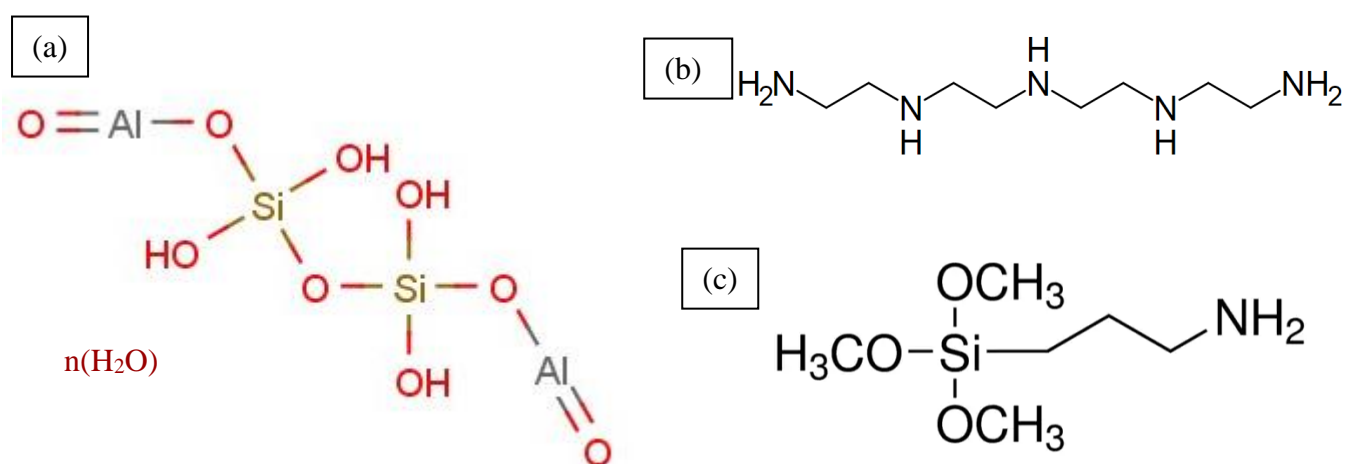
Figure 39: Chemical structure of (a) Halloysite nanoclay hydrate (b) Tetraethelenepentamine (TEPA) (c) 3-Aminopropyltrimethoxysilane (APTMS)

REFERENCES

Ababneh, H., & Hameed, B. H. (2021). Chitosan-Derived Hydrothermally Carbonized Materials and Iis Applications : A Review of Recent Literature. *International Journal of Biological Macromolecules*, *186*, 314–327.

Abdulsalam, J., Mulopo, J., Bada, S. O., & Oboirien, B. (2020). Equilibria and Isosteric Heat of Adsorption of Methane on Activated Carbons Derived from South African Coal Discards. *ACS Omega*. *5*(50), 32530–32539. https://doi.org/10.1021/acsomega.0c04744

Abitbol, T., Rivkin, A., Cao, Y., Nevo, Y., Abraham, E., Ben-Shalom, T., Lapidot, S., & Shoseyov, O. (2016). Nanocellulose, A Tiny Fiber with Huge Applications. *Current opinion in biotechnology*, *39*, 76–88. https://doi.org/10.1016/j.copbio.2016.01.002

Ahmed, S. Ikram, S. (2015). Chitosan & its Derivatives: A Review in Recent Innovations. *Int. J. Pharm. Sci. Re*s, *6*(1), 14

Ahn, S. I., Cho, S., & Choi, N. J. (2021). Effectiveness of Chitosan as a Dietary Supplement in Lowering Cholesterol in Murine Models: A Meta-Analysis. *Marine drugs*, *19*(1), 26. https://doi.org/10.3390/md19010026

Alhwaige, A. A., Agag, T., Ishida, H., & Qutubuddin, S. (2013). Biobased chitosan hybrid aerogels with superior adsorption: Role of graphene oxide in CO_2 capture. *RSC Advances*, *3*(36), 16011–16020. https://doi.org/10.1039/c3ra42022a

Al-Manhel, A. J. Al-Hilphy, A. R. S. Niamah, A. K. (2018). Extraction of Chitosan, Characterisation and Its Use for Water Purification. *J. Saudi Soc. Agric. Sci*., *17*(2), 186−190

Anyanwu, J. T., Wang, Y., & Yang, R. T. (2020). Amine-Grafted Silica Gels for CO_2 Capture including Direct Air Capture. *Industrial and Engineering Chemistry Research*, *59*(15), 7072–7079. https://doi.org/10.1021/acs.iecr.9b05228

Araki, J., Wada, M., Kuga, S. Okano, T. (1999). Influence of Surface Charge on Viscosity Behavior of Cellulose Microcrystal Suspension. *J. Wood Sci,* 45, 258–261 https://doi.org/10.1007/BF01177736

Aranaz, I., Alcántara, A. R., Civera, M. C., Arias, C., Elorza, B., Heras Caballero, A., & Acosta, N. (2021). Chitosan: An Overview of its Properties and Applications. *Polymers*, *13*(19), 3256. https://doi.org/10.3390/polym13193256

Azarabadi, H., & Lackner, K. S. (2020). Postcombustion Capture or Direct Air Capture in Decarbonizing US Natural Gas Power? *Environmental Science & Technology*, *54*(8), 5102–5111. https://doi.org/10.1021/acs.est.0c00161

Bai, R. Yang, M. Hu, G. Xu, L. Hu, X. Li, Z. Wang, S. Dai, W. Fan, M. (2015). A New Nanoporous Nitrogen-Doped Highly-Efficient Carbonaceous CO_2 Sorbent Synthesized With Inexpensive Urea And Petroleum Coke. *Carbon*, 81, 465−473.

Barman, M., Mahmood, S., Augustine, R., Hasan, A., Thomas, S., & Ghosal, K. (2020). Natural Halloysite Nanotubes/Chitosan Based Bio-Nanocomposite for Delivering Norfloxacin, an Anti-Microbial Agent in Sustained Release Manner. *International Journal of Biological Macromolecules*, 162, 1849–1861. https://doi.org/10.1016/j.ijbiomac.2020.08.060

Barzagli, F., Giorgi, C., Mani, F., & Peruzzini, M. (2020). Screening Study of Different Amine-Based Solutions as Sorbents for Direct CO_2 Capture from Air. *ACS Sustainable Chemistry and Engineering*, *8*(37), 14013–14021. https://doi.org/10.1021/acssuschemeng.0c03800

Baxter, A., Dillon, M., Taylor, K. D. A., & Roberts, G. A. F. (1992). Improved method for IR. Determination of the Degree of N-acetylation of Chitosan. *International Journal of Biological Macromolecules*, *14*(16), 6–169.

Beck-Candanedo, S., Roman, M., & Gray, D. G. (2005). Effect of Reaction Conditions on the Properties and Behavior of Wood Cellulose Nanocrystal Suspensions. *Biomacromolecules*, *6*(2), 1048–1054. https://doi.org/10.1021/bm049300p

Bernard F. L., Rodrigues D. M., Polesso B. B., Donato A. J., Seferin, M., Chaban, V. V., Vecchia F. D., Einloft, S. (2016). *Fuel Process. Technol*. 149, 131–138

Bheekhun, N.; Abu Talib, A.R.; Hassan, M.R. (2013). Aerogels in aerospace: An overview. *Adv. Mater. Sci. Eng*. Vol. 2013, no. 2013, 1-18

Bhown, A. S. Freeman, B. C. (2011). Analysis and Status of Post-Combustion Carbon Dioxide Capture Technologies. *Environ. Sci. Technol*., *45*(20), 8624−8632.

Bradić, B., Bajec, D., Pohar, A., Novak, U. & Likozar, B. (2018). A Reaction–Diffusion Kinetic Model For The Heterogeneous N-Deacetylation Step In Chitin Material Conversion To Chitosan In Catalytic Alkaline Solutions. *Reaction Chemistry & Engineering,* 3 920–929. https://doi.org/10.1039/c8re00170g

Cai, H., Zhang, X., Lei, L., & Xiao, C. (2020). Direct CO_2 Capture from Air Via Crystallization with a Trichelating Iminoguanidine Ligand. *ACS Omega*, *5*(32), 20428–20437. https://doi.org/10.1021/acsomega.0c02460

Cheng, J., Li, Y., Hu, L., Liu, J., Zhou, J., & Cen, K. (2018). CO_2 Absorption and Diffusion In Ionic Liquid [P66614][Triz] Modified Molecular Sieves SBA-15 with Various Pore Lengths. *Fuel Processing Technology*, *172*(1), 216–224. https://doi.org/10.1016/j.fuproc.2017.12.022

Choe, J. H., Park, J. R., Chae, Y. S., Kim, D. W., Choi, D. S., Kim, H., Kang, M., Seo, H., Park, Y. K., & Hong, C. S. (2021). Shaping and Silane Coating of a Diamine-Grafted Metal-Organic Framework for Improved CO_2 Capture. *Communications Materials*, *2*(1), 1–8. https://doi.org/10.1038/s43246-020-00109-8

Dassanayake, R.S., Gunathilake, C., Dassanayake, A.C., Abidi, N., & Jaroniec, M. (2017). Amidoxime-Functionalized Nanocrystalline Cellulose–Mesoporous Silica Composites for Carbon Dioxide Sorption at Ambient and Elevated Temperatures. *Journal of Materials Chemistry, 5*, 7462-7473.

Dawson, R. Stockel, E., Holst, J. R., Adams D. J., & Cooper, A. I. (2011). Microporous Organic Polymers for Carbon Dioxide Capture. *Energy Environ. Sci*., 4, 4239−4245.

Delavar, M. Ghoreyshi, A. A. Jahanshahi, M. Khalili, S. Nabian, N. (2012). Equilibria and Kinetics of Natural Gas Adsorption on Multi-Walled Carbon Nanotube Material. *RSC Adv*., *2*, 4490−7

Diab M. A, El-Sonbati A. Z., Bader D. M. D. (2011). Thermal Stability and Degradation of Chitosan Modified by Benzophenone. *Spectrochim Acta Part A Mol Biomol Spectrosc.*, *79*(5):1057–62. doi:10.1016/j.saa.2011.04.019

Domszy, J. G., & Roberts, G. A. F. (1985). Evaluation of Infrared Spectroscopic Techniques for Analyzing Chitosan. *Macromolecular Chemistry and Physics*, *186*(8), 1671–1677.

Dong, X. M., Kimura, T., Revol, J. F., Gray, D. G. (1996). Effects of Ionic Strength on the Isotropic−Chiral Nematic Phase Transition of Suspensions of Cellulose Crystallites**.** *Langmuir,* 12, 2076 – 2082

Dotto, G. L., Vieira, M. L. G., & Pinto, L. A. A. (2012). Kinetics and Mechanism of Tartrazine Adsorption onto Chitin and Chitosan. *Ind. Eng. Chem. Res.*, 51, 19, 6862–6868

Doustdar, F., Olad, A., & Ghorbani, M. (2022a). Effect of Glutaraldehyde and Calcium Chloride as Different Crosslinking Agents on the Characteristics of Chitosan/Cellulose Nanocrystals Scaffold. *International journal of biological macromolecules*, *208*, 912–924. https://doi.org/10.1016/j.ijbiomac.2022.03.193

Doustdar, F., Olad, A., & Ghorbani, M. (2022b). Development of A Novel Reinforced Scaffold Based on Chitosan/Cellulose Nanocrystals/Halloysite Nanotubes for Curcumin Delivery. *Carbohydrate*

polymers, *282*, 119127. https://doi.org/10.1016/j.carbpol.2022.119127

Edgar, C. D., Gray, D. G. (2003). Smooth Model Cellulose I Surfaces from Nanocrystal Suspensions. *Cellulose 10*, 299–306. https://doi.org/10.1023/A:1027333928715

El Knidri, H., Belaabed, R., Addaou, A., Laajeb, A., & Lahsini, A. (2018). Extraction, Chemical Modification and Characterization of Chitin and Chitosan. *International journal of biological macromolecules*, *120*(Pt A), 1181–1189. https://doi.org/10.1016/j.ijbiomac.2018.08.139

Elazzouzi-Hafraoui, S., Nishiyama, Y., Putaux, J. L., Heux, L., Dubreuil, F., & Rochas, C. (2008). The Shape and Size Distribution of Crystalline Nanoparticles Prepared by Acid Hydrolysis of Native Cellulose. *Biomacromolecules*, *9*(1), 57–65. https://doi.org/10.1021/bm700769p

Esmaeili, Z., Izadyar, S., Hamzeh, Y., & Abdulkhani, A. (2021). Preparation and Characterization of Highly Porous Cellulose Nanofibrils/Chitosan Aerogel for Acid Blue 93 Adsorption: Kinetics, Isotherms, and Thermodynamics Analysis. *Journal of Chemical and Engineering Data*, *66*(2), 1068–1080. https://doi.org/10.1021/acs.jced.0c00872

Esmaeili, Z., Izadyar, S., Hamzeh, Y., & Abdulkhani, A. (2021). Preparation and Characterization of Highly Porous Cellulose Nanofibrils/Chitosan Aerogel for Acid Blue 93 Adsorption: Kinetics, Isotherms, and Thermodynamics Analysis. *Journal of Chemical and Engineering Data*, *66*(2), 1068–1080. https://doi.org/10.1021/acs.jced.0c00872

Fern, A., Reyes, G., Oviedo, C., Gacit, W., & Uyarte, O. (2018). Isolation and Characterization of Cellulose Nanocrystals from Rejected Fibers Originated in the Kraft Pulping Process. *Polymers*, *10*(1145), 1–11. https://doi.org/10.3390/polym10101145

Fredriksen, S. B. Jens, K. J. (2013). Oxidative Degradation of Aqueous Amine Solutions of MEA, AMP, MDEA, Pz: A Review. *Energy Procedia*, 37, 1770−1777.

French, A. D., Perez, S., Bulone, V., Rosenau, T., Gray, D. (2018). Cellulose. Encyclopedia of Polymer Science and Technology. John Wiley & Sons, Inc.: Hoboken, NJ, 1−69. https://doi.org/10.1002/0471440264.pst042.pub2

Friedlingstein, P., O'Sullivan, M., Jones, M. W., Andrew, R. M., Hauck, J., Olsen, A., Peters, G. P., Peters, W., Pongratz, J., Sitch, S., Le Quéré, C., Canadell, J. G., Ciais, P., Jackson, R. B., Alin, S., Aragão, L. E. O. C., Arneth, A., Arora, V., Bates, N. R., Zaehle, S. (2020). Global Carbon Budget 2020. *Earth System Science Data*, *12*(4), 3269–3340. https://doi.org/10.5194/essd-12-3269-2020

Fujiki, J., & Yogo, K. (2014). Carbon Dioxide Adsorption onto Polyethylenimine-Functionalized Porous Chitosan Beads. *Energy and Fuels*, *28*(10), 6467–6474. https://doi.org/10.1021/ef500975g

George, J., & Sabapathi, S. N. (2015). Cellulose Nanocrystals: Synthesis, Functional Properties, and

Applications. *Nanotechnology, science and applications*, *8*, 45–54. https://doi.org/10.2147/NSA.S64386

Golmohammadi, H.; Morales-Narváez, E.; Naghdi, T.; Merkoçi, A. (2017). Nanocellulose In Sensing and Biosensing. *Chem. Mater.*, *29*(13), 5426−5446.

Grząbka-Zasadzińska, A., Amietszajew, T., & Borysiak, S. (2017). Thermal and mechanical properties of chitosan nanocomposites with cellulose modified in ionic liquids. Journal of Thermal Analysis and Calorimetry, 130(1), 143-154. https://doi.org/10.1007/s10973-017-6295-3

Guo, L.; Hu, X.; Hu, G.; Chen, J.; Li, Z.; Dai, W.; Dacosta, H. F. M.; Fan, M. (2015). Tetraethylenepentamine Modified Protonated Titanate Nanotubes for CO_2 Capture. *Fuel Process. Technol*, 138, 663−669

Guo, M., Liang, S., Liu, J., Jin, J., & Mi, J. (2020). Epoxide-Functionalization of Grafted Tetraethylenepentamine on the Framework of an Acrylate Copolymer as a CO_2 Sorbent with Long Cycle Stability. *ACS Sustainable Chemistry and Engineering*, *8*(9), 3853–3864. https://doi.org/10.1021/acssuschemeng.9b07318

Guo, Y., Luo, L., Zheng, Y., & Zhu, T. (2020). Optimization of CO_2 Adsorption on Solid-Supported Amines and Thermal Regeneration Mode Comparison. *ACS Omega*, *5*(17), 9641–9648. https://doi.org/10.1021/acsomega.9b03374

Habibi, Y. (2014). Key Advances in the Chemical Modification of Nanocelluloses. *Chem. Soc. Rev*., *43*(5), 1519−1542

Habibi, Y.; Lucia, L. A.; Rojas, O. J. (2010). Cellulose Nanocrystals: Chemistry, Self-assembly, and Applications. *Chem. Rev*., *110*(6), 3479−3500.

Hajji, S., Younes, I., Ghorbel-Bellaaj, O., Hajji, R., Rinaudo, M., Nasri, M., & Jellouli, K. (2014). Structural Differences Between Chitin and Chitosan Extracted from Three Different Marine Sources. *International journal of biological macromolecules*, *65*, 298–306. https://doi.org/10.1016/j.ijbiomac.2014.01.045

He, G., Huang, S., Villalobos, L. F., Zhao, J., Mensi, M., Oveisi, E., Rezaei, M., & Agrawal, K. V. (2019). High-permeance polymer-functionalized single-layer graphene membranes that surpass the postcombustion carbon capture target. Energy and Environmental Science, 12(11), 3305–3312. https://doi.org/10.1039/c9ee01238a

Herzog, H. J. (2018). *Carbon Capture*. The MIT Press.

Hou, C., Wu, Y., Wang, T., Wang, X., & Gao, X. (2019). Preparation of Quaternized Bamboo Cellulose and Its Implication in Direct Air Capture of CO_2. *Energy and Fuels*, *33*(3), 1745–1752.

https://doi.org/10.1021/acs.energyfuels.8b02821

Hsan, N., Dutta, P. K., Kumar, S., Bera, R., & Das, N. (2019). Chitosan Grafted Graphene Oxide Aerogel: Synthesis, Characterization and Carbon Dioxide Capture Study. *International Journal of Biological Macromolecules*, *125*, 300–306. https://doi.org/10.1016/j.ijbiomac.2018.12.071

Huang, T., Shao, Y., Zhang, Q., Deng, Y., Liang, Z., Guo, F., Li, P., & Wang, Y. (2019). Chitosan-Cross-Linked Graphene Oxide/Carboxymethyl Cellulose Aerogel Globules with High Structure Stability in Liquid and Extremely High Adsorption Ability. *ACS Sus. Chem. Eng.* https://doi.org/10.1021/acssuschemeng.9b00691

Hussein, M. H. M., El-Hady, M. F., Shehata, H. A. H., Hegazy, M. A., & Hefni, H. H. H. (2013). Preparation of Some Eco-Friendly Corrosion Inhibitors Having Antibacterial Activity From Sea Food Waste. *Journal of Surfactants and Detergents*, *16*(2), 233–242. https://doi.org/10.1007/s11743-012-1395-3

Hwang, K. T., Jung, S. T., Lee, G. D., Chinnan, M. S., Park, Y. S., & Park, H. J. (2002). Controlling Molecular Weight and Degree Of Deacetylation of Chitosan by Response Surface Methodology. *Journal of agricultural and food chemistry*, *50*(7), 1876–1882. https://doi.org/10.1021/jf011167u]

Hwang, K. T., Jung, S. T., Lee, G. D., Chinnan, M. S., Park, Y. S., & Park, H. J. (2002). Controlling Molecular Weight and Degree of Deacetylation of Chitosan by Response Surface Methodology. *Journal of agricultural and food chemistry*, *50*(7), 1876–1882. https://doi.org/10.1021/jf011167u

Ilyina, A. V., Tikhonov V. E., Albulov A. I., Varlamov V. P. (2000). Enzymic Preparation of Acid-Free-Water-Soluble Chitosan. *Process. Biochem*. *35*(6), 563-568

IPCC. (2006). The IPCC Special Report on Carbon Dioxide Capture and Storage. In *ECOS 2006 - Proceedings of the 19th International Conference on Efficiency, Cost, Optimization, Simulation and Environmental Impact of Energy Systems*.

IPCC. Summary for Policymakers. (2013). In *Climate Change: The Physical Science Basis*; Contribution of Working Group I to the Fifth Assessment Report of the Intergovernmental Panel on Climate Change; Stocker, T.F., Qin, D., Plattner, G.-K., Tignor, M., Allen, S.K., Boschung, J., Nauels, A., Xia, Y., Bex, V., Midgley, P.M., Eds.; Cambridge University Press: Cambridge, UK; New York, NY, USA, 2013; Volume 3, pp. 3–29.

Ishihara, M., Ono, K., Sato, M., Nakanishi, K., Saito, Y., Yura, H., Matsui, T., Hattori, H., Fujita, M., Kikuchi, M., & Kurita, A. (2001). Acceleration of Wound Contraction And Healing With a Photocrosslinkable Chitosan Hydrogel. *Wound repair and regeneration : official publication of*

the Wound Healing Society [and] the European Tissue Repair Society, 9(6), 513–521. https://doi.org/10.1046/j.1524-475x.2001.00513.x]

Jayakumar, R., Menon, D. Manzoor, K,. Nair S. V., & Tamura, H. (2010b). Biomedical Applications of Chitin Nanomaterials: A Short Review. *Carbohydrate Polymers.* 82(2), 227-232. doi:10.1016/j.carbpol.2010.04.074

Jayakumar, R., Prabaharan, M., Nair, S. V., & Tamura, H. (2010a). Novel Chitin and Chitosan Nanofibers in Biomedical Applications. *Biotechnology advances*, 28(1), 142–150. https://doi.org/10.1016/j.biotechadv.2009.11.001,7

Jiang, Y., Mathias, P. M., Freeman, C. J., Swisher, J. A., Zheng, R. F., Whyatt, G. A., & Heldebrant, D. J. (2021). Techno-Economic Comparison of Various Process Configurations for Post-Combustion Carbon Capture Using a Single-Component Water-Lean Solvent. *International Journal of Greenhouse Gas Control*, 106(1), 103279. https://doi.org/10.1016/j.ijggc.2021.103279

Kang, H., Liu, X., Zhang, S., & Li, J. (2017). Functionalization Of Halloysite Nanotubes (Hnts) *Via* Mussel-Inspired Surface Modification And Silane Grafting For HNTs/Soy Protein Isolate Nanocomposite Film Preparation. *RSC Advances*, *7*, 24140–24148. https://doi.org/10.1039/C7RA02987J

Kar, S., Goeppert, A., Galvan, V., Chowdhury, R., Olah, J., & Prakash, G. K. S. (2018). A Carbon-Neutral CO_2 Capture, Conversion, and Utilization Cycle with Low-Temperature Regeneration of Sodium Hydroxide. *Journal of the American Chemical Society*, *140*(49), 16873–16876. https://doi.org/10.1021/jacs.8b09325

Kasaai M. R. (2009). Various Methods for Determination of the Degree of N-Acetylation of Chitin and Chitosan: A Review. *Journal of agricultural and food chemistry*, *57*(5), 1667–1676. https://doi.org/10.1021/jf803001m

Kasaai, M. R., & Arul, J. (2000). Intrinsic Viscosity – Molecular Weight Relationship for Chitosan. 38(19), *J. Polym. Sci. B: Polym. Phys*. 2591–2598.

Keith, D. W., Holmes, G., St. Angelo, D., & Heidel, K. (2018). A Process for Capturing CO_2 from the Atmosphere. *Joule*, *2*(8), 1573–1594. https://doi.org/10.1016/j.joule.2018.05.006

Khan, A., Wen, Y., Huq, T., & Ni, Y. (2018). Cellulosic Nanomaterials in Food and Nutraceutical Applications: A Review. *Journal of agricultural and food chemistry*, *66*(1), 8–19. https://doi.org/10.1021/acs.jafc.7b04204

Klein, M. P., Hackenhaar, C. R., Lorenzoni, A. S. G., Rodrigues, R. C., Costa, T. M. H., Ninow, J. L., Hertz, P. F. (2016). Chitosan Crosslinked with Genipin As Support Matrix For Application In Food Process: Support Characterization and B-D Galactosidase Immobilization. *Carbohydr. Polym*., 137, 184−190.

Klemm, D. Heublein, B. Fink, H. P. Bohn, A. (2005). Cellulose: Fascinating Biopolymer and Sustainable Raw Material. *Angew. Chem., Int. Ed.*, *44*(22), 3358−3393.

Klemm, D., Kramer, F., Moritz, S., Lindström, T., Ankerfors, M., Gray, D., & Dorris, A. (2011). Nanocelluloses: A New Family of Nature-Based Materials. In *Angewandte Chemie - International Edition, 50*(24), 5438–5466. https://doi.org/10.1002/anie.201001273

Kolle, J. M., & Sayari, A. (2020). Covalently Immobilized Polyethylenimine for CO_2 Adsorption. *Industrial and Engineering Chemistry Research*, *59*(15), 6944–6950. https://doi.org/10.1021/acs.iecr.9b04669

Kumar, S., Bera, R., Das, N., & Koh, J. (2020). Chitosan-Based Zeolite-Y and ZSM-5 Porous Biocomposites for H_2 And CO_2 Storage. *Carbohydrate Polymers*, 232, 115808. https://doi.org/10.1016/j.carbpol.2019.115808

Kumar, S., de A. e Silva, J., Wani, M. Y., Gil, J. M., & Sobral, A. J. F. N. (2017). Carbon Dioxide Capture and Conversion by an Environmentally-friendly Chitosan Based Meso-Tetrakis(4-Sulfonatophenyl) Porphyrin. *Carbohydrate Polymers*, *175*, 575–583. https://doi.org/10.1016/j.carbpol.2017.08.031

Kumar, S., Prasad, K., Gil, J. M., Sobral, A. J. F. N., & Koh, J. (2018). Mesoporous Zeolite-Chitosan Composite for Enhanced Capture And Catalytic Activity in Chemical Fixation of CO_2. *Carbohydrate Polymers*, 198, 401–406. https://doi.org/10.1016/j.carbpol.2018.06.100

Kumari, Suneeta and Rupak, K. (2020). Handbook of Chitin And Chitosan Preparation And Properties (Vol. 1). Elsevier Inc.

Lawrie, G., Keen, I., Drew, B., Chandler-temple, A., Rintoul, L., Fredericks, P., & Grøndahl, L. (2007). Interactions between Alginate and Chitosan Biopolymers Characterized Using FTIR and XPS. *8*(8), 2533–2541. https://doi.org/10.1021/bm070014y

Li, F., You, X., Li, Q., Qin, D., Wang, M., Yuan, S., Chen, X., & Bi, S. (2021). Homogeneous Deacetylation and Degradation of Chitin In NaOH/Urea Dissolution System. *International journal of biological macromolecules*, *189*, 391–397. https://doi.org/10.1016/j.ijbiomac.2021.08.126

Li, J., Zhang, W., & Bao, A. (2021). Design of Hierarchically Structured Porous Boron/Nitrogen-Codoped Carbon Materials with Excellent Performance for CO_2 Capture. *Industrial & Engineering Chemistry Research*. https://doi.org/10.1021/acs.iecr.0c05725

Li, Yannan, Cheng, J., Hu, L., Liu, J., Zhou, J., & Cen, K. (2018). Graphene Nanoplatelet and Reduced Graphene Oxide Functionalized by Ionic Liquid for CO_2 Capture. *Energy and Fuels, 32*(6), 6918–6925. https://doi.org/10.1021/acs.energyfuels.8b00889

Li, Yu, Gao, J., Li, J., Li, Y., Bernards, M. T., Tao, M., He, Y., & Shi, Y. (2020). Screening and Performance Evaluation of Triethylenetetramine Nonaqueous Solutions for CO_2 Capture with Microwave Regeneration. *Energy and Fuels*, *34*(9), 11270–11281. https://doi.org/10.1021/acs.energyfuels.0c02006

Liu, H., Liu, B., Lin, L. C., Chen, G., Wu, Y., Wang, J., Gao, X., Lv, Y., Pan, Y., Zhang, X., Zhang, X., Yang, L., Sun, C., Smit, B., & Wang, W. (2014). A Hybrid Absorption-Adsorption Method to Efficiently Capture Carbon. *Nature Communications*, *5*, 1–7. https://doi.org/10.1038/ncomms6147

Liu, Q., Yu, H., Zeng, F., Li, X., Sun, J., Li, C., Lin, H., & Su, Z. (2021). HKUST-1 Modified Ultrastability Cellulose /Chitosan Composite Aerogel for Highly Efficient Removal of Methylene Blue. *Carbohydrate Polymers*, *255*, 117402. https://doi.org/10.1016/j.carbpol.2020.117402

Long, L. Y., Weng, Y. X., & Wang, Y. Z. (2018). Cellulose Aerogels: Synthesis, Applications, and Prospects. *Polymers*, *10*(6), 623. https://doi.org/10.3390/polym10060623

Lu, L., Guest, J. S., Peters, C. A., Zhu, X., Rau, G. H., & Ren, Z. J. (2018). Wastewater Treatment for Carbon Capture and Utilization. *Nature Sustainability*, *1*(12), 750–758. https://doi.org/10.1038/s41893-018-0187-9

Lu, S., Yuan, G., Zhu, Y., & Yu, S. (2021). Carbon Dots Crosslinked Chitosan/Cellulose Sponge Capture of Methyl Blue by an Adsorption Process. *Luminescence: the journal of biological and chemical luminescence*, *36*(6), 1459–1468. https://doi.org/10.1002/bio.4089

Maleki, H. (2016). Recent Advances in Aerogels for Environmental Remediation Applications: A Review. *Chem. Eng. J.*, *300*, 98–118

Mandal, A.; Chakrabarty, D. (2014). Studies on the Mechanical, Thermal, Morphological and Barrier Properties of Nanocomposites Based on Poly(vinyl alcohol) and Nanocellulose From Sugarcane Bagasse. *J. Ind. Eng. Chem.*, *20*, 462−473.

Meng, G., Peng, H., Wu, J., Wang, Y., Wang, H., Liu, Z., & Guo, X. (2017). *Fabrication of*

Superhydrophobic Cellulose/Chitosan Composite Aerogel for Oil / Water Separation. *18*(4), 706–712. https://doi.org/10.1007/s12221-017-1099-4

Miao, Y., Luo, H., Pudukudy, M., Zhi, Y., Zhao, W., Shan, S., Jia, Q., & Ni, Y. (2020). CO_2 Capture Performance and Characterization of Cellulose Aerogels Synthesized from Old Corrugated Containers. *Carbohydrate Polymers*, *227*, 115380. https://doi.org/10.1016/j.carbpol.2019.115380

Mohammed, M. A., Syeda, J., Wasan, K. M., & Wasan, E. K. (2017). An Overview of Chitosan Nanoparticles and Its Application in Non-Parenteral Drug Delivery. *Pharmaceutics*, *9*(4), 53. https://doi.org/10.3390/pharmaceutics9040053.

Nazir, G., Rehman, A., & Park, S. J. (2021). Valorization of shrimp shell biowaste for environmental remediation: Efficient contender for CO_2 adsorption and separation. *Journal of environmental management*, *299*, 113661. https://doi.org/10.1016/j.jenvman.2021.113661

Nguyen, S. T., Feng, J., Le, N. T., Le, A. T. T., Hoang, N., Tan, V. B. C., & Duong, H. M. (2013). Cellulose Aerogel from Paper Waste for Crude Oil Spill Cleaning. *52*(51) 18386–18391). https://doi.org/10.1021/ie4032567

No, H. K., Lee, S. H., Park, N. Y., & Meyers, S. P. (2003). Comparison of Physicochemical, Binding, And Antibacterial Properties of Chitosans Prepared Without and With Deproteinization Process. *Journal of agricultural and food chemistry*, *51*(26), 7659–7663. https://doi.org/10.1021/jf030226w

Nordqvist D., Idermark J, Hedenqvist M. S., Ga¨llstedt M., Ankerfors M., Lindstro¨m T. (2007). Enhancement of the Wet Properties of Transparent Chitosan—Acetic-Acid—Salt Films Using Microfibrillated Cellulose. *Biomacromolecules.* *8*(8):2398–403. doi:10.1021/bm070246x

Ogawa, K., Yui, T., & Okuyama, K. (2004). Three-D Structures of Chitosan. *International journal of biological macromolecules*, *34*(1-2), 1–8. https://doi.org/10.1016/j.ijbiomac.2003.11.002

Pachauri, R. K.; Allen, M. R.; Barros, V. R.; Broome, J.; Cramer, W.; Christ, R.; Church, J. A.; Clarke, L.; Dahe, Q.; Dasgupta, P. Climate Change. (2014). Synthesis Report. Contribution of Working Groups I, II and III to the Fifth Assessment Report of the Intergovernmental Panel on Climate Change; IPCC, 2014

Park, J., Park, J. R., Choe, J. H., Kim, S., Kang, M., Kang, D. W., Kim, J. Y., Jeong, Y. W., & Hong, C. S. (2020). Metal-Organic Framework Adsorbent for Practical Capture of Trace Carbon Dioxide. *ACS Applied Materials and Interfaces*, *12*(45), 50534–50540. https://doi.org/10.1021/acsami.0c16224

Park, R. D., Jo, K. J., Jo, Y. Y., Jin, Y. L., Kim, K. Y., Shim, J. H., Kim, Y. W. (2002). *Journal of*

Microbiology and Biotechnology. 12, 84 – 88

Pierre, A. C.; Pajonk, G. M. (2002). Chemistry of Aerogels and Their Applications. *Chem. Rev.*, 102, 4243−4266

Primo, A., Forneli, A., Corma, A., & García, H. (2012). Graphitisation of Chitosan and Alginate Biopolymers: From Biomass Wastes to Highly Efficient CO_2 Adsorbents. *ChemSusChem*, *5*(11), 2207–2214. https://doi.org/10.1002/cssc.201200366

Qaroush, A. K., Assaf, K. I., Bardaweel, S. K., Al-Khateeb, A., Alsoubani, F., Al-Ramahi, E., Masri, M., Brück, T., Troll, C., Rieger, B., & Eftaiha, A. F. (2017). Chemisorption Of CO_2 by Chitosan Oligosaccharide/DMSO: Organic Carbamato-Carbonato Bond Formation. *Green Chemistry*, *19*(18), 4305–4314. https://doi.org/10.1039/c7gc01830d

Qazvini, O. T., Babarao, R., & Telfer, S. G. (2021). Selective Capture of Carbon Dioxide From Hydrocarbons Using A Metal-Organic Framework. *Nature Communications*, *12*(1), 1–8. https://doi.org/10.1038/s41467-020-20489-2

Qian, X., Yang, J., Fei, Z., Liu, Q., Zhang, Z., Chen, X., Tang, J., Cui, M., & Qiao, X. (2019). A Simple Strategy to Improve PEI Dispersion on MCM-48 with Long-Alkyl Chains Template for Efficient CO_2 Adsorption. *Industrial and Engineering Chemistry Research.* https://doi.org/10.1021/acs.iecr.9b00545

Qin, C., Du, Y., Xiao, L., Li, Z., & Gao, X. (2002). Enzymic Preparation Of Water-Soluble Chitosan and Their Antitumor Activity. *International journal of biological macromolecules*, *31*(1-3), 111–117. https://doi.org/10.1016/s0141-8130(02)00064-8)

Riofrio, A., Alcivar, T., & Baykara, H. (2021). Environmental and Economic Viability of Chitosan Production in Guayas-Ecuador: A Robust Investment and Life Cycle Analysis. *ACS omega*, *6*(36), 23038–23051. https://doi.org/10.1021/acsomega.1c01672

Rizal, S.; Yahya, E.B.; Abdul Khalil, H.P.S.; Abdullah, C.K.; Marwan, M.; Ikramullah, I.; Muksin, U. (2021). Preparation and Characterization of Nanocellulose/Chitosan Aerogel Scaffolds Using Chemical-Free Approach. *Gels*, *7*, 246. https://doi.org/10.3390/gels7040246

Rochelle, G. T. (2009). Amine Scrubbing for CO_2 Capture. *Science*, *325*(5948), 1652−1654.

Rosu, C., Pang, S. H., Sujan, A. R., Sakwa-Novak, M. A., Ping, E. W., & Jones, C. W. (2020). Effect of Extended Aging and Oxidation on Linear Poly(propylenimine)-Mesoporous Silica Composites for CO_2 Capture from Simulated Air and Flue Gas Streams. *ACS Applied Materials and Interfaces, 12*(34), 38085–38097. https://doi.org/10.1021/acsami.0c09554

Roy, J. C., Salaün, F., Giraud, S., & Ferri, A. (2017). Solubility of Chitin : Solvents , Solution Behaviors

and Their Related Mechanisms. https://doi.org/10.5772/intechopen.71385

Ruiz, C., Rincón, L., Contreras, R. R., Sidney, C., & Almarza, J. (2020). Sustainable and Negative Carbon Footprint Solid-Based NaOH Technology for CO_2 Capture. *ACS Sustainable Chemistry and Engineering*, *8*(51), 19003–19012. https://doi.org/10.1021/acssuschemeng.0c07093

Rungthaworn, P., Sukatta, U., & Sukyai, P. (2020). Pretreatment of Cellulose from Sugarcane Bagasse with Xylanase for Improving Dyeability with Natural Dyes. https://doi.org/10.1021/acsomega.0c03837

Rungthaworn, P., Sukatta, U., & Sukyai, P. (2020). Pretreatment of Cellulose from Sugarcane Bagasse with Xylanase for Improving Dyeability with Natural Dyes. *ACS Omega*, *5*, 28168−28177. https://doi.org/10.1021/acsomega.0c03837

Sabnis, S., & Block, L. H. (1997). Improved Infrared Spectroscopic Method for the Analysis of Degree of N-Deacetylation. *Polymer Bulletin*, 39, 67–71.

Sarkar, G.; Orasugh, J. T.; Saha, N. R.; Roy, I.; Bhattacharyya, A.; Chattopadhyay, A. K.; Rana, D.; Chattopadhyay, D. (2017). Cellulose Nanofibrils/Chitosan Based Transdermal Drug Delivery Vehicle for Controlled Release of Ketorolac Tromethamine. *New J. Chem*., 41, 15312−15319

Sato, K., & Hunger, M. (2020). Carbon dioxide adsorption in open nanospaces formed by overlap of saponite clay nanosheets. *Communications Chemistry*, *3*(1), 1–7. https://doi.org/10.1038/s42004-020-00346-5

Sato, K., & Hunger, M. (2020). Carbon Dioxide Adsorption in Open Nanospaces Formed by Overlap of Saponite Clay Nanosheets. *Communications Chemistry*, *3*(1), 1–7. https://doi.org/10.1038/s42004-020-00346-5

Scripps Institution of Oceanography (SIO). (2022). The Keeling Curve. Available online: https://keelingcurve.ucsd.edu/ (Accessed on 5 May, 2022)

Seantier, B. Bendahou, D.; Bendahou, A. Grohens, Y. Kaddami, H. (2016). Multi-Scale Cellulose Based New Bio-Aerogel Composites with Thermal Super-Insulating and Tunable Mechanical Properties. *Carbohydr. Polym*., 138, 335–348

Sen, R., Goeppert, A., Kar, S., & Prakash, G. K. S. (2020). Hydroxide Based Integrated CO_2 Capture from Air and Conversion to Methanol. *Journal of the American Chemical Society, 142*(10), 4544–4549. https://doi.org/10.1021/jacs.9b12711

Sepahvand, S., Jonoobi, M., Ashori, A., Gauvin, F., Brouwers, H. J. H., Oksman, K., & Yu, Q. (2020). A Promising Process to Modify Cellulose Nanofibers for Carbon Dioxide (CO_2) Adsorption.

Carbohydrate Polymers, *230*, 115571. https://doi.org/10.1016/j.carbpol.2019.115571

Shak, K., Pang, Y. L., & Mah, S. K. (2018). Nanocellulose: Recent Advances and its Prospects in Environmental Remediation. *Beilstein journal of nanotechnology*, *9*, 2479–2498. https://doi.org/10.3762/bjnano.9.232

Shu, Q., Legrand, L., Kuntke, P., Tedesco, M., & Hamelers, H. V. M. (2020). Electrochemical Regeneration of Spent Alkaline Absorbent from Direct Air Capture. *Environmental science & technology*, *54*(14), 8990–8998. https://doi.org/10.1021/acs.est.0c01977

Siegelman, R. L., Milner, P. J., Forse, A. C., Lee, J. H., Colwell, K. A., Neaton, J. B., Reimer, J. A., Weston, S. C., & Long, J. R. (2019). Water Enables Efficient CO_2 Capture from Natural Gas Flue Emissions in an Oxidation-Resistant Diamine-Appended Metal-Organic Framework. *Journal of the American Chemical Society*, *141*(33), 13171–13186. https://doi.org/10.1021/jacs.9b05567

Sogias, I.A., Khutoryanskiy, V.V., & Williams, A.C. (2010). Exploring the Factors Affecting the Solubility of Chitosan in Water. *Macromolecular Chemistry and Physics, 211*, 426-433

Soni, B., Barbary, E., & Mahmoud, B. (2015). Chemical Isolation And Characterization of Different Cellulose Nanofibers from Cotton Stalks. *Carbohydrate Polymers*, *134*, 581–589. https://doi.org/10.1016/j.carbpol.2015.08.031

Stergar, J.; Maver, U. (2016). Review Of Aerogel-Based Materials in Biomedical Applications. *J. Sol-Gel Sci. Technol.*, 77, 738–752

Sujan, A. R., Kumar, D. R., Sakwa-Novak, M., Ping, E. W., Hu, B., Park, S. J., & Jones, C. W. (2019). Poly(glycidyl amine)-Loaded SBA-15 Sorbents for CO_2 Capture from Dilute and Ultradilute Gas Mixtures. *ACS Applied Polymer Materials*, *1*(11), 3137–3147. https://doi.org/10.1021/acsapm.9b00788

Sujan, A. R., Pang, S. H., Zhu, G., Jones, C. W., & Lively, R. P. (2019). Direct CO_2 Capture from Air using Poly(ethylenimine)-Loaded Polymer/Silica Fiber Sorbents. *ACS Sustainable Chemistry and Engineering*, *7*(5), 5264–5273. https://doi.org/10.1021/acssuschemeng.8b06203

Szymanska-Chargot, M., Chylinska, M., Kruk, B., Zdunek, A. (2015). Combining FT-IR Spectroscopy and Multivariate Analysis for Qualitative and Quantitative Analysis of the Cell Wall Composition Changes During Apples Development. *Carbohydr. Polym.*, 115, 93−103.

Tamilarasan, P., Remya, T. S., & Ramaprabhu, S. (2013). Ionic Liquid Functionalized Graphene for Carbon Dioxide Capture. *Graphene*, *1*(1), 3–10. https://doi.org/10.1166/graph.2013.1004

Tang, J., Tang, H., Sun, W., Plancher, H., Radosz, M., & Shen, Y. (2005). Poly(Ionic Liquid): A New Material with Enhanced and Fast CO_2 Absorption. *Chemical Communications*, 26, 3325–3327. https://doi.org/10.1039/b501940k

Thakur V. K., Thakur M. K. (2014). Recent Advances In Graft Copolymerization and Applications of Chitosan: a review. *ACS Sustain Chem Eng.*, *2*(12):2637–52. doi:10.1021/sc500634p.

Tolaimate, A., Desbrieres, J., Rhazi, M., Alagui, A. (2003). Contribution to the Preparation of Chitins and Chitosans with Controlled Physico-Chemical Properties. *Polymer*, *44*(26), 7939-7952, https://doi.org/10.1016/j.polymer.2003.10.025

Tsaih, M. L., Chen, R. H. (2003). The Effect of Reaction Time and Temperature During Heterogenous Alkali Deacetylation on Degree of Deacetylation and Molecular Weight of Resulting Chitosan. *J. Appl. Polym. Sci., 88*, 2917–2923

Turci, F., Giulia, M., Corazzari, I., Nistic, R., Franzoso, F., Tabasso, S., & Magnacca, G. (2015). Advanced Physico-Chemical Characterization of Chitosan by Means of TGA Coupled On-Line with FTIR And GCMS : Thermal Degradation and Water Adsorption Capacity. *Polymer Degradation and Stability*. *112*, 1–9. https://doi.org/10.1016/j.polymdegradstab.2014.12.006

Udoetok, I. A., Wilson, L. D., & Headley, J. V. (2016). Self-Assembled and Cross-Linked Animal and Plant-Based Polysaccharides: Chitosan−Cellulose Composites and Their Anion Uptake Properties. *ACS applied materials & interfaces*, *8*(48), 33197–33209. https://doi.org/10.1021/acsami.6b11504

Ünügül, T., & Ugur, F. (2022). Evaluation of Halloysite Nanotube – Loaded Chitosan - Based Nanocomposite Membranes for Water Desalination by Pervaporation. *Water, Air, & Soil Pollution*. https://doi.org/10.1007/s11270-022-05505-z

Usov, I., Nyström, G., Adamcik, J., Handschin, S., Schütz, C., Fall, A., Bergström, L., & Mezzenga, R. (2015). Understanding Nanocellulose Chirality and Structure–Properties Relationship at the Single Fibril Level. *Nat Commun. 6,* 7564. https://doi.org/10.1038/ncomms8564

Vareda, J. P. Valente, A. J. M. Durães, L. (2016). Heavy metals in Liberian soils: Removal by current adsorbents/amendments and prospective for aerogels. *Adv. Colloid Interface Sci.*, 237, 28–42

Vega, F. Sanna, A. Navarrete, B. Maroto-Valer, M. M. Cortés, V. J. (2014). Degradation of Amine-based Solvents in CO_2 Capture Process by Chemical Absorption. *Greenhouse Gases: Sci. Technol.*, *4*(6), 707−733

Wang, N., Ding, E., & Cheng, R. (2007). Thermal Degradation Behaviors of Spherical Cellulose Nanocrystals With Sulfate Group*s*. *Polymer, 48, 3486-3493*. https://doi.org/10.1016/j.polymer.2007.03.062

Wang, P., Zhang, G., Chen, W., Chen, Q., Jiao, H., Liu, L., Wang, X., & Deng, X. (2020). Molten Salt Template Synthesis of Hierarchical Porous Nitrogen-Containing Activated Carbon Derived From Chitosan for CO_2 Capture. *ACS Omega*, *5*(36), 23460–23467. https://doi.org/10.1021/acsomega.0c03497

Wang, Q. Q., Zhu, J. Y., Reiner, R. S., Verrill, S. P., Baxa, U., McNeil, S. E. (2012). Approaching Zero Cellulose Loss In Cellulose Nanocrystal (CNC) Production: Recovery And Characterization of Cellulosic Solid Residues (CSR) and CNC. *Cellulose*, *19*(6), 2033−2047

Wang, S., Mahurin, S. M., Dai, S., & Jiang, D. E. (2021). Design of Graphene/Ionic Liquid Composites for Carbon Capture. *ACS Applied Materials and Interfaces*, *13*(15), 17511–17516. https://doi.org/10.1021/acsami.1c01242

Wang, S., Tian, Z., Dai, S., & Jiang, D. E. (2017). Optimal Size of a Cylindrical Pore for Post-Combustion CO_2 Capture. *Journal of Physical Chemistry C*, *121*(40), 22025–22030. https://doi.org/10.1021/acs.jpcc.7b05516

Wardhono, E. Y., Pinem, M. P., Kustiningsih, I., Effendy, M., Clausse, D., Saleh, K., & Guénin, E. (2021). Heterogeneous Deacetylation Reaction of Chitin Under Low-Frequency Ultrasonic Irradiation. *Carbohydrate polymers*, *267*, 118180. https://doi.org/10.1016/j.carbpol.2021.118180;

Wei, L., Wei, W., Xue, N., Cheng, F., & Yang, H. (2021). One-Step Synthesis of Solid–Liquid Composite Microsphere for CO_2 Capture. *ACS Applied Materials & Interfaces*, *13*(4), 5814–5822. https://doi.org/10.1021/acsami.0c19907

World Meteorological Organization (WMO). (2022). Greenhouse Gas Bulletin, No. 13. Available online: https://public.wmo.int/en/media/press-release/greenhouse-gas-concentrations-surge-new-record (accessed on 6 May, 2022)

Wotzka, A., Dühren, R., Suhrbier, T., Polyakov, M., & Wohlrab, S. (2020). Adsorptive Capture of CO_2 from Air and Subsequent Direct Esterification under Mild Conditions. *ACS Sustainable Chemistry and Engineering*, *8*(13), 5013–5017. https://doi.org/10.1021/acssuschemeng.0c00247

Wu, H., Yuan, Y., Chen, Y., Lv, D., Tu, S., Wu, Y., Li, Z., & Xia, Q. (2021). Highly Efficient Capture of Postcombustion Generated CO_2 through a Copper-Based Metal-Organic Framework. Energy and Fuels, *35*(1), 610–617. https://doi.org/10.1021/acs.energyfuels.0c03144

Xia, Y., Mokaya, R., Walker, G. S., & Zhu, Y. (2011). Superior CO_2 Adsorption Capacity on N-Doped, High-Surface-Area, Microporous Carbons Templated From Zeolite. *Advanced Energy Materials*, *1*(4), 678–683. https://doi.org/10.1002/aenm.201100061

Xu, X., Liu, F., Jiang, L., Zhu, J. Y., Haagenson, D., & Wiesenborn, D. P. (2013). Cellulose Nanocrystals vs. Cellulose Nanofibrils: A Comparative Study on Their Microstructures and Effects as Polymer Reinforcing Agents. *ACS Appl. Mater. Interfaces*. dx.doi.org/10.1021/am302624t

Yuan, P., Southon, P. D., Liu, Z., Green, M. E. R., Hook, J. M., Antill S. J., & Kepert, C. J. (2008). Functionalization of Halloysite Clay Nanotubes by Grafting with γ-Aminopropyltriethoxysilane. *J. Phys. Chem*. C, 112, 15742–15751. https://doi.org/10.1021/jp805657t

Zhang, M., Jiang, S., Han, F., Li, M., Wang, N., & Liu, L. (2021). Anisotropic Cellulose Nanofiber/Chitosan Aerogel with Thermal Management and Oil Absorption Properties. *Carbohydrate Polymers*, *264*, 118033. https://doi.org/10.1016/j.carbpol.2021.118033

Zhang, T., Zhang, W., Zhang, Y., Shen, M., & Zhang, J. (2020). Gas phase synthesis of aminated nanocellulose aerogel for carbon dioxide adsorption. *Cellulose*, *27*(6), 2953–2958. https://doi.org/10.1007/s10570-020-03035-7

Zhang, W. & Xia, W. (2014). Dissolution and Stability of Chitosan in a Sodium Hydroxide/ Urea Aqueous Solution. *131*(3), 2–7. https://doi.org/10.1002/app.39819

Zhang, Y., Zhang, Y., Wang, X., Yu, J., & Ding, B. (2018). Ultrahigh Metal-Organic Framework Loading and Flexible Nanofibrous Membranes for Efficient CO_2 Capture with Long-Term, Ultrastable Recyclability. ACS Applied Materials and Interfaces, 10(40), 34802–34810. https://doi.org/10.1021/acsami.8b14197

Zulfiqar, S., Mantione, D., El Tall, O., Sarwar, M. I., Ruipérez, F., Rothenberger A., and Mecerreyes, D. (2016). Nanoporous Amide Networks Based on Tetraphenyladamantane for Selective CO_2 Capture. *J. Mater. Chem. A*, 4, 8190-8197 https://doi.org/10.1039/C6TA01457G

Zulfiqar, S., Sarwar, M. I., & Mecerreyes, D. (2015). Polymeric Ionic Liquids for CO_2 Capture and Separation: Potential, Progress and Challenges. *Polymer Chemistry*, *6*(36), 6435–6451. https://doi.org/10.1039/c5py00842e